Electronic Thesis and Dissertation Repository

8-12-2022 2:00 PM

Geomechanical Modeling of a Fault During Fluid Injection

Charles KW Hulls, *The University of Western Ontario*

Supervisor: Shcherbakov, Robert, *The University of Western Ontario*
A thesis submitted in partial fulfillment of the requirements for the Master of Science degree in Geophysics
© Charles KW Hulls 2022

Abstract

The injection of fluid into rock masses as a part of industrial processes, such as hydraulic fracturing, can lead to an increase in seismic activity. The movement of the injected fluid and resulting stresses can be simulated and analyzed. One aspect of this analysis is the predicted rate of seismic activity, obtained via the Dietrich rate-and-state law and the Coulomb Failure Stress. This work produces simulations for two fracturing scenarios in the Duvernay Shale region. Model parameters, such as layer permeability and timing of fault slip, are varied to determine their impact on the model results. The simulated results show that increases in activity are primarily derived from pore pressure increases, and that changes in permeability between models have the most effect on the results.

Keywords: Induced seismicity, geomechanical modelling, poroelasticity, finite-element analysis, hydraulic fracturing.

Summary for Lay Audience

Hydraulic fracturing, commonly known as fracking, involves the injection of large amounts of water into a section of rock, and is known to be capable of leading to earthquakes. This leads to an increase in pressure that can put stress on the rock surrounding the injection point. These stresses, along with the movement of the water through the rock, can be examined to determine the potential for earthquakes to occur. The pressure increases and stresses on the rock can be combined into a single measurement that can be used to estimate the rate of seismic activity. This work produces simulations for two fracturing scenarios in the Duvernay Shale region in Alberta. These models include variations to determine which aspects are most important, such as how easily the water, can flow through the surrounding rock and when the fault moves in response to the changing stress or increased pressure. Results from the simulations show that the former of those parameters has one of the largest impacts in the overall rate of earthquake occurrence. The results also show that most of the earthquakes were triggered as a result of pressure increases instead of stress changes within the rock itself.

Acknowledgments

First, I would like to thank my supervisor, Dr. Robert Shcherbakov. His time and expertise with both the subject matter and the process of thesis writing were both invaluable for the completion of this thesis.

I would also like to thank Prof. Katsuichiro Goda, Dr. Karen Assatourians, and Prof. Geoff Wild for their willingness to act as the review committee for this thesis.

Thank you to NSERC for providing funding.

Thank you to both the Western Writing Centre and Elisa Dong for their advice on how to convey the information in written form.

Finally, thank you to my family for their support. I would not have accomplished this without your kind words and occasional prodding.

Table of Contents

List of Tables

List of Figures

xv

Chapter 1

1 Introduction and Literature Review

1.1 Problem Statement

Most seismic events are of little concern since they are often too small to be noticed. In general, earthquakes are a result of the natural tectonic activity taking place in the brittle outer layer of the Earth in relatively narrow and well-established zones. Natural sources of stress, such as tectonic plate movement, can cause an earthquake when the stress buildup becomes large enough to cause movement along a fault surface. However, seismic events can also be triggered by human activity - referred to as induced seismicity (Ellsworth, 2013, Eaton, 2018, Schultz et al., 2020). It is important to study induced seismicity because it can lead to larger events than would be expected within a region, and thus buildings and other structures may not have been built with the capability to withstand said events.

Industrial processes that can induce seismicity involve removing material from the Earth, as in mines, or adding material, such as impounding a reservoir behind a dam or injecting fluid into the subsurface rock layers directly (Grigoli et al., 2017). While different activities have varied mechanisms for triggering seismic events, the injection of fluids under subsurface is commonplace in several processes. These include wastewater disposal (Zhai et al., 2019), enhanced geothermal reservoir stimulation (Baisch et al., 2010), hydraulic fracturing for resource exploitation (Bao and Eaton, 2016), and carbon capture and storage (Chang et al., 2018). Of these processes, hydraulic fracturing, informally referred to as fracking, has been particularly controversial for its potential environmental impacts, including induced seismicity, and has received mainstream attention as a result.

In order to safely perform these processes which plays an important role in economy, it is vital that scientists gain an understanding of the underlying processes that cause induced seismic events. Interest in induced seismicity dramatically increased after a

5.9-magnitude earthquake occurred in Oklahoma in November 2011, believed to have been caused by wastewater injection (Grigoli et al., 2017).

In order to forecast and understand the effect of energy related anthropogenic activities and the potential for induced seismicity, detailed physical models that describe the evolution of the stresses and propagation of fluids in porous media are needed. Current predictive models of earthquake frequency and magnitude are lacking newly available theoretical information, which can be solved by expanding the existing models with more parameters. It is particularly important to have robust forecasting since the seismicity of an injection site can peak after injection has stopped. This is potentially due to the time it takes for the changes in pore pressure and stresses to propagate to seismically prone areas (Segal and Lu, 2015, Chang et al., 2018). The current standard method for closing wells is based on a reactionary response when an earthquake occurs (Bao and Eaton, 2016). Coupled with the difficulty in installing dense networks of sensing equipment (seismometers) to detect earthquakes with smaller magnitudes (Ellsworth, 2013), it becomes very important to have physically realistic methods for determining when and how to stop injections, rather than the current standard, which is based on a reactionary response when significant seismic events occur (Bao and Eaton, 2016). Important aspects to consider include the movement of injected fluid, stresses on the rock as a result of injection or fault movement, and how the presence and location of various features of the formation affect these stresses.

1.1.1   Research Questions

This work is a forward-modelling study based on hydraulic fracturing operation data from the Duvernay formation and has both practical and theoretical benefits. From this, the scope of the model is expanded so that it can cover similar operation scenarios, approaching the point at which the model is robust enough to be usable for real-life scenarios in risk assessment of potential injection sites.

This thesis contributes to the study of induced seismicity through the development of two geomechanical models of seismic activity as a result of fluid injection from hydraulic fracturing operations, modelling activity in scenarios based on field data

gathered from the Western Canada Sedimentary Basin. This work examines how pore pressure diffusion, poroelastic stresses, and slip on a fault interact with each other and determine the overall seismicity of a system undergoing a hydraulic fracturing operation. The impact of varying fault properties including permeability, slip magnitude, and orientation with respect to other features is investigated, as well as the impact of the distribution of fluid injection and the parameters determining the areas surrounding the faults.

To understand the process of how induced seismicity occurs during hydraulic fracturing, it is necessary to understand the interplay between poroelastic stresses, pore pressure diffusion, and the slip on a given fault. Questions to be answered are:

- Can a model be developed based on existing data that explains the seismic activity similar to the recorded seismic events?
- Can this model be expanded to incorporate different arrangements of faults and/or fracture zones?
- Using these models, what is the effect on the overall stress state due to changes in the model parameters such as the angle of a fault and the surrounding rock permeability?

1.2   General Overview

1.2.1   Injection-Induced Seismicity

One of the earliest major review papers on injection-induced seismic activity is by Ellsworth, (2013). Ellsworth (2013) identified increases in pore pressure and poroelastic stressing as two main mechanisms by which stress might be transferred to a fault and cause it to slip resulting in an earthquake. Additionally, he noted that high volume injections, such as those used in large-scale wastewater injection, are more likely to trigger larger earthquakes. These two mechanisms of stress transfer were repeated in a later review, with note of the need for improved monitoring systems at injection sites (Grigori et al., 2017). The importance of the underlying structure of the formation in determining the expected activity was noted in Kernanen and Weingarten (2018).

The introduction of poroelastic stresses into numerical models of fluid injection is a recent development (Segall and Lu, 2015, Deng et al., 2016, Chang and Segal, 2016, Chang et al., 2018, Yehya et al., 2018, Kernanen and Weingarten, 2018, Verdeccia,

Cochran, and Harrington, 2021). In addition to examining models that include poroelastic stresses, newer surveys of the literature, such as Atkinson et al. (2020) and Schultz et al. (2020), also included loading from aseismic slip occurring on other faults as a method of stress transfer and fault activation, noting works such as Bhattacharya and Viesca (2019) and Eyre et al. (2019) that focused on aseismic loading. However, these reviews suggested increases in pore pressure as the most significant method of fault activation (Atkinson et al., 2020, Schultz et al., 2020). More recently, hydraulic fracturing operations are now included in the analyses when they were previously disregarded due to the process involving a smaller injection volume than other injection activities (Atkinson et al., 2020, Schultz et al., 2020).

1.2.2   Hydraulic Fracturing

Hydraulic fracturing, abbreviated as hydrofracturing and often colloquially referred to as fracking, is a process by which fluid is injected into a rock mass in order to produce fractures to increase the permeability for resource extraction (Ellsworth, 2013, Ge et al., 2020). Despite the low tensile strength of rocks, the injection pressure must be significant, since it needs to exceed the ambient compressive stresses acting at depth (Eaton, 2018). The volume of fluid injected is small compared to other industrial processes, since the fluid storage of the rock mass is not used for the injected fluid (Bao and Eaton, 2016).

Much of the earlier hazard data for induced seismicity comes from operations that involve large volumes of fluid at comparatively low pressure, such as the disposal of wastewater (Ellsworth, 2013, Segall and Lu, 2015, Chang and Segall, 2016, Yeyha et al., 2018, Zhai et al., 2019, Verdecchia et al., 2021) and geothermal projects (Altmann et al., 2014, Deichmann et al., 2014, Atkinson et al., 2016, Meller and Ledesert, 2017). For this type of injection, the expected magnitude of an induced earthquake is strongly tied to the total injected volume (McGarr, 2014, Atkinson et al., 2016). Carbon capture operations can use this data as well, since CO_2 is occasionally injected dissolved in brine (Bickle, 2009), and it was determined by Nicot et al. (2011) that an accurate model of the resulting stresses could be obtained without modelling the incoming CO_2 and the pre-existing water separately.

Hydraulic fracturing operations are distinct from high volume wastewater injection operations since they entail a relatively small injection volume and a much higher injection pressure (Bao and Eaton, 2016). Additionally, the standard purpose of hydrofracturing operations means they are used in less permeable formations (Rutqvist et al., 2013), which may have led to the earlier belief hydraulic fracturing (HF) seismic hazard was going to be low. Hydrofracturing operations can trigger larger earthquakes than their injection volume may suggest based on the power law used for other injections (Atkinson et al., 2016, Castro et al., 2020). Hydrofracturing earthquakes frequently have a less organized structure than the normal foreshock-mainshock-aftershock sequence of tectonic earthquakes (Schultz et al., 2020). This may be due to the rock type associated with HF operations: less granitic regions are noted to have more swarm-like earthquakes under geothermal operations (Meller and Ledesert, 2017). For these reasons, hydraulic fracturing operations need to have their own class of models to determine the associated hazard. Several numerical models of hydraulic fracturing operations often focused on the details of crack expansion over the possibility of induced seismicity, as in Damjanac and Cundall, (2016) and de Borst (2018). These works noted that the path of injected fluid can be altered by pre-existing faults (Zhao and Young, 2011) and that the applied stresses from fracturing can exceed the threshold for slip on a fault (Ge et al., 2020).

Major reviews on the study of fracturing-induced seismicity have been published in recent years. In Schultz et al. (2020), the locations of seismic events relative to the injection wells were discussed. They note that most earthquakes are close enough in space and time to the injection and activity can be ascribed to increases in pore pressure at the fault. In another recent review, it was noted that induced events often have lower stress changes than natural events but shallower foci when compared to natural events (Atkinson et al., 2020). This in turn leads to induced events being capable of resulting in similar damage to natural ones at short distances. Both of these reviews noted the difficulty in accumulating statistical data from industrial operators (Atkinson et al., 2020, Shultz et al., 2020).

1.2.3   Hydraulic Fracturing in Canada

Much of the fluid injection activity in Canada is part of the hydraulic fracturing operations in the Western Canada Sedimentary Basin. Other processes occurring in this region, such as wastewater disposal, show reduced correlation with recorded seismicity (Atkinson et al., 2016). By contrast, statistical analysis shows a very strong correlation between hydraulic fracturing operations and recorded seismic activity in the area, which has been historically inactive (Atkinson et al., 2016). Some of these operations occur in the Fox Creek region in Alberta, as part of oil and gas extraction from the Duvernay formation (Atkinson et al., 2016, Bao and Eaton, 2016, Deng et al., 2016). Several noticeable earthquakes have occurred in this region and are believed to be consequences of the fracturing and extraction operations. These include a moment magnitude Mw 4.27 event on June 13. 2015 and a M 4.1 event on January 12, 2016 (Atkinson et al., 2016, Bao and Eaton, 2016). Given the low permeability of the shale being worked on, aseismic movement has been invoked as an explanation for recorded events occurring sooner after injection than would be expected based on pore pressure diffusion alone (Eyre et al., 2019, Atkinson et al., 2020).

As a result of concerns about the seismic activity in the area, the Fox Creek region also houses the Tony Creek Dual Microseismic Experiment, a set of injection wells and sensors designed to measure the response to fluid injection (Eaton et al., 2018, Igonin et al., 2021). In order to simulate the behaviour of industrial fracturing projects, fluid was injected into these wells (Igonin et al., 2021). The results of this work demonstrate the possibility of networks of cracks in a rock formation acting as a permeable channel and allowing high pore pressure to be transferred faster than normal (Igonin et al., 2016). This explanation was backed up by similar data from Castro et al. (2020), which came to a similar conclusion when analyzing a Mw 4.2 earthquake in the Montney formation near the border between Alberta and British Columbia.

1.2.4   Injection-Induced Seismicity in the US

In contrast to induced seismicity in Canada being ascribed primarily to hydraulic fracturing operations, much of the activity in the US appears to result from the large-scale

disposal of wastewater from both hydraulic fracturing operations and other industrial activities (Ellsworth, 2013). In these processes, fluid is often injected into a permeable reservoir surrounded by impermeable formations to reduce leaching of the wastewater. Many earthquakes in the last decade have been recorded at a depth corresponding with wastewater disposal projects (Ellsworth, 2013, Atkinson et al., 2016). These situations can also lead to seismic activity even years after the injection has concluded (Gan and Frolich, 2013, Zhai et al., 2019,)

1.3   Concepts Overview

1.3.1   Direct Effects of Pore Pressure

Three major mechanisms for stress transfer in fluid injection systems have been proposed for triggering injection-induced earthquakes: pore pressure effects, poroelastic stress, and aseismic slip (Ellsworth, 2013, Bhattacharya and Viesca, 2019, Atkinson et al., 2020,). Of these, pore pressure effects were examined earliest, such as in Mazzoldi et al. (2012), Gan and Frolich (2013), Woods (2015), Shapiro (2015), and Zoback (2019). Increases in pressure act against the ambient normal stress on a fault, reducing the effective frictional strength and pushing the fault towards failure (Ellsworth, 2013). The direct effects of pore pressure increases are limited to regions close to or hydraulically connected to the injection site (Keranen and Weingarten, 2013). Since hydraulic fracturing often takes place in less permeable environments, this limitation may have contributed to a belief that fracturing projects are less capable of producing injection-related seismicity. This in turn may have led to a large number of sources on hydraulic fracturing not mentioning potential seismic impacts (Zhao and Young, 2011, Rutqvist et al., 2013, Damjanac and Cundall, 2015, Eaton, 2018, Zoback, 2019, Ge et al., 2020). Other triggering mechanisms are used to explain seismic events that do not occur in pressurized areas, most significantly, poroelastic stressing from the injection sites and aseismic movement on other faults that are pressurized (Atkinson et al., 2020).

Recently, pore pressure interactions have been re-examined as a principal triggering mechanism even for systems where the well is not obviously connected to the fault. Networks of small fractures in the rock mass can create a permeable channel

through which fluid can flow into and pressurize a fault. The work done by Castro et al. (2020) emphasized this, noting that older formations are likely to have cracks, and a connection to another region can be inferred by a relative lack of recovered fluid compared to other injection wells, and that including a permeable connection into a simulated model of an injection site significantly increases the possibility of slip on the examined fault. Similar results were reported by Igonin et al. (2021), where the effects of other stressors were smaller than the pressure increase in areas connected to the injection via fracture corridors. These corridors were also noted to have been found in field measurements of the studied formation.

1.3.2   Poroelastic Effects

Poroelastic theory was developed mainly following Biot (1941) and Skempton (1954) and is well established in geophysics contexts. These original works focused on the context of groundwater aquifers. Changes in the fluid content of reservoirs can lead to changing seismicity from natural processes such as seasonal rain (Hsu et al., 2021) compared to deliberate fluid injection. Indirect stresses from injection may also be derived from thermal (Cheng, 2016) and chemical transfer (Sherwood, 1993) in addition to changes in pore pressure. Thermal factors are only occasionally considered for models of induced seismicity (see Andres et al., 2019 and Jiang et al., 2021), but have generally not been considered a major mechanism for stress transfer when compared to the direct and indirect effects of pore pressure movement due to the pressures involved being much higher than other contributors to the solid deformation (Atkinson et al., 2020).

Poroelastic contributions to the stress state are often small compared to the pressure increase in areas where fluid can reach but are more significant at larger distances and in less permeable environments (Verdecchia, Cochran, and Harrington, 2021, Grigoli et al., 2013, Segall and Lu, 2015, Chang and Segall, 2016, Deng et al., 2016, Zhai et al., 2019). Unlike the reduction in friction related to an increase in pore pressure, poroelastic stresses can inhibit slip in areas close to the fault (Yehya et al.,

2018) and cause faults to slip in directions other than their unperturbed stress state would indicate (Altmann et al., 2014)

1.3.3   Aseismic slip

A fault can also slip without producing a seismic event. This occurs when velocity-dependant variables, such as the critical slip distance, produce negative feedback and inhibit further movement (Im et al., 2020). Stress changes resulting from this slow movement can be transferred to other parts of the rock, and this stress transfer has been used to explain the occurrence of large tectonic earthquakes (van den Ende et al., 2020). This movement can propagate faster than pore pressure changes under the right conditions (Bhattacharya and Viesca, 2019). At deeper depths, this effect is less apparent since it is dominated by the ambient stresses being applied, but it can be relevant at shallower depths (Sgambato et al., 2020). Since induced seismicity often occurs at a shallower depth than tectonic seismicity (Yenier and Atkinson, 2015), and sudden changes in pore pressure can lead to aseismic slip (Viesca and Dublanchet, 2019), aseismic loading has been considered as a mechanism for triggering induced earthquakes. It has been assumed as the main mechanism for earthquakes occurring soon after injection in hydrofracturing systems, where the lower permeability of the surrounding rock is assumed to lead to pore pressure increases travelling too slowly to reach an existing fault in time for an observed event (Eyre et al., 2019). However, more recent studies suggested that fluid pressure can reach farther than originally anticipated by using fracture networks (Castro et al., 2020, Igonin et al., 2021, Wang et al., 2021).

Regardless of whether aseismic slip leads to the triggering of induced earthquakes, it has been noted to occur in fluid-injection systems (Cappa et al., 2019). Cornet (2016) noted that activation of existing fractures and shear failure at a lower pore pressure than is required for tensile fracturing. It has been noted that hydraulic fracturing operations can lead to seismic activity long after injection ends (Bao and Eaton, 2016). This can be explained via aseismic movement. A sufficient stress drop from aseismic movement can lead to an earthquake occurring later than it normally would have been observed (Liu et al., 2021).

1.4   Modelling of Faults

1.4.1   Fault Properties

There are several ways a fault can be simulated. In one approach, faults are represented as an area with different properties to the surrounding rock (Treffeisen and Henk, 2020). Because faults are often quite thin compared to the size of the space being modeled, this can result in overly large simulated faults if the resolution of the simulation model is not high enough (Treffeisen and Henk, 2020). Even so, this approach is often used in studies of injection-induced seismicity because it more easily allows simulation of fluid moving through the fault. This approach was used in (Chang and Segall, 2016, Deng et al., 2016, and Igonin et al., 2021). An alternative approach is to represent a fault as a border of model elements that does not transfer shear stress through it (Treffeisen and Henk, 2020). This approach is often used in studies where a crack is allowed to expand, such as in Basich et al., 2010, Damanjanac and Cundall, 2016, and Cundall, 2020. The former of these two approaches will be used in this work.

1.4.2   Stressing and Seismic Activity Rate

A commonly used relation between the stress state of a system and the rate of seismic activity was established by Dieterich (1994). This relation describes the frictional strength of the fault as dependant on both the current stress state and its rate of change and is sometimes referred to as the Dietrich rate-and-state law (Hiemisson and Segall, 2018). This law is capable of replicating the observed behaviour of earthquake aftershocks, which follow a pattern referred to as Omori decay (Dieterich, 1994). Dieterich's law is often simplified by combining several stress terms into one parameter, the Coulomb Failure Stress (CFS) (Cocco and Rice, 2002, Segall and Lu, 2015, Chang and Segall, 2016, Heimisson and Segall, 2018). The original work on the rate-and-state law did not include changes in pore pressure within the rock, but pressure can be included into the CFS (Segall and Lu, 2015). It has been attempted to model pressure changes in other parts of the relation, however this was noted to only be particularly accurate under specific conditions (Cocco and Rice, 2002).

1.4.3   Forward-Modelling Simulations of Induced Seismicity

For the case of high-volume injection, such as wastewater disposal, several forward-modelling studies have been performed to examine the effects of the injected fluid after injection has concluded. These models include the work done by Segall and Lu (2015), Chang and Segall (2016), Chang, Yoon, and Martinez (2018), Zhai et al. (2019), Shirzaei et al. (2019), and Shiu et al. (2021). Within these models, the fluid flow was calculated using Darcy's law, and the stress state of the rock matrix is coupled to the pore pressure. Occasionally, as in Chang and Segall (2016), the model was fully coupled, with the pore pressure also being dependant on the stress state of the surrounding rock. These works showed that activity can peak some time after injection finishes. This can suggest that a more gradual cutoff of injection may reduce the risk of earthquakes (Chang et al., 2018). It was similarly noted by Basich et al., (2010) that the most seismically active regions appear to be where the stress state is changing rapidly instead of simply the areas with the highest pore pressure.

Another notable work in this area is by Jiang, (2021), which examined the importance of several parameters in determining the surface displacement after fluid injection into a reservoir. Their results suggest that the permeability and porosity of the simulated rocks are the most prominent factors in the displacement (Jiang, 2021). However, it did not include analysis of the resultant stresses or seismic activity on a fault.

Within the context of hydraulic fracturing, there does not appear to be a consensus as to the triggering mechanism for induced earthquakes. Papers, such as Deng et al. (2016), Eyre, et al. (2019), and Lui, Huang, and Young (2021), suggest that stress is transferred via aseismic movement of other faults. These sources suggest that the low-permeability rock being injected into cannot transfer fluid fast enough for recorded earthquakes to have occurred as a result of increasing pore pressure. By contrast, recent papers including Igonin et al (2021) and Wang et al. (2021) suggest that the earthquakes were triggered by increases in pore pressure, with fluid moving through permeable cracks in the rock.

1.5   Outline of the Thesis

In order to better understand which factors are most significant for determining the likelihood of earthquakes induced by a hydraulic fracturing operation, I performed numerical simulations of injection operations into the Duvernay formation.

The details of the physical laws and computational implementations used in these simulations are described in Chapter 2. The solid stresses on the rock mass are detailed first, including the contribution of the pore pressure on the stress state. Then, the governing equations for the pore fluid flow are reviewed, including the contribution from the stress state. The solid and fluid stresses are then combined into the Coulomb Failure Stress, which is used to calculate the rate of seismic activity.

Chapter 3 showcases the simulations for normal and reverse faulting regimes using a vertical cross-section of the formation. Model parameters are described first, then a series of case studies exploring the impact of several simulation parameters. Those used in the calculation of the activity rate are examined first before moving on to variations in the slip magnitude, timing, and direction. Following those examples, the system geometry and material properties are explored, starting with a non-conductive fault and differences in the angle of the fault. Finally, the permeability of certain rock layers is altered.

Chapter 4 then continues by examining the simulations for strike-slip faults using a top-down model. After the model parameters are described, case studies follow similar to in Chapter 3. A second fault hydraulically disconnected from the injection sites is introduced to serve as a comparison point. Following this, the direction in which injection proceeds is inverted, as is the direction of fault slip. The angle of the second fault is then altered to explore the effect of having multiple faults at different angles. Finally, the propagation of fluid from the injection sites to the fault is examined by changing the size and permeability of the fracture corridor connecting them.

The relative importance of the parameters explored in Chapters 3 and 4 are examined in greater detail in Chapter 5. The two models are compared to the field data

used to construct them in order to determine their accuracy. How much each parameter affects the overall activity is ranked. Values for these parameters are suggested such that the models align best with recorded activity.

Finally, conclusions drawn from this work are described in Chapter 6. The research questions described in 1.1.1 are revisited and answered.

Chapter 2

2   Methods

Some aspects of the behaviour of faults, and the effects of the fluid injection into the subsurface are based on common approaches to modelling poroelastic rock materials. The possibility of fault failure and resulting occurrence of earthquakes use relations that are standard for both induced and tectonic earthquakes. The state of the rock can be determined from the stress tensor, which can also be used to calculate the displacement of each modelled particle, while the diffusion of pore fluid can be modelled using Darcy's law. These factors can be coupled together to form a comprehensive picture of the system. This data can then be used to calculate the expected rate of seismic activity using the Rate-and-State Law. This chapter contains the derivation of the equations used, as well as the implementation common to all simulations. The specific models and their parameters are described later, in Chapters 3 and 4.

2.1   Stresses on the Solid Matrix

In solid mechanics, the two principal quantities are the stress σ and the strain ϵ. Stress measures the force experienced by sections of material as a result of adjacent sections, while strain measures the resulting relative deformation. Knowing the stresses and strains of a system allows the behaviour, such as when the material fails, to be modelled. The rock surface can be described using these quantities, with the stresses and strains each forming a 3×3 tensor. The stress tensor is often expressed as it appears below (Zoback, 2007):

$$\overset{\leftrightarrow}{\sigma} = \begin{pmatrix} \sigma_{xx} & \sigma_{xy} & \sigma_{xz} \\ \sigma_{yx} & \sigma_{yy} & \sigma_{yz} \\ \sigma_{zx} & \sigma_{zy} & \sigma_{zz} \end{pmatrix}. \tag{2.1}$$

Stresses along the diagonal are classified as normal stresses, and those not on the diagonal are classified as shear stresses (Zoback, 2007). Shear stresses are also labelled by τ instead of σ when not denoted by their location in a tensor. The stress tensor is symmetric, i.e., $\sigma_{ij} = \sigma_{ji}$. Like other matrices, the stress tensor can be diagonalized to reduce the number of parameters used to calculate the state of the system. The matrices used to diagonalize the stresses can be interpreted as a set of rotations through Euler

angles, so the process itself corresponds to a change in the coordinate system (Zoback, 2007):

$$\overleftrightarrow{\sigma} = \overleftrightarrow{R} * \begin{pmatrix} \sigma_i & 0 & 0 \\ 0 & \sigma_i & 0 \\ 0 & 0 & \sigma_i \end{pmatrix} * \overleftrightarrow{R}^{-1}. \tag{2.2}$$

In equation (2.2), $\overleftrightarrow{R}$ represents the rotation matrix used to diagonalize the stress tensor and is composed of the sines and cosines required for the coordinate transform. The resulting eigenvalues of the stress state σ_i are referred to as the principal stresses of the system and are conventionally labelled as σ_1, σ_2, and σ_3 with $|\sigma_1| \geq |\sigma_2| \geq |\sigma_3|$ while the rotation matrix $\overleftrightarrow{R}$ is composed of the normalized eigenvectors of that state. For a rock formation, the effects of gravity and the interface with a fluid at the surface not supporting shear loads mean that one of these principal stresses is nearly always vertical (Zoback, 2007), with the other two varying in rotation through the horizontal plane. For a 2D system, the normal and shear stresses for a fault at angle θ_f to the first principal stress can be calculated via the following equations (King and Deves, 2015):

$$\sigma = \frac{\sigma_1 + \sigma_3}{2} - \frac{\sigma_1 - \sigma_3}{2} \cos(2\theta_f), \tag{2.3}$$

$$\tau^L = \frac{\sigma_1 - \sigma_3}{2} \sin(2\theta_f), \tag{2.4}$$

$$\tau^R = -\frac{\sigma_1 - \sigma_3}{2} \sin(2\theta_f). \tag{2.5}$$

These equations include two different shear stresses, τ^L and τ^R, to provide for the possibility of the fault to slip in both the right-lateral (i.e. when viewing across the fault, the section opposite the observer moves rightward) and left-lateral (the reversed movement of right-lateral) directions.

Like stress, the strain of a system can be described as a second-order tensor. It is formally defined using the derivatives of the displacements u_i with respect to the positions x_i (Zoback, 2007):

$$\epsilon_{ij} = \frac{1}{2} \left(\frac{\partial u_i}{\partial x_j} + \frac{\partial u_j}{\partial x_i} \right). \tag{2.6}$$

Similar to the principal stresses, diagonalizing the strain tensor produces what are referred to as the principal strains of the system: ϵ_1, ϵ_2, and ϵ_3. If the properties of the medium do not vary with position or angle (i.e., the material is homogenous and

isotropic), the principal strains will match the directions of the principal stresses (Zoback, 2007).

It is however more useful to have a relation between the strain and the applied stress. The primary model used for the deformation of a rock mass is referred to as linear elasticity, reflecting both that stress and strain are linearly proportional, and that the deformation can be reversed. The rock is then referred to as a linearly elastic material. In this case, the constant of proportionality relating compressive axial stress σ_{ii} to the strain in the same direction ϵ_{ii} is the Young's modulus E (Zoback, 2007)

$$\sigma_{ii} = E\epsilon_{ii}. \tag{2.7}$$

In addition to compacting in the direction of an applied compressive stress, a material will also expand in the directions perpendicular to that stress (see Figure 2.1). The perpendicular strain in the case of loading in the direction of σ_{11} is given by another material property, the Poisson's ratio ν (Zoback, 2007):

$$\nu = -\frac{\epsilon_{33}}{\epsilon_{11}}. \tag{2.8}$$

In equation (2.8), the sign change is included since it relates compaction in one direction to expansion in another. For an incompressible fluid, ν is equal to 0.5, and an idealized solid known as a Poisson solid has a ratio of $\nu = 0.25$ (Zoback, 2007).
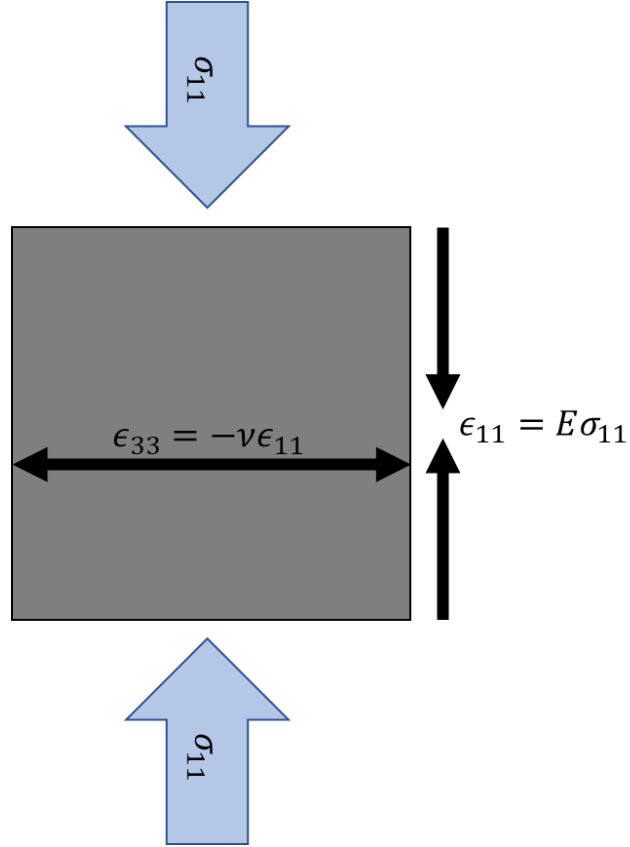
Figure 2.1: Depiction of uniaxial compression showing the relationships between the strains and elastic moduli.

In the case of other stressing conditions, other elastic moduli are preferred. For volumetric compression equal on all sides of magnitude σ_{00}, the bulk modulus K and the compressibility β are used (Zoback, 2007),

$$\sigma_{00} = \frac{1}{3}(\sigma_{11} + \sigma_{22} + \sigma_{33}), \ \epsilon_{00} = \epsilon_{11} + \epsilon_{22} + \epsilon_{33}, \tag{2.9}$$

$$K = \frac{\sigma_{00}}{\epsilon_{00}} = \frac{1}{\beta} \tag{2.10}$$

while for the case of shear loading, the shear modulus G is used (Zoback, 2007)

$$G = \frac{1}{2}\left(\frac{\sigma_{ij}}{\epsilon_{ij}}\right). \tag{2.11}$$

The Lamé constant λ is another elastic modulus, used for the ability to describe a system with relatively simple relations combined with the shear modulus, though it does not have a simple physical representation (Zoback, 2007). It is however more optimized for producing a constitutive equation, which can describe the stresses and strains under

arbitrary conditions instead of being limited to specific circumstances like (2.7) -(2.11):

$$\sigma_{ij} = \lambda \delta_{ij} \epsilon_{00} + 2G \epsilon_{ij}. \tag{2.12}$$

In (2.12), the Kronecker delta δ_{ij} is used to denote which terms only apply when the indices i and j are equal:

$$\delta_{ij} = \begin{cases} 0 & if\ i \neq j \\ 1 & if\ i = j \end{cases}. \tag{2.13}$$

If the material's properties do not depend on orientation relative to the stress field, it is referred to as isotropic. For isotropic materials, any two of the above elastic moduli can fully describe the behaviour of the material. In this case, the moduli are related as follows (Zoback, 2007):

$$K = \frac{2G(1+\nu)}{3(1-2\nu)} = \frac{E}{3(1-2\nu)} = \frac{E}{3\left(3-\frac{E}{G}\right)}, \tag{2.14}$$

$$E = 2G(1+\nu) = 3K(1-2\nu) = \frac{9KG}{3K+G}, \tag{2.15}$$

$$G = \frac{E}{2+2\nu} = 3K\frac{1-2\nu}{2+2\nu} = \frac{3KE}{9K-E}, \tag{2.16}$$

$$\nu = \frac{3K-2G}{6K+2G} = \frac{E}{2G} - 1 = \frac{(3K-E)}{6K}, \tag{2.17}$$

$$\lambda = \frac{2}{3}G - K. \tag{2.18}$$

Anisotropic materials would require additional moduli for different orientations. While many rocks are anisotropic, the models used in this work use isotropic materials to streamline computation.

Rocks are porous due to imperfect packing of irregular grains. The amount that these pores affect the properties of the rock is determined by the porosity ϕ, defined as the ratio of pore volume to total volume of the material

$$\phi = \frac{V_p}{V}. \tag{2.19}$$

If the pores in a material are filled with fluid, it can impact the response of the rock to applied stress. At one extreme, referred to as drained conditions, the pore fluid can freely move in and out of pores in the solid material, equivalent to applying a constraint of zero pore pressure (Cheng, 2016). Drained conditions are often used when the timescale is large enough to allow pressure to equilibrate and uses the same parameters as a dry material (Cheng, 2016). The other extreme condition is referred to as undrained. For

undrained conditions, fluid is not allowed to enter or exit the pores of the solid material, either because of an impermeable barrier or because the timescale is too short to allow the fluid to move (Cheng, 2016). This changes the values of $K, E,$ and ν, but does not change the value of G since the pore fluid is not capable of resisting shear stress. The subscript u is added when referring to undrained parameters (e.g., K_u denotes the undrained bulk modulus). In addition to the various drained moduli, the undrained moduli also depend on the Biot-Willis coefficient α_B and the Skempton coefficient B. The Biot-Willis coefficient describes the magnitude of the pore pressure's contribution to resisting volumetric stress, and ranges between values of 0 (in the case where the pore pressure has no effect) and 1. Meanwhile, the Skempton coefficient $B = \frac{\Delta p}{\Delta \sigma_{00}}$ represents how much the pore pressure p is increased under a compressive load (Cheng, 2016). The undrained moduli are described below (Cheng, 2016):

$$K_u = \frac{K}{1-\alpha_B B}, \tag{2.20}$$

$$E_u = \frac{9KG}{3K+G(1-\alpha_B B)}, \tag{2.21}$$

$$\nu_u = \frac{3K-2G(1-\alpha_B B)}{6K+2G(1-\alpha_B B)}. \tag{2.22}$$

The relationships between different undrained moduli is the same as the relationships between those moduli's drained equivalents (Cheng, 2016) i.e.

$$K_u = \frac{2G(1+\nu_u)}{3(1-2\nu_u)} = \frac{E_u}{3(1-2\nu_u)} = \frac{E_u}{3\left(3-\frac{E_u}{G}\right)}, \tag{2.23}$$

$$E_u = 2G(1+\nu_u) = 3K_u(1-2\nu_u) = \frac{9K_u G}{3K_u+G}, \tag{2.24}$$

$$G = \frac{E_u}{2+2\nu_u} = 3K_u \frac{1-2\nu_u}{2+2\nu_u} = \frac{3K_u E_u}{9K_u-E_u}, \tag{2.25}$$

$$\nu_u = \frac{3K_u-2G}{6K_u+2G} = \frac{E_u}{2G} - 1 = \frac{(3K_u-E_u)}{6K_u}. \tag{2.26}$$

For an isotropic, fluid-filled medium, the relationship between the stresses σ_{ij} and strains ϵ_{ij} depends on elastic moduli, such as the shear modulus G and the drained Poisson ratio ν, as with other solid materials. In addition, the pore pressure within the medium contributes to the normal stress, with the magnitude of that interaction determined by the Biot-Willis coefficient α_B. A constitutive equation can be produced that includes both the pore pressure effects and the stresses on the surrounding rock,

(Wang et al., 2000):

$$\sigma_{ij} = 2G\epsilon_{ij} + \delta_{ij}\left(\frac{2Gv}{1-2v} - \alpha_B p\right). \tag{2.27}$$

Equation (2.27) can describe the stress state of a system, but in its current form cannot calculate the displacements.

The conservation of momentum in the solid matrix can be expressed as follows (Wang, 2000):

$$\frac{\partial \sigma_{ji}}{\partial x_j} - F_i = 0 \tag{2.28}$$

summing across the index j. F_i is representing the applied force on the section of the material being considered in a given direction. Equation (2.28) relates the stresses and positions, and the displacements can be determined using the positions and strains by way of equation (2.6). Substituting in equation (2.27), which relates the stresses and strains, to equation (2.28) then gives a constitutive relation for the displacements u_i (Wang, 2000)

$$G\nabla^2 u_i + \frac{G}{1-2v}\frac{\partial^2 u_k}{\partial x_i \partial x_k} = \alpha_B \frac{\partial p}{\partial x_i} - F_i \tag{2.29}$$

summing across the index k. Solving (2.29) calculates the displacement of the material particles as a result of the external force and the pore pressure differential, allowing the deformation of the material to be examined. This dependence on the pressure differential couples the fluid behaviour to the solid stress state. The steps used to produce these pressure values are outlined below.

2.2   Fluid flow in a Porous Medium

The rate of fluid flow $\vec{q}$ through a porous medium is given by Darcy's law:

$$\vec{q} = -\left(\frac{\kappa \rho_f}{\eta_f}\right)\nabla p, \tag{2.30}$$

where it is dependent on the pressure gradient ∇p, the pore fluid's density ρ_f and viscosity η_f, and the permeability of the material κ (Wang, 2000, Chang and Segall, 2016). κ determines how much the material impedes fluid movement, with higher permeability corresponding to a more free-flowing fluid. Meanwhile, the change in fluid mass can be calculated with the constitutive equation (Wang, 2000):

$$\Delta m = S_\sigma B\sigma + S_\sigma p, \tag{2.31}$$

where B is the Skempton coefficient, and S_σ is the unconstrained specific storage of the material. S_σ relates the change in fluid volume to the change in pressure under the condition of constant applied stress. It can be derived from α_B, G, and both the drained (v) and undrained (v_u) Poisson ratios (Chang and Segall, 2016):

$$S_\sigma = \frac{\alpha_B^2(1-2v)^2(1+v_u)}{2G(1+v)(v_u-v)}. \tag{2.32}$$

Lower values of S_σ imply the surrounding rock does not expand as much as a result of a pore pressure increase. Finally, the continuity of the fluid can be expressed in terms of the flow rate and specific discharge, as well as the external fluid added Q_{ext} (Chang and Segall, 2016):

$$\frac{dm}{dt} + \nabla \cdot \vec{q} = Q_{ext}. \tag{2.33}$$

Substituting (2.30) and (2.31) into the above equation produces an inhomogeneous diffusion equation (Chang and Segall, 2016):

$$S_\sigma \left(\frac{B}{3}\frac{\partial \sigma_{kk}}{\partial t} + \frac{\partial p}{\partial t}\right) - \left(\frac{\kappa}{\eta_f}\right)\nabla^2 p = Q_{ext}. \tag{2.34}$$

Rearranging this shows that the contribution from the changing normal stress is equivalent to another source term (Wang, 2000), which is how this coupling is applied in this work:

$$S_\sigma \frac{\partial p}{\partial t} - \frac{\kappa\rho_f}{\eta_f}\nabla^2 p = Q_{ext} - \frac{S_\sigma B}{3}\frac{\partial \sigma_{kk}}{\partial t}. \tag{2.35}$$

In addition to the unconstrained specific storage, this diffusion equation can also be rewritten in terms of the constrained specific storage S_c (which is used for the case of a constant volume) and includes a source term based on the displacement vector $\vec{u}$ (Chang and Segall, 2016),

$$S_c \frac{\partial p}{\partial t} + \alpha \frac{\partial}{\partial t}(\nabla \cdot \vec{u}) - \left(\frac{\kappa}{\eta_f}\right)\nabla^2 p = Q_{ext}. \tag{2.36}$$

This storage can likewise be defined in terms of other parameters (Chang and Segall, 2016),

$$S_c = \frac{\alpha_B^2(1-2v)(1-2v_u)}{2G(v_u-v)}. \tag{2.37}$$

Under uniaxial strain and constant vertical stress, the diffusion equation does not include an additional source term and can be written in terms of the uniaxial specific storage S_u (Chang and Segall, 2016)

$$S_u \frac{\partial p}{\partial t} - \frac{\kappa}{\eta_f} \nabla^2 p = Q_{ext},$$ (2.38)

$$S_u = \frac{\alpha_B^2 (1-2\nu)^2 (1-\nu_u)}{2G(1-\nu)(\nu_u-\nu)}.$$ (2.39)

For this work, Equation (2.35) is used since the source term is easier to calculate.

Similarly to equation (2.29) that includes a coupling term to apply the effects of the fluid pressure to the solid stresses, equation (2.35) includes the contribution of the normal stress differential on the fluid system. This contribution can be considered mathematically equivalent to an additional fluid source term (Wang, 2000) as if additional fluid is being introduced by being squeezed out of the rock pores by increases in normal stress. For the computed model, this interpretation is used to simulate this term. The overall model is fully coupled between the solid stresses and the pore pressure since the equations used for both sets of variables include terms detailing the contribution from the other set.

2.3   The Coulomb Failure Stress

Once both the pressure and the solid stresses are known at a location, that location can be examined for the possibility of failure. The point of shear failure on a fault is often determined by comparing the shear stress and frictional strength. When they are equal, the fault begins to favour slip:

$$\tau = -\mu\sigma \ ,$$ (2.40)

where τ denotes the shear stress on the system, μ the coefficient of friction, and σ the normal stress on the system (Zoback, 2007). Here, extensional normal stress is taken as positive. Pore pressure acts to decrease the frictional strength, and its inclusion changes (2.40) to

$$\tau = -\mu(\sigma + p)$$ (2.41)

with p representing the pore pressure (Cocco and Rice, 2002). The likelihood of a fault slipping is examined with the changes in these parameters, referred to as the Coulomb

Failure Stress S, abbreviated as CFS (Cocco and Rice, 2002)

$$\Delta S = \Delta \tau + \mu(\Delta \sigma + \Delta p). \tag{2.42}$$

Positive changes in the CFS indicate a fault is more likely to fail. Other methods of examining ongoing fault movement exist, such as the Chen-Neimeijer-Spiers model (Verberne et al., 2020) and the various criteria outlined by Reches (2020), but the CFS is more optimized for determining the effect of changes in the pore pressure. This makes it particularly valuable for studying injection-induced seismicity, where the introduction of fluid and the resulting pressure increases are the main perturbations the system undergoes (Ellsworth, 2013). The calculated changes in the CFS can then be used to compute the expected seismic activity in an area.

2.4   Seismicity Rate

The rate of seismic activity relative to background $R = \frac{r}{r_0}$ is dependant on the background shear stressing rate $\dot{\tau}_0$ and state variable γ (Heimisson and Segall, 2018)

$$R = \frac{1}{\dot{\tau}_0 \gamma}. \tag{2.43}$$

γ is described by a differential equation,

$$\dot{\gamma} = \frac{1}{A\sigma}\left[1 - \gamma\dot{\tau} + \gamma\left(\frac{\tau}{\sigma} - a\right)\dot{\sigma}\right], \tag{2.44}$$

which involves the applied normal and shear stresses, and two constitutive parameters A and a relating the friction to the slip rate and changes in effective normal stress, respectively (Hiemisson and Segall, 2018).

If the ratio of the stresses is assumed to be constant, $\frac{\tau}{\sigma} - a$ can be condensed into a single parameter. The contribution of the changing stresses is then analogous to the change in Coulomb failure stress (Dieterich et al., 2000)

$$-\gamma\dot{\tau} + \gamma\left(\frac{\tau}{\sigma} - a\right)\dot{\sigma} \rightarrow -\gamma(\dot{\tau} - \mu\dot{\sigma}) = -\gamma\dot{S}. \tag{2.45}$$

As such, in this case, the state variable can be expressed with only one other variable, the change in Coulomb Failure Stress $\dot{S}$:

$$\dot{\gamma} = \frac{1}{A\sigma}\left(1 - \gamma\dot{S}\right). \tag{2.46}$$

The assumption of a constant ratio between normal and shear stresses can still produce accurate results compared to the more general case provided the effective coefficient of friction is chosen well (Norbeck and Rubenstien, 2018).

The state variable γ can then be removed, producing a differential equation for the seismic activity rate in terms of the change in CFS (Segall and Lu, 2015, Chang, Yoon, and Martinez, 2018):

$$\frac{dR}{dt} = \frac{R}{t_a}\left(\frac{\dot{S}}{\dot{S}_0} - R\right). \tag{2.47}$$

With $\dot{S}_0$ representing the background Coulomb stressing rate, and t_a the characteristic decay time of the system, equation (2.47) can then be solved numerically. t_a determines how quickly the activity rate decays back to the background value after a perturbation in the CFS and can itself be derived from the background stress rate, effective normal stress $\overline{\sigma}$, and the direct-effect parameter of the rate-and-state law A, shown below.

$$t_a = \frac{A\overline{\sigma}}{\dot{S}_0} \tag{2.48}$$

In addition to the Coulomb stress rate produced by the poroelastic model, two other static parameters are required to solve equation (2.47), $\dot{S}_0$ and t_a. In the case where $\dot{S}_0$ and $\overline{\sigma}$ are unchanging, this can be reduced by the substitutions $y = \frac{R}{t_a}$ and $A_\sigma = A\overline{\sigma}$, transforming the equation into

$$\frac{dy}{dt} = y\left(\frac{\dot{S}}{A_\sigma} - y\right), \tag{2.49}$$

which only requires one additional constant. t_a can then be divided after the calculation of the differential equation is completed to produce R. This is done to increase computational efficiency. An alternate method to simplify the differential equation being calculated is to change the timescale with the substitution $t_R = \frac{t}{t_a}$. This produces an equation that only requires $\dot{S}_0$ to be input, and the scaling can be reversed after the differential equation calculation is completed:

$$\frac{dR}{dt_R} = R\left(\frac{\dot{S}}{\dot{S}_0} - R\right). \tag{2.50}$$

2.5   Computational Modelling

This work makes use of two distinct finite-element models, both two-dimensional cross-sections. A full three-dimensional model was deemed too computationally intensive. The two models are at different orientations in an attempt to include information that would be lost with a single two-dimensional model. The first is a vertical cross-section that includes a fault experiencing normal and reverse faulting, while the second is a horizontal cross-section that deals with strike-slip fault movement. These models, along with their simulated results, are detailed fully in Chapters 3 and 4.

2.5.1   CFS Calculation

Calculations were done on a mesh of elements using the commercially available finite-element software COMSOL 5.4. The meshes themselves are two-dimensional, with the system assumed to have a consistent width. This simulation made use of the fully coupled model described by Equations (2.29) and (2.35). The solid stresses and pore pressure are calculated separately following Equations (2.27) and (2.35) using the preconstructed modules for solid mechanics and Darcy's law, respectively, which are then combined into the Coulomb Failure Stress. Coupling was achieved through the addition of terms dependant on the other module, determined by Equations (2.29) and (2.35).

The CFS is then recorded, alongside its components: the pore pressure, shear stress, and normal stress. The size of the mesh varies between the two distinct models and are detailed in sections 3.2.2 and 4.2.2, respectively. Similarly, the boundary conditions of each model are distinct from each other and detailed in sections 3.2.2 and 4.2.1. Stress data was recorded every $0.1\ days$, and the simulation time steps were set to always include those time points (using the 'strict' setting in the COMSOL interface). However, the actual calculation used significantly shorter time steps adaptively determined by the software.

2.5.2   Seismic Activity Rate Calculation

Seismic activity rate was calculated using the MATLAB function `ode45`, using Equation (2.49). The function is set with an absolute tolerance of 10^{-9}, a relative tolerance of 10^{-8}, and assuming a nonnegative solution. An input file is read containing the CFS at specified coordinates from the Finite-Element model described above, focused on the area near the faults and injection wells. This input file had a time step of $0.1\ days$ between stress measurements. This work contains two significantly different model geometries, and as a result the range of the data used for activity rate calculation is different between them. These ranges are detailed in 3.2.5 and 4.2.2 respectively.

Equation (2.49) is then solved for each point, and the rate is displayed for the area at a specified time. Equation (2.50) was also tested but produced the same results for a single set of input parameters.

2.6   Summary

The above equations allow for examining the potential for fluid injection to produce an earthquake in a given scenario. The CFS is calculated using a fully-coupled poroelastic model, obtained by introducing additional terms into the formulae for linear elasticity and pore pressure diffusion. The CFS calculations are done using COMSOL and are then used to produce a simulated activity rate over time for the relevant regions using MATLAB. The scenarios considered for this work, as well as the results each produces, are detailed next, starting with the scenarios for normal and reverse faulting in Chapter 3 and followed by the models for strike-slip faults in Chapter 4.

Chapter 3

3 Geomechanical Modelling of the Effect of Fluid Injection on Normal and Reverse Faults

3.1 Introduction

This chapter contains the details of a model for fluid injection and the resulting seismicity in and around the Duvernay shale. Modelling is performed in order to determine which aspects of the system most impact the possibility of dangerous earthquakes. General parameters of the model and those of the base case are described first in Section 3.2, with each of the case studies following. All models in this section are vertical cross-sections, and deal with normal or reverse faulting regimes. Which parameters to vary were selected based on what was deemed to have the most impact on the calculated activity The parameters affecting the calculation of the seismic activity rate are examined first in order to establish values for the other simulations to use. The magnitude, timing, and direction of the slip on the fault are varied, followed by the permeability and angle of the fault. Finally, the permeability of other rock layers in the system is changed.

3.2 Model Definition and Simulation Parameters.

The geomechanical model and its several variations studied in this chapter are based on the observational work of the specific case of induced seismicity by Bao and Eaton (2016) and are designed to represent features of the Duvernay formation in Alberta (Figure 3.1). This sequence was chosen since it was a hydraulic fracturing project, and the resulting seismic data provided an indication of where to place faults in the simulation Fluid injection was modelled based on hydraulic fracturing operations that occurred during the time period studied by that work. This model simulated the propogation of fluid from injection points into the surrounding rock structures using Darcy's Law, as well as the stresses on said structures using fully coupled linear poroelasticity. The seismicity rate was then calculated using the state of the pore pressure and stresses.
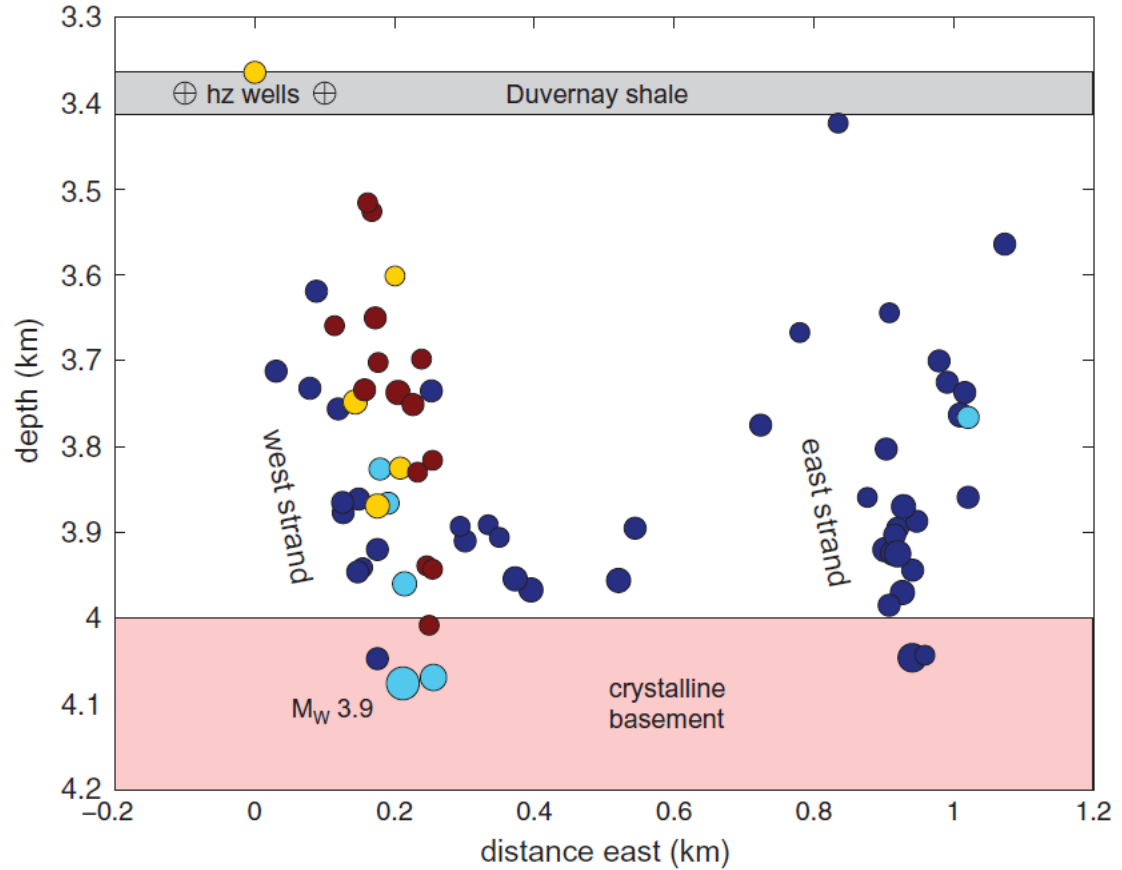
Figure 3.1: Seismic data from Bao and Eaton (2016), showing the locations of recorded earthquakes, as well as the injection wells and rock layers. Earthquakes recorded during the injection, from December 2014 to early January 2015, are coloured as dark blue. The first cluster of events occurring after injection finishes occurred throughout January and are coloured light blue. Following are two more clusters which occurred in February (coloured yellow) and March (coloured red). The size of the circle corresponds to the magnitude of the recorded event. The clustering of earthquakes into the east and west groups is used to infer the locations of faults in the system

3.2.1   Model Geometry and Material Parameters

The bulk of the model is composed of several horizontal layers of rock. A shale layer is inserted between a cap section and an intermediate layer, which share the same material properties. These three layers are then placed above the basement layer. Two

faults extend from the upper part of the basement into shortly below the shale layer. These faults are defined by rectangular areas $10\ m$ across, with material properties distinct from the surrounding rock layers. The faults are modelled in this way in order for fluid to be able to move through them (see Chapter 1.4.1). With the exception of case study 5, the faults are more permeable than other regions and form a pathway for fluid diffusion into the basement. This geometry is shown in Figure 3.2 and the parameters used to construct the geometry are given in Table 3.1. While the geometry is two-dimensional, the system is assumed to extend laterally for $1000\ m$ as part of calculating variables that depend on a third dimension, such as pore pressure propagation relying on a volume of injected fluid. The properties of the simulated layers and faults are given in Table 3.2. These parameters are believed to be typical for the type of rock layers in question. Several measurement points were specified within the mesh geometry to investigate the changes of the pore pressure and stresses during the simulation of the model. In addition to points within and horizontally across from the two faults, there are measurement points in each of the main rock layers, arranged in five columns (Figure 3.2). Each of these columns included measurement points above the shale layer at $y = -3\,000\ m$, within the shale layer at $y = -3\,375\ m$, within the middle layer at $y = -3\,700\ m$, and two within the basement layer at $y = -5\,000\ m$ and $y = -7\,000\ m$, respectively. Note that the value in Table 3.1: Parameters used to construct the model geometry shown in Figure 3.2. Locations of features approximated from Bao and Eaton (2016).Table 3.1 for the fault angle is what was used to construct the simulated geometry and corresponds to a dip angle of $80°$.

The top boundary of the model is free to move and set to a pore pressure of $p = 0$, while the other three sides of the model share boundary conditions. These shared conditions prevent flow across the boundary and movement perpendicular to the boundary but allow movement along the boundary edge. The behaviour of permitting parallel but not perpendicular movement is referred to as a roller boundary.
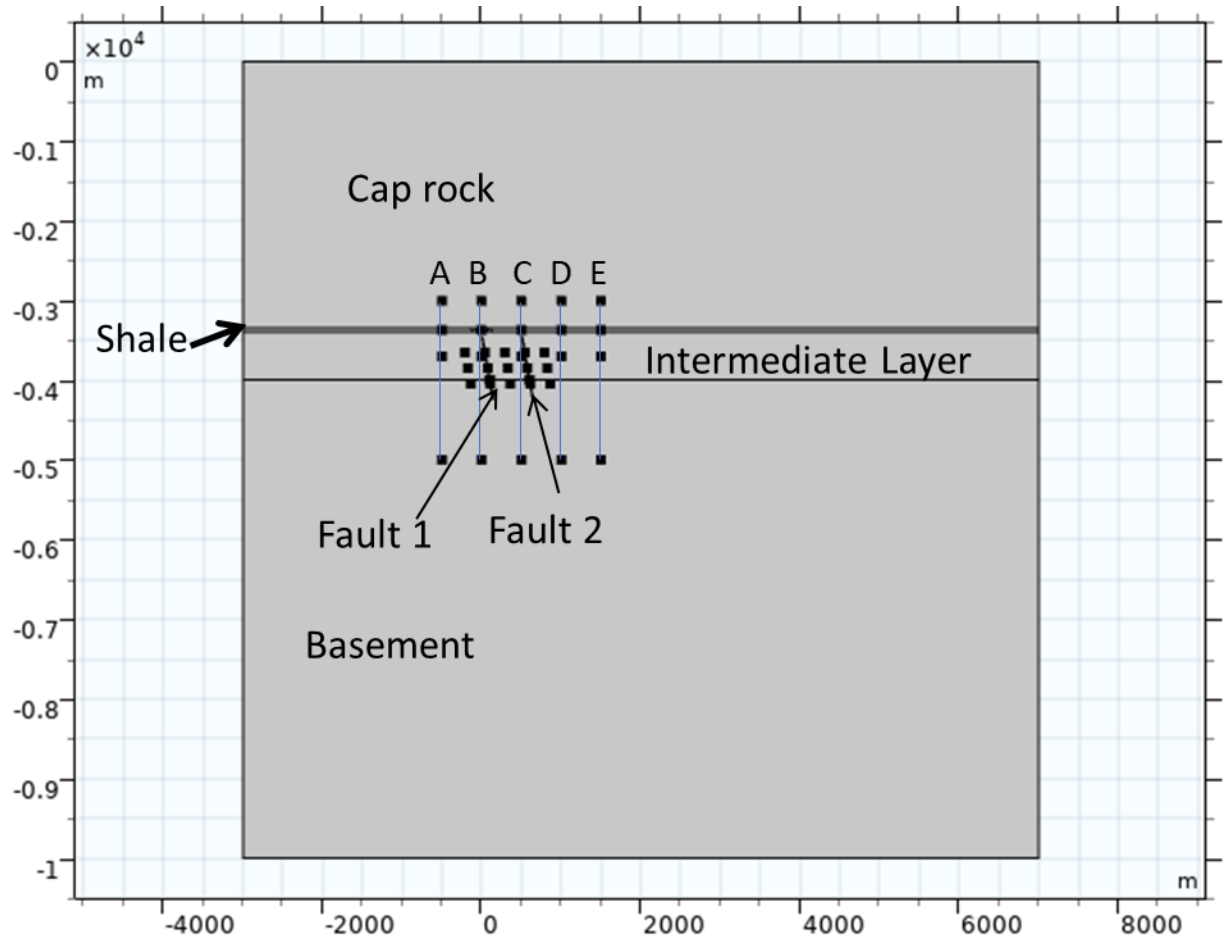
Figure 3.2: Model geometry considered in this study, showing the entire scope of the model, the faults (Fault 1 and Fault 2), the layers of differently modelled rock, and the five columns of measurement points A-E. The injection wells are within the reservoir near column B but are too small to be distinct at this magnification. The area near the injection wells can be seen in more detail in Figure 3.3. The simulated area shown in this figure is much larger than the area shown in Figure 3.1 in order to minimize possible boundary effects.

Table 3.1: Parameters used to construct the model geometry shown in Figure 3.2. Locations of features approximated from Bao and Eaton (2016).

Parameter	Value	Parameter	Value
Horizontal length of model (m)	10000	Fault 2 centre x (m)	575
Starting x position of model (m)	-3000	Fault 2 centre y (m)	-3850
Full model width (m)	1000	Fault 2 length (m)	800
Height of cap rock (m)	3350	Fault angle (°)	100
Width of shale layer (m)	50	Injection well height (m)	-3375
Width of intermediate layer (m)	600	x-Midpoint between two wells (m)	0
Height of basement rock (m)	6000	Distance from midpoint to well (m)	100
Fault thickness (m)	10	Size of enhanced mesh area (m)	25
Fault 1 centre x position (m)	75	Spacing for measurement points tied to fault location (m)	250
Fault 1 centre y (m)	-3850	Starting x position for fixed measurement points (m)	-500
Fault 1 length (m)	800	Spacing between fixed measurement columns (m)	500

Table 3.2: Material properties used for simulation. Parameters marked with [A] are from Chang and Segall (2016), while other Skempton coefficients (marked with [B]) are from Deng et al. (2016). Other parameters have been selected as being reasonable values based on knowledge of typical rock masses. Most values are similar to Chang and Segall (2016).

	Shale layer	Basement	Other rock layers	Fault[A]
Density $\rho \left(\frac{\text{kg}}{\text{m}^3}\right)$	2 500	2 900	2 500	2 500
Poisson ratio ν $(-)$	0.25	0.2	0.25	0.2
Young's Modulus E (MPa)	25 000	66 000	40 000	14.4 000
Biot-Willis coefficient α $(-)$	0.9	0.23	0.4	0.8
Porosity ϕ $(-)$	0.2	0.2	0.2	0.02
Permeability κ (m^2)	10^{-16}	10^{-18}	10^{-15}	10^{-13}
Skempton Coefficient[B] B $(-)$	0.75	0.75	0.75	0.75

3.2.2 Finite-Element Calculations

This simulation made use of the fully coupled model described by Equations (2.29) and (2.35). The solid stresses and pore pressure were calculated separately following Equations (2.27) and (2.35), which are then combined into the Coulomb Failure Stress. The CFS was then recorded, alongside its components: the pore pressure, shear stress, and normal stress.

These calculations were done on a mesh of elements using the commercially available finite-element software COMSOL 5.4 (Figure 3.3). The mesh was constructed using the preset options from this software. Most of the model domain uses the "average" resolution option, while near the injection wells uses the "fine" option so that fluid

propagation from the point sources proceeds in a circular pattern within the reservoir. The total mesh is composed of 10452 triangular elements, 925 edge elements, and 72 vertex elements. Data was extracted with a time step of 0.1 $days$ during the simulations. The simulation begins at $t = 0\ days$ with no movement or stress applied to the system and pore pressure set to $0\ MPa$ throughout.
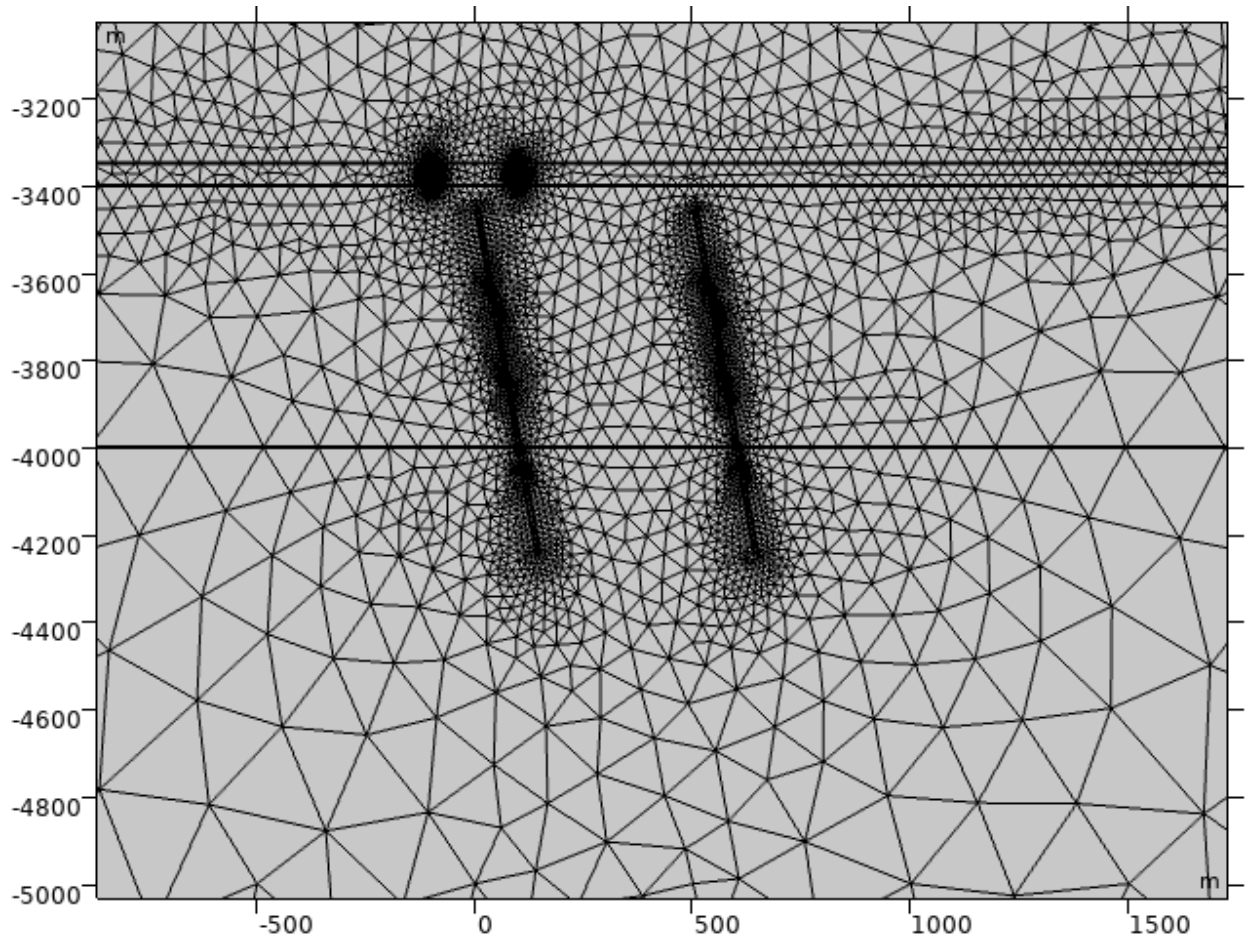
Figure 3.3: Simulation finite-element mesh of the area near the injection wells and faults. More elements have been included near the locations of the injection wells.

3.2.3   Injection Parameters

The injected fluid in this system matches the values used in Chang and Segall (2016), with a density of $\rho_f = 1000\ \frac{kg}{m^3}$, a viscosity of $\eta = 0.001\ Pa \cdot s$, and a compressibility of $4 \cdot 10^{-10}\ Pa^{-1}$. Injection followed a similar procedure to the field

experiment described in Bao and Eaton (2016). There were two time periods in which injection occurs, from $t = 6\ days$ to $t = 10\ days$ and from $t = 19\ days$ to $t = 28\ days$. During both periods, the two wells were injected into simultaneously, and injection was continuous within these periods. The combined injection rate during these periods was $2015\ \frac{m^3}{day}$. This rate was determined by examining the average rate from the field work (see Figure 3.4) and dividing by the ratio of the well length in the field (1900m) by the model width used in the simulation. The field procedure included an attempt at recovering fluid from the injection wells after injection had occurred (represented by the dashed segments of the line in Figure 3.4), however the volume of fluid recovered was minimal (Bao and Eaton, 2016), and so recovery through the wells was not considered for this simulation.
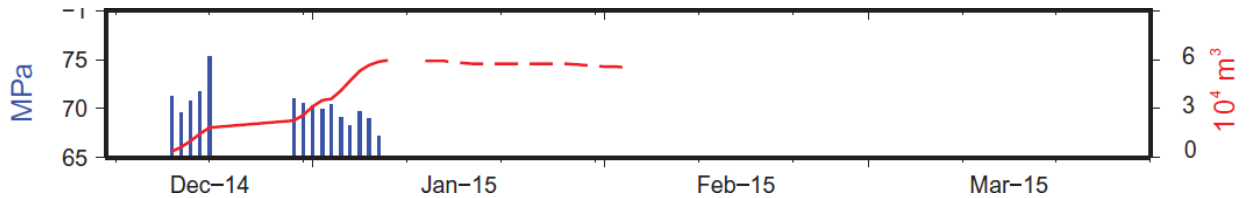
Figure 3.4: Injection data from Bao and Eaton (2016). A solid red line indicates the total injected volume, which was used to determine the injection rate for this work. A red solid line indicates the total injected volume, which was used as the basis for the injection rate in this work. The dashed section of the red line indicates the small reduction in injected fluid from recovery operations.

3.2.4   Fault Slip Parameters

While the faults surrounding the Duvernay formation are primarily strike-slip (Igonin et al., 2021), a vertical 2D cross-section is not capable of modelling movement outside of its plane. As such, this model applies movement on the fault as if it were in normal and reverse faulting regimes instead. A strike-slip model of a fault affected by the fluid injection into the Duvernay shale is modelled in Chapter 4.

In order to determine when the fault slip should occur, the change in CFS, determined by Equation (2.42) within the fault is examined. Once the CFS reaches a threshold of $\Delta S = 0.05\ MPa$, a value capable of triggering earthquakes (King et al.,

1994), slip is introduced on the fault. The slip is modeled as a displacement imposed on each side of the fault. For a fault of length $800\ m$, a 4.0 Magnitude earthquake corresponds to a fault slip of $0.0376m$, with half that value $(0.0188m)$ being applied to each side of the fault (Figure 3.5) (Leonard, 2010). Without any of the variations applied in the case studies detailed below, this threshold is met at $t = 7.2\ days$ (Figure 3.6) within the upper regions of Fault 1. Therefore, the displacement is applied to Fault 1 because the change in CFS is larger than that in Fault 2. Most of the simulations here concern themselves with the case of normal faulting (see Figure 3.5), with the case of reverse faulting being considered one of several variations to the model.
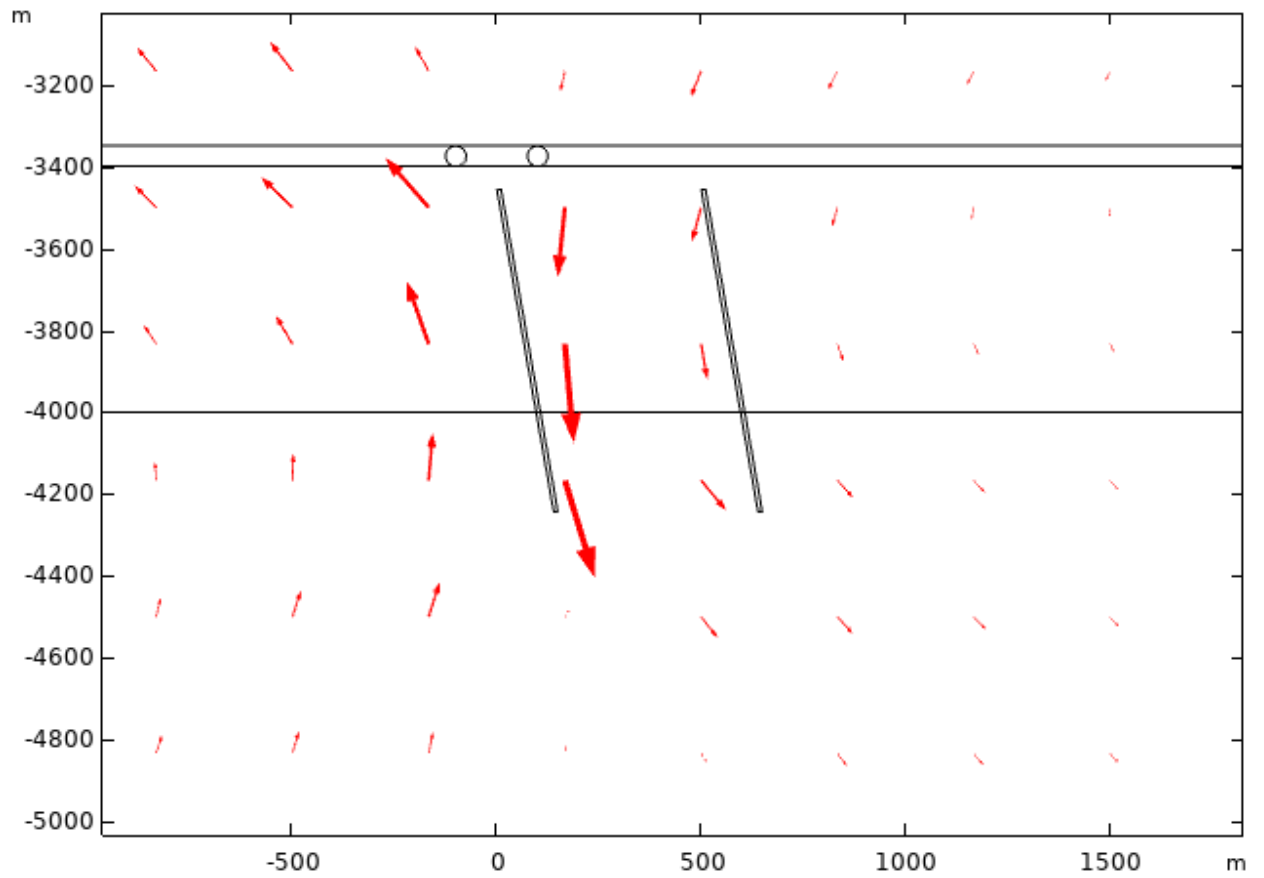
Figure 3.5: Displacement at $t = 8 \; days$, shortly after slip occurs. Arrows show the direction of movement at that point in space, with magnitude of displacement corresponding to arrow size.
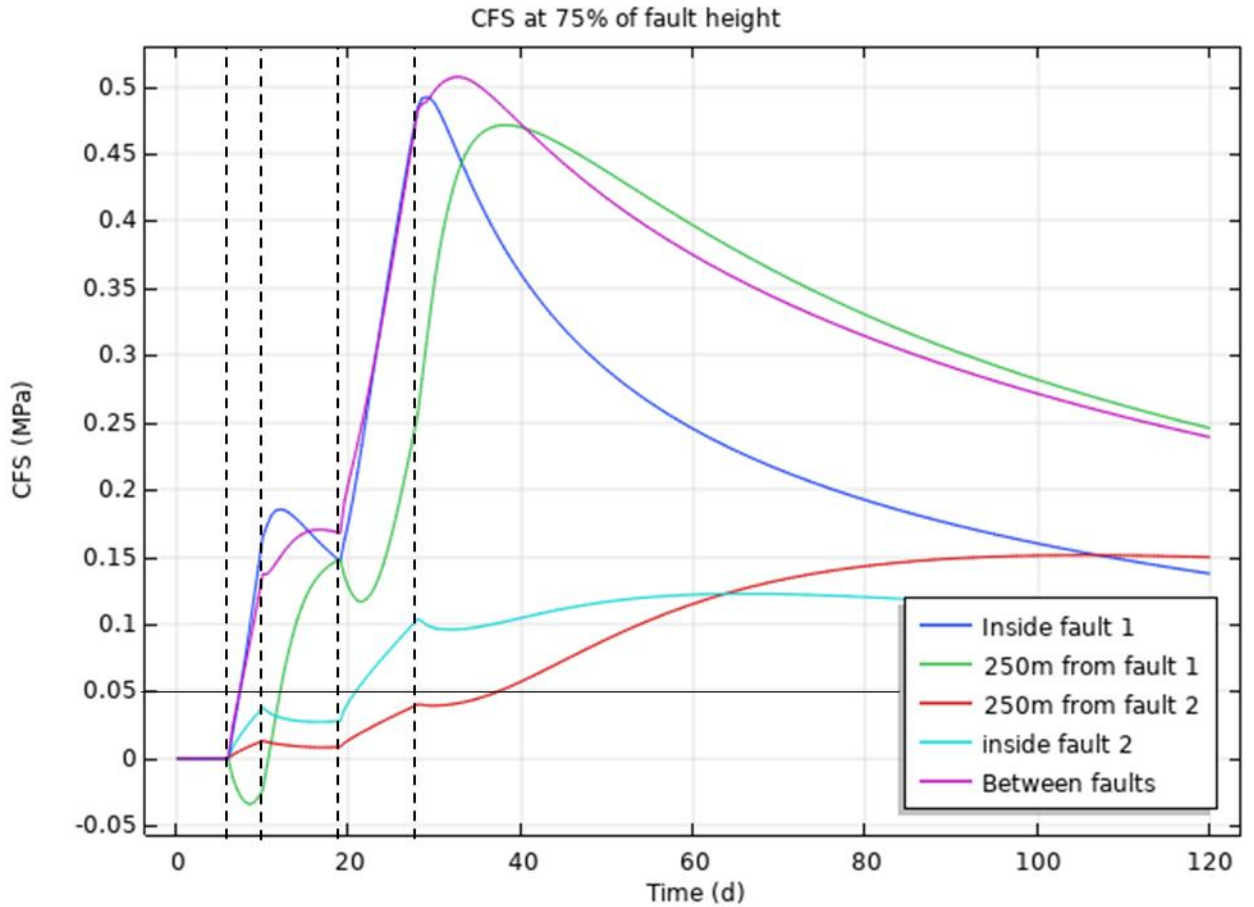
Figure 3.6: Coulomb failure stress at $y = -3653m$, ¾ up the height of the fault with no slip applied. The x-coordinates of the data points were determined relative to the position of the faults at that height and have values of $40.27m$ (within Fault 1), $-207.7m$ ($250m$ outside of Fault 1), $790.3m$ ($250m$ outside of Fault 2) 540.3 (within Fault 2), and $290.3m$ (at the midpoint between faults) respectively. Injection periods are bounded by dashed lines. The slip threshold of $0.05\ MPa$ was passed at approximately $t = 7.2\ days$ within Fault 1, denoted by the black solid line. The CFS peaks within the fault at $t = 29\ days$.

Before the slip, the CFS in the region aligns closely with the pore pressure, shown in Figure 3.7. The slip only impacted the pore pressure very close to the fault endpoints, as seen in Figure 3.8, but had a more noticeable effect on the CFS. The CFS is increased along the length of the fault, while the endpoints have regions of positive and negative changes. The largest regions of negative CFS are in line with the fault, with much smaller

ones approximately 120° from that angle (Figure 3.8). The slip-induced changes are more difficult to distinguish near the injection wells since they are partially masked by the high stresses resulting from injection.

A)
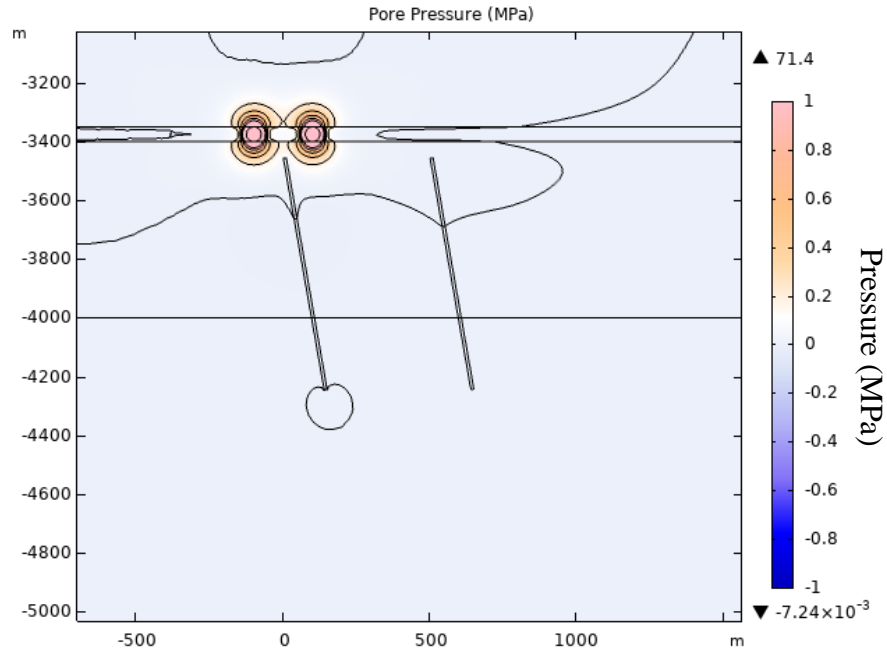
B)
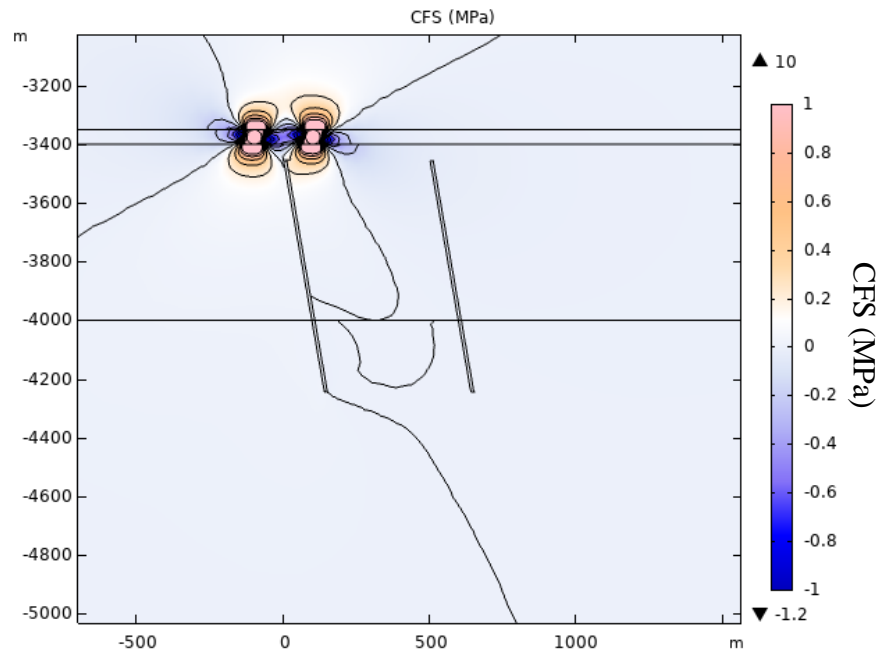
Figure 3.7: (A) Pore pressure and (B) Coulomb Failure Stress immediately before slip is applied to Fault 1, at $t = 7$ days. Contour lines are spaced every $0.2\ MPa$ in the range between $-1\ MPa$ and $1\ MPa$, including those endpoints.

A)

B)
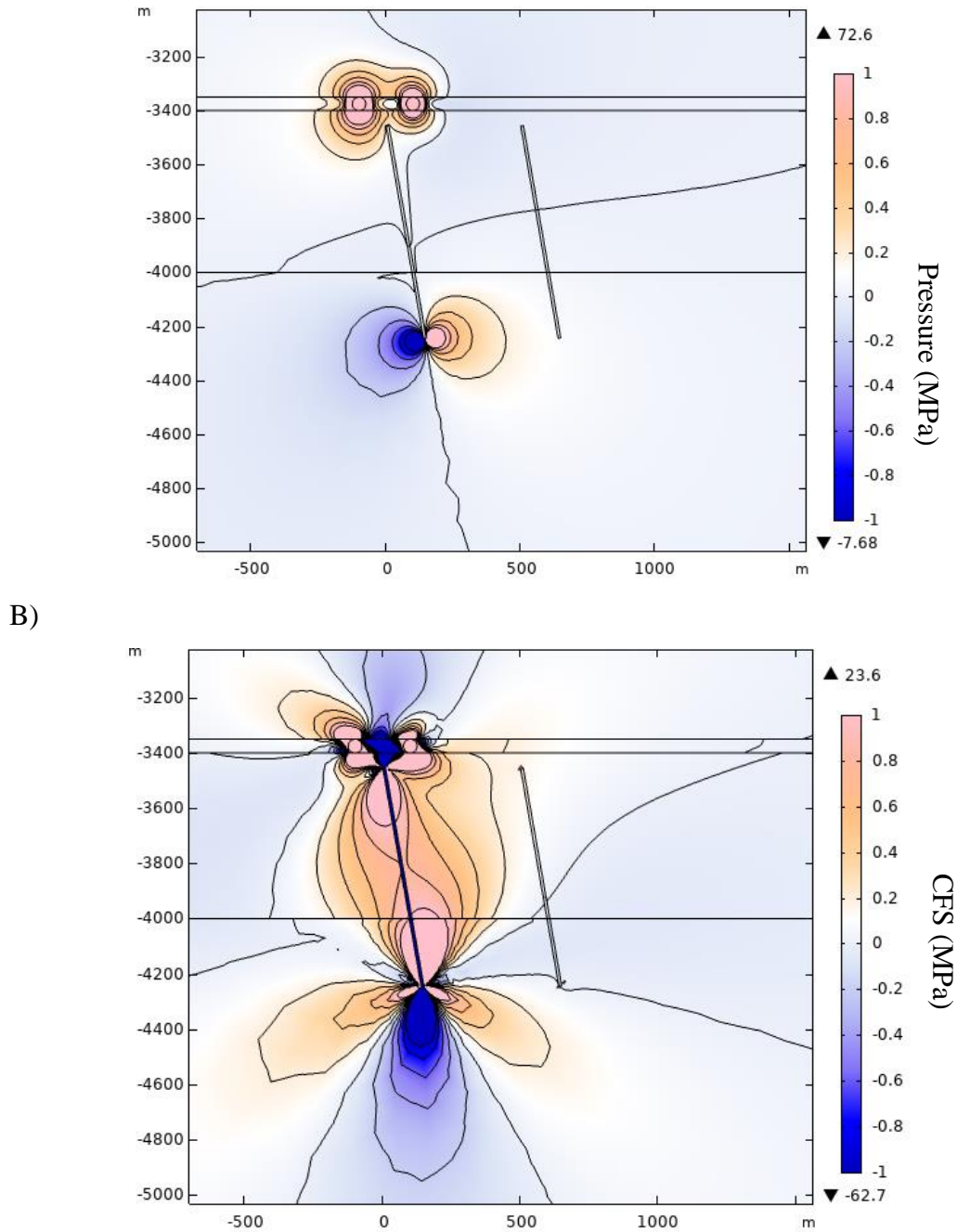
Figure 3.8: (A) Pore pressure and (B) Coulomb Failure Stress after the fault slip occurs, at $t = 8\ days$. Contour lines are discontinuous at boundaries between layers as a result of the layers having different properties.

3.2.5   Seismic Activity Rate Calculation

Seismic activity rate was calculated using the MATLAB function `ode45`, using Equation (2.49). The function is set with an absolute tolerance of 10^{-9}, a relative tolerance of 10^{-8}, and assuming a nonnegative solution. An input file is read containing the CFS at specified times and special coordinates from the finite-element model described above. For this model, the data is separated by time steps of 0.1 days and covers a square area $2000m$ on a side, centred about $(500m, -4000m)$. The data points in this area are spaced by $10m$ in both the x- and y-directions.

Equation (2.49) is then solved for each point, and the rate is displayed for the area at a specified time. Equation (2.50) was also tested but produced the same results for a single set of input parameters.

3.3   Case study 1: Seismic Activity Rate Parameters

In addition to the CFS generated by the geomechanical model, the seismic activity rate also depends on the other two parameters of Equation (2.49), t_a and A_σ. t_a, the characteristic decay time of the system, determines how quickly the activity rate subsides after a disruption to the stress state occurs. A_σ is a composition of the background stress and the constitutive parameter of the rate-and-state law. These parameters need to be examined to ensure the activity rate takes on reasonable values.

Several values of A_σ and t_a were tested in order to determine what values the parameters should have for the other case studies. All of these tests use the same CFS data obtained from the model described in Section 3.2. Both parameters were set manually for these tests instead of being calculated via equation (2.48).

At low values of t_a, decay can be seen in the activity rate even before the model is affected by the fluid injection or slip (Figure 3.9). That behaviour was deemed inappropriate for examining the effects of injection and slip, and so t_a values less than $10^4 \; days$ were rejected for further tests. Values of t_a higher than $10^4 \; days$ did not appear to significantly affect the activity rate during the simulation period (Figure 3.9), so $10^4 \; days$ was used as the baseline for further case studies. This figure is within the same

order of magnitude as the reference case used in (Chang and Segall, 2016) of $50\ years$ or approximately $1.8 \times 10^4\ days$.
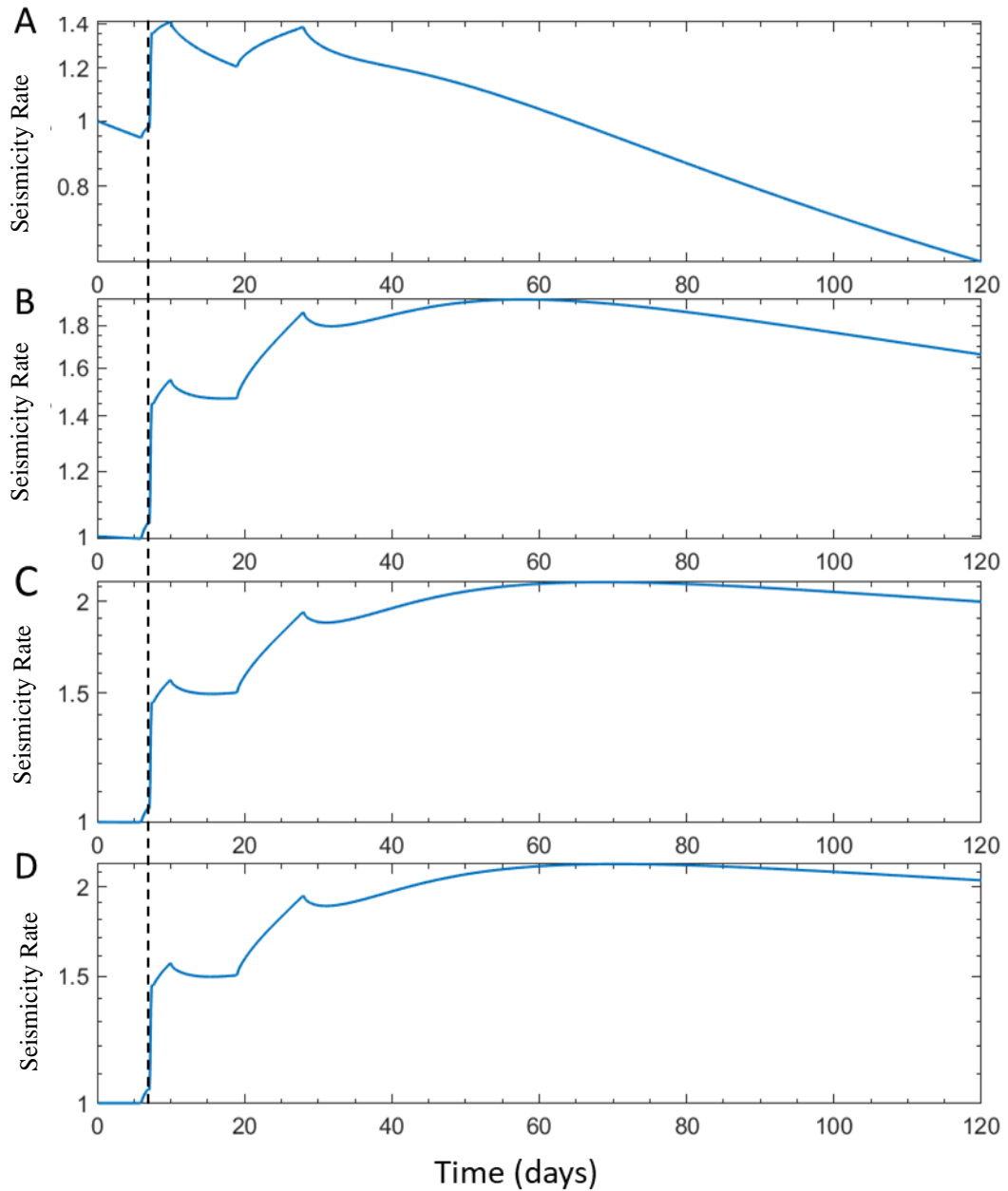
Figure 3.9: Comparison of the activity rate for (A) $t_a = 100\ days$, (B) $t_a = 1\ 000\ days$, (C) $t_a = 10\ 000\ days$, and (D) $t_a = 100\ 000\ days$. A_σ remains $0.3\ MPa$ in all instances. This data was taken at the midpoint of Fault 2, at $(375m, -3850m)$. The timing of the fault slip is denoted by a dashed line.

The magnitude of the calculated rate is sensitive to changes in A_σ, with the rate changing by orders of magnitude with a $0.1\ MPa$ change in A (Figure 3.10). Higher values of A_σ led to decreased activity rates, and lower values of A_σ led to increased activity. A value of $A_\sigma = 0.3\ MPa$ was selected since it produced only small areas where the calculated rate exceeded $R = 100$, even soon after slip occurs (Figure 3.11).
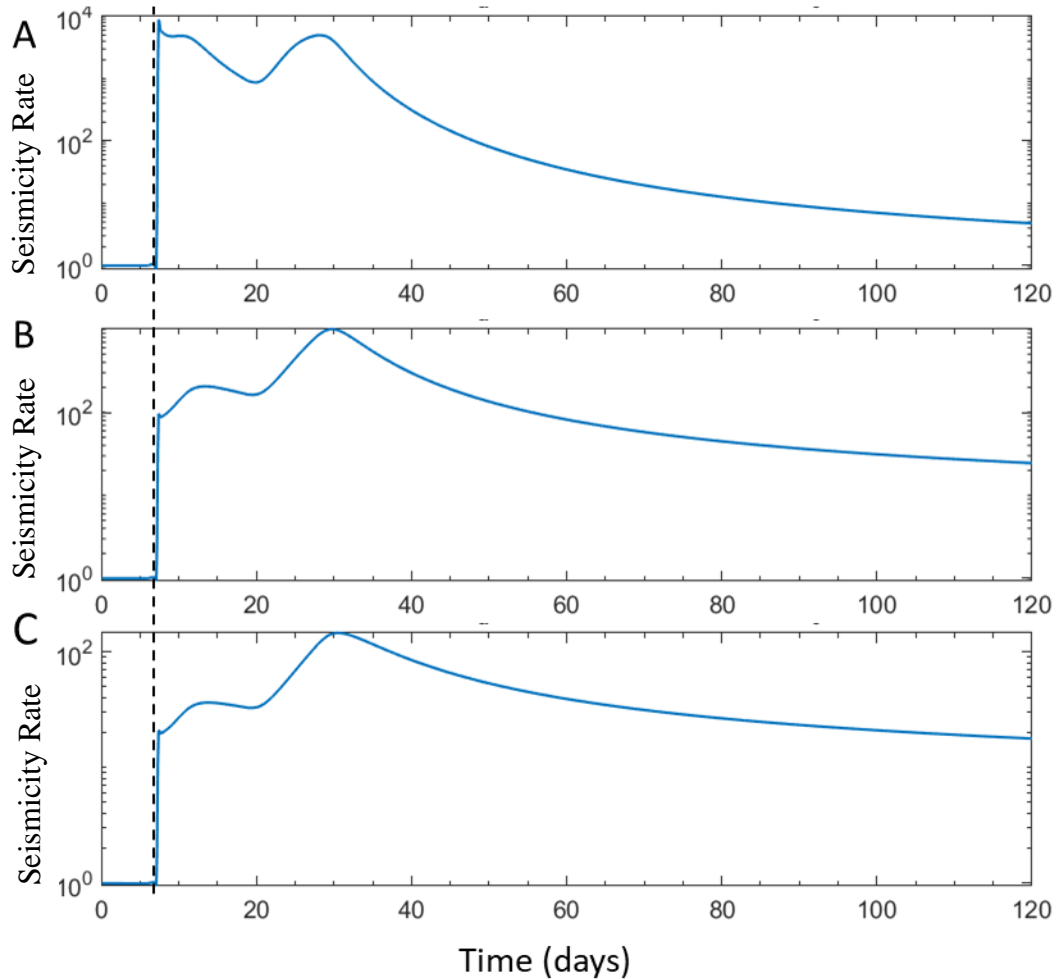
Figure 3.10: Comparison of activity rate over time for A_σ values of (A) $0.1\ MPa$, (B) $0.2\ MPa$, and (C) $0.3\ MPa$. t_a was set to $10\ 000\ days$, and data was gathered at the measurement point nearest the middle of Fault 1, at $(0, -3700)$. Fault slip is denoted by a dashed line.
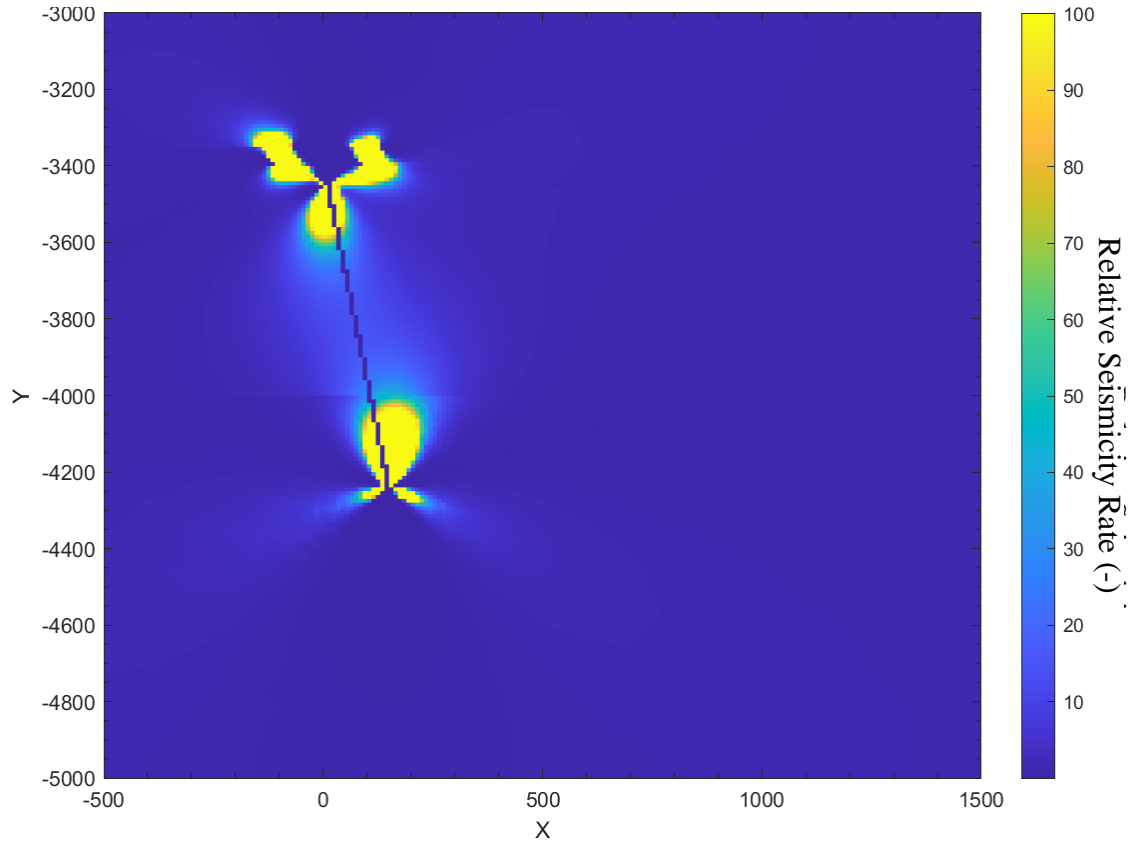
Figure 3.11: Calculated activity rate for $t = 8\ days$, shortly after fault slip. This calculation uses $t_a = 10\ 000\ days$ and $A_\sigma = 0.3\ MPa$. Sites of high activity are shown with yellower pixels, with the scale given on the right.

These values of $t_a = 10^4\ days$ and $A_\sigma = 0.3\ MPa$ are used for the following case studies, as well as those presented in Chapter 4. This corresponds to approximately a background Coulomb stressing rate of $\dot{S}_0 = 10^{-5}\ \frac{MPa}{day}$, a background normal stress of $\sigma_0 = 50\ MPa$, and a rate-and-state constitutive parameter of $a = 0.0086$.

3.4   Case Study 2 and Case Study 3: Variations in the Amount of Slip on a Fault and the Slip Timing

One of the parameters being examined was the stress change required to apply slip on the main fault. Instead of the $0.05\ MPa$ threshold used for the other case studies, the slip is imposed at the time the CFS peaks within the upper region of the fault, at $t =$

$29 \ days$ (Figure 3.6). These are the only simulations done with altered timing for the slip on the fault. Two simulations were run with this timing. One of them maintained the slip magnitude of $0.0376 \ m$ the same as in the other simulations, while the second doubled the slip magnitude to $0.0752 \ m$ to reflect the triggering stresses being higher. The stress state after the slip in both cases is shown in Figure 3.12. Larger slip produces larger stress changes, as expected, and this increased stress change also corresponds to an increase in activity rate (Figure 3.13). The long-term behaviour of the activity was not significantly affected for the case of a later slip with the same magnitude compared to Case Study 1 (see Figure 3.14).

A
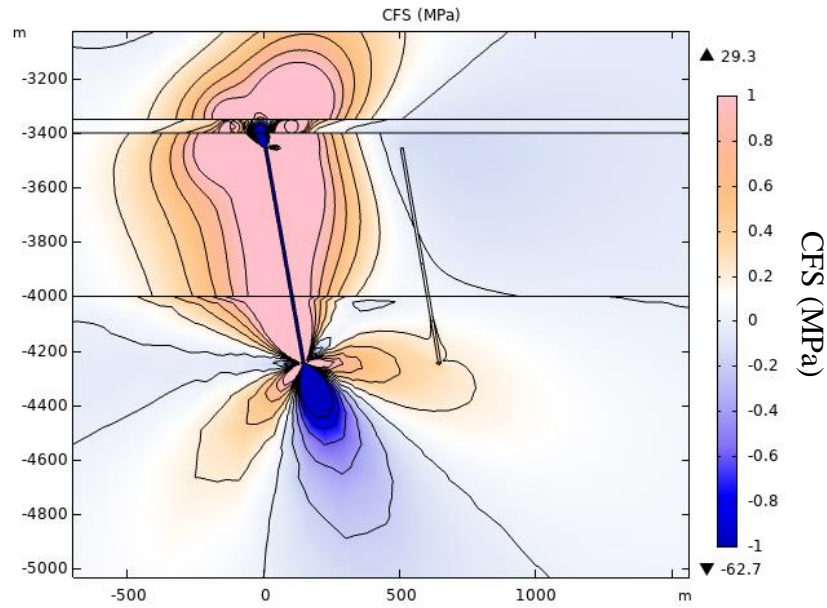
B
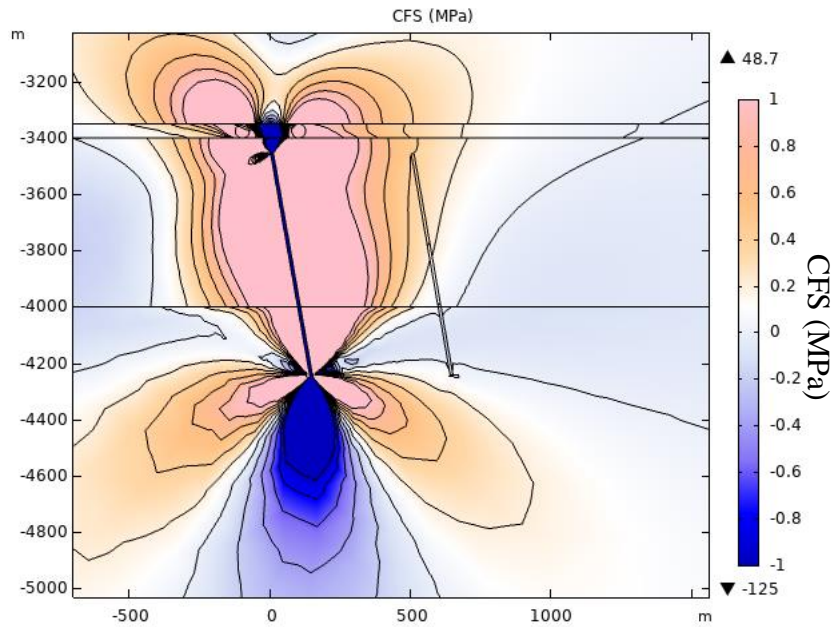
Figure 3.12: Comparison of CFS after an (A) $0.0376\ m$ and (B) $0.0752\ m$ fault slip, at $t = 30\ days$. Despite the wider scale in B, an increased area affected by stress changes is still visible. Near the injection wells, the larger slip begins to have a significant effect despite the high pressure-related stresses.

A)
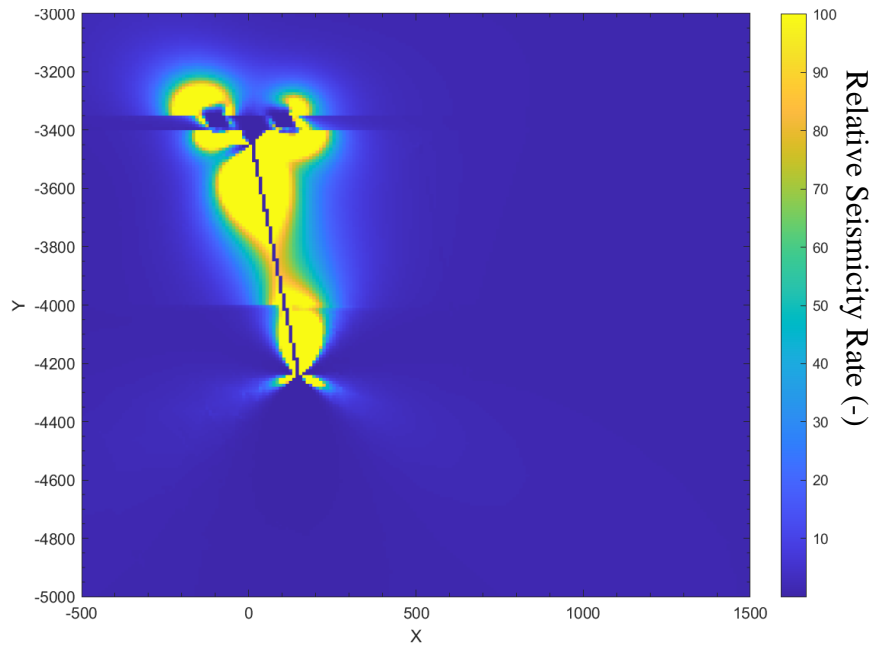
B)
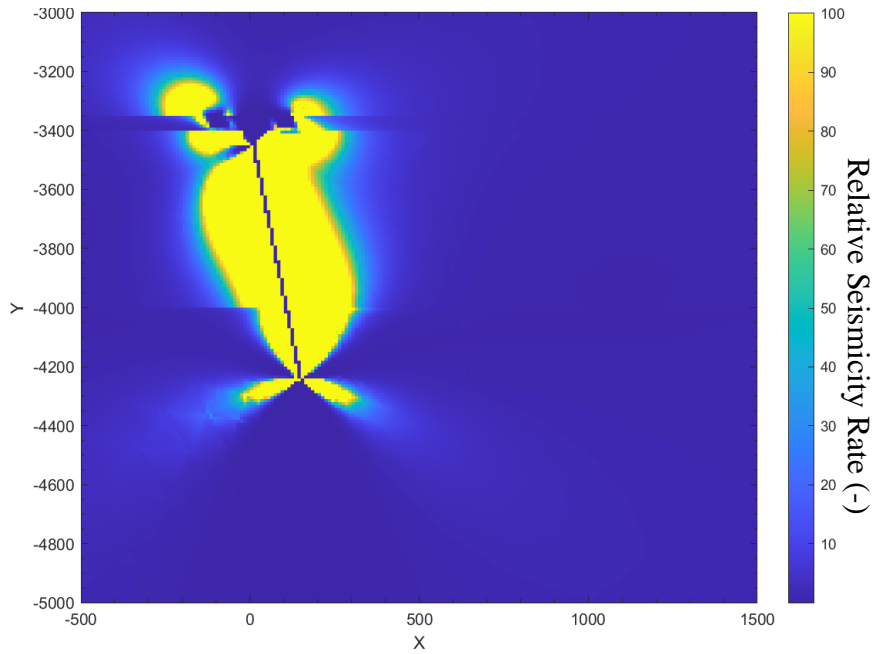
Figure 3.13: Comparison of seismicity rate for a slip occurring at $t = 29\ days$, for slip magnitudes of (A) $0.0376\ m$ and (B) $0.0752\ m$. Both snapshots were taken at $t = 30\ days$.
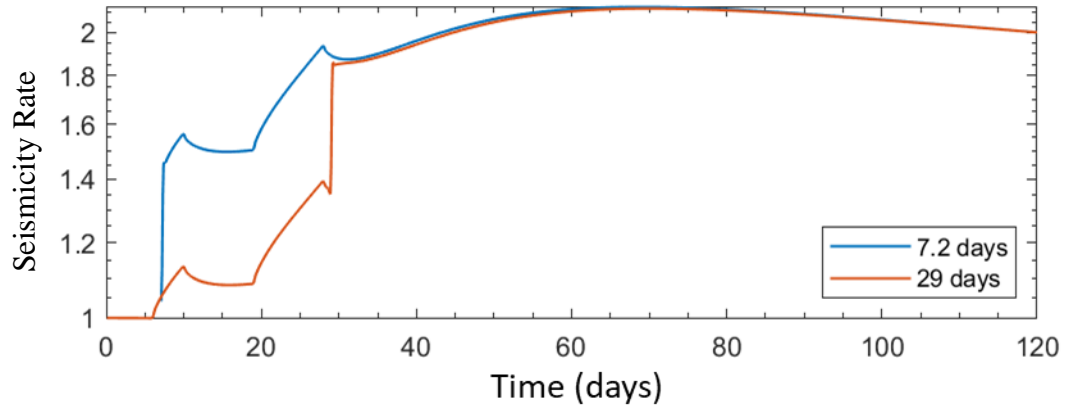
Figure 3.14: Comparison of activity rate over time at the midpoint of Fault 2 under different slip timings. The slip is set to $0.0376m$ in both instances.

3.5   Case Study 4: Reverse slip on the Fault

Another case simulated is that of reverse faulting. The slip timing and magnitude are unchanged from the primary model, only the direction of slip is changed. The displacement after the slip is shown in Figure 3.15. The pressure propagation from the injection wells changes little compared to the base case (See Figure 3.8A and Figure 3.16). Under the assumption that the rest of the model is prone to slip in the same direction as the fault, the change from normal to reverse faulting only changes the angle of the regions of positive and negative CFS (see Figure 3.8B and Figure 3.17). However, this angle change does move a region of positive stress farther away from Fault 2.
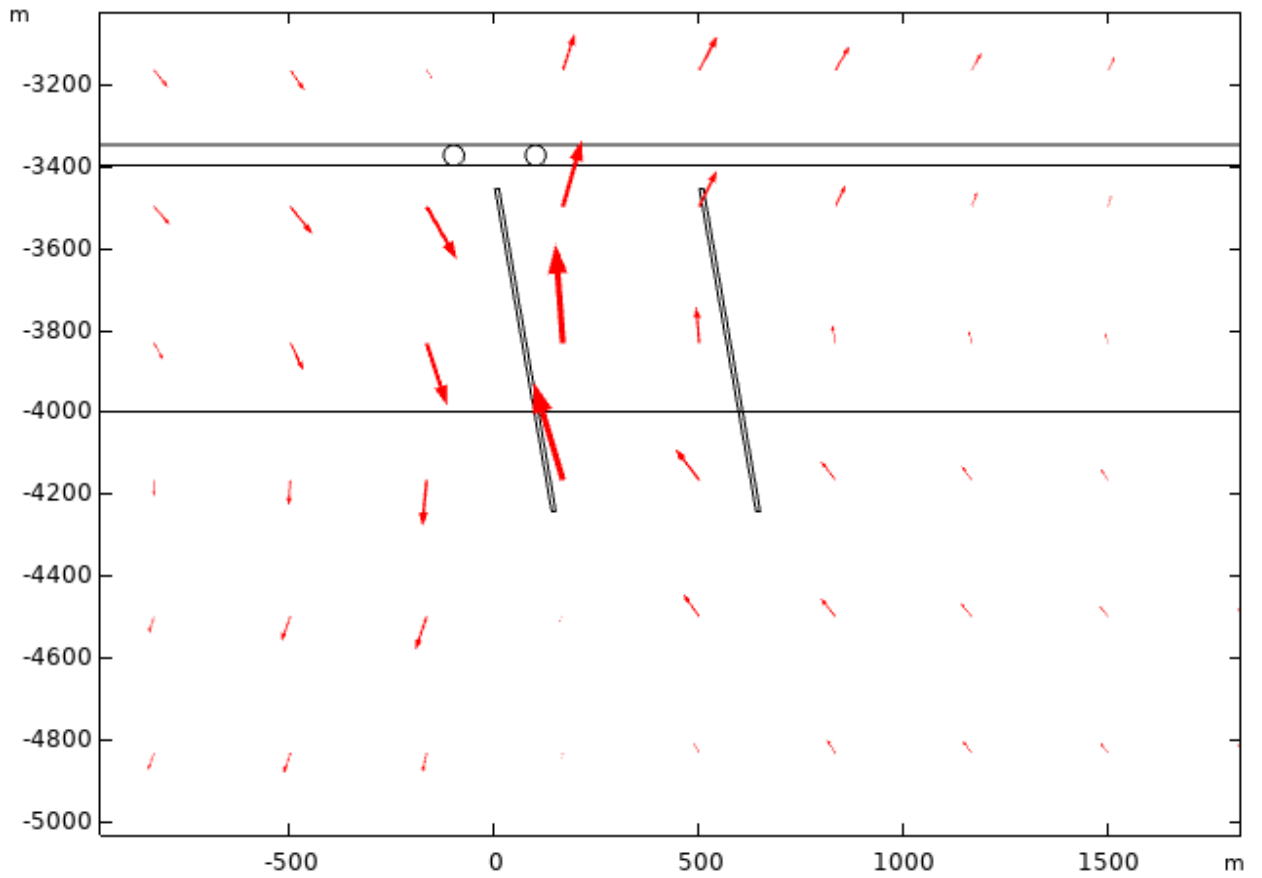
Figure 3.15: Displacement at $t = 8\ days$ for case study 4. Arrows show the direction of movement at that point in space, with magnitude of displacement corresponding to arrow size.
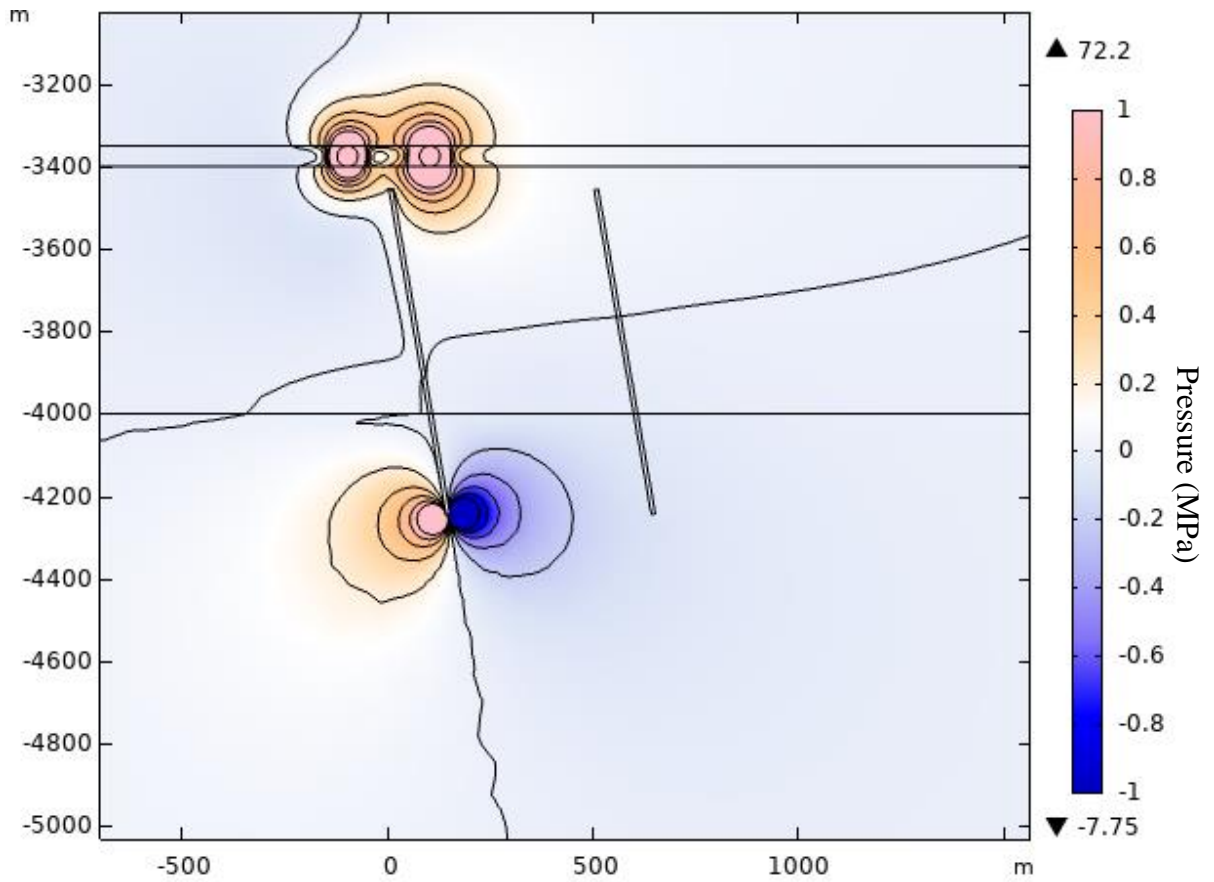
Figure 3.16 : Pore pressure after Reverse faulting at $t = 8$ days. The state near the wells is relatively unchanged, while the lower endpoint has the pressure differential inverted.
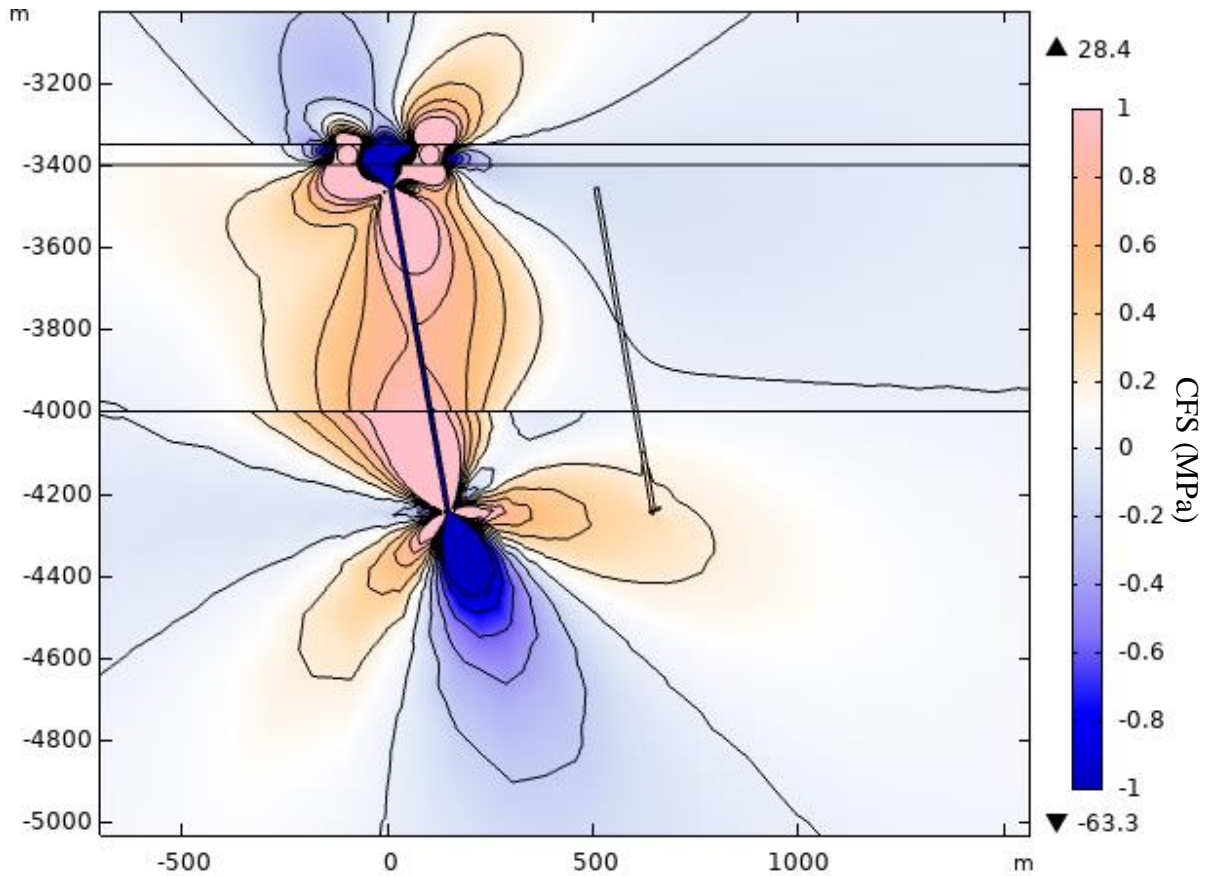
Figure 3.17: CFS after reverse (Case Study 4) faulting with $0.0376\ m$ of slip along the fault, taken at $t = 8\ days$.

3.6　Case Study 5: Non-conductive Faults

For this simulation, the permeability of both faults was decreased to $1 \cdot 10^{-21}\ m^2$, following the data in Chang and Segall, 2016 for a sealing fault. Other simulation parameters, including the slip timing, were not changed. The stress state was similar to that of a conductive fault during the earlier times of the simulation, before large amounts of fluid are able to diffuse out into the intermediate layer and basement (Figure 3.8B and Figure 3.18). However, at later times, the lack of a permeable channel into the basement resulted in fluid remaining within the intermediate rock layer, producing an increase in pore pressure when compared with a conductive fault (Figure 3.19).

In addition to the lack of transfer into the basement, the faults being impermeable also impacted the fluid and stress propagation within the intermediate layer. An

impermeable Fault 2 restricted the fluid from easily moving beyond it, resulting in lower activity at that location (Figure 3.20). Both of these effects lead to the longer-term activity in the intermediate layer between the two faults being higher than for other case studies (Figure 3.21)
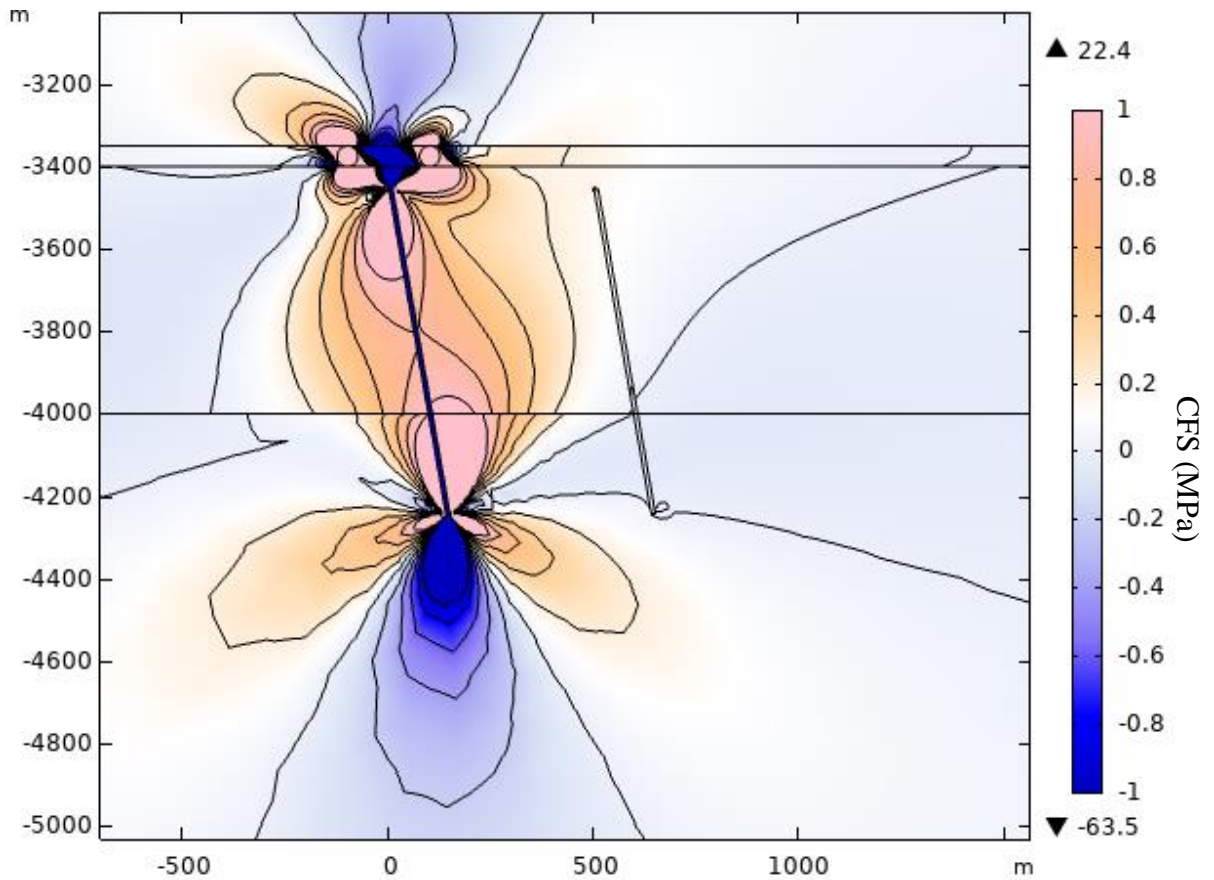
Figure 3.18: CFS at $t = 8\ days$ for Case Study 5. The permeability of the faults has been decreased, restricting fluid movement.

A
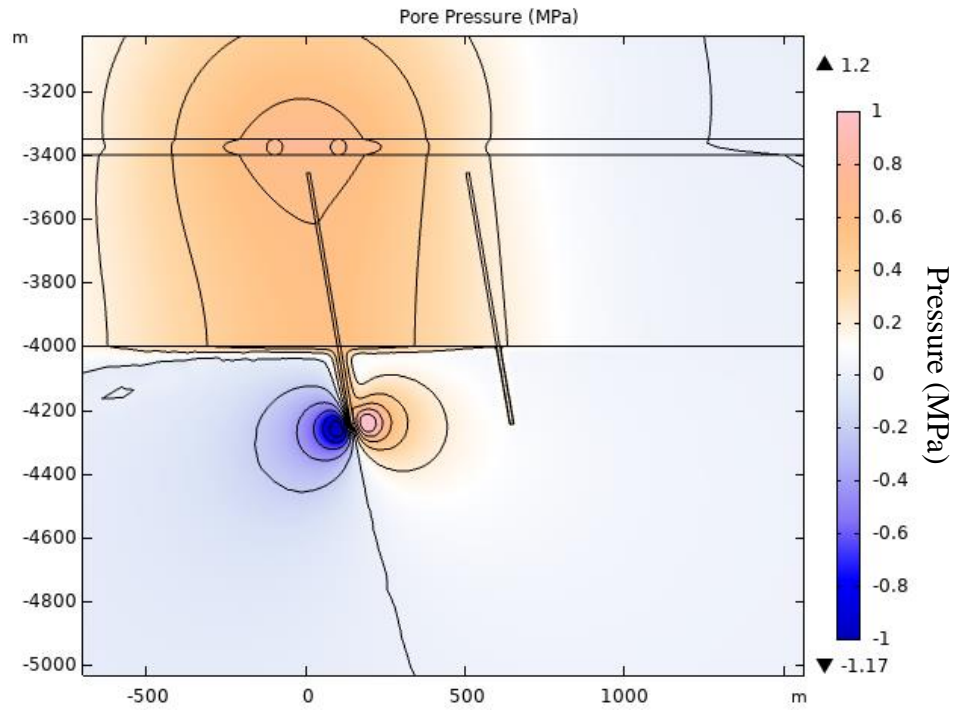
B
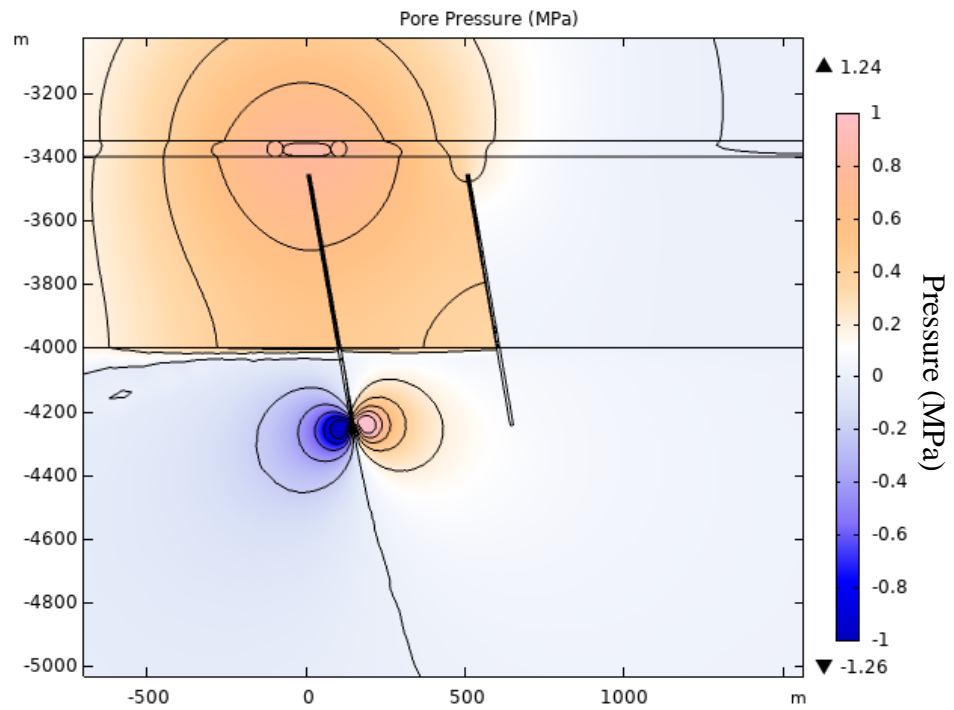
Figure 3.19: Pore pressure at $t = 50 \ days$ for (A) Case Study 1 and (B) Case Study 5.
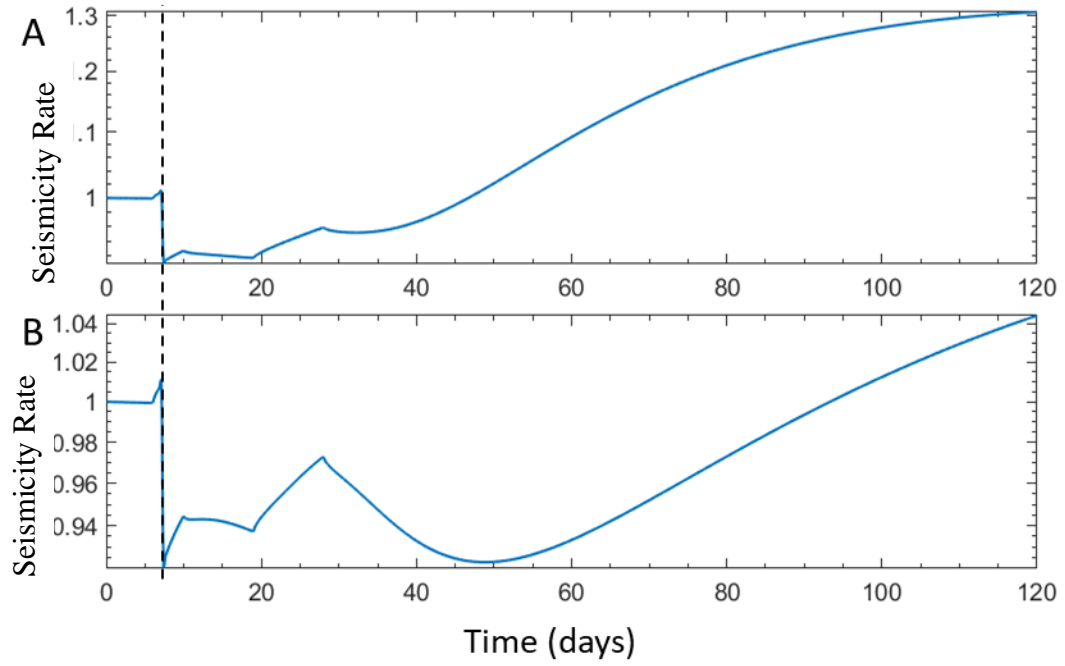
Figure 3.20: Activity rate over time beyond Fault 2 at $(1000, -3700)$ for (A) Case Study 1 and (B) Case Study 5. Slip is denoted by the dashed line.
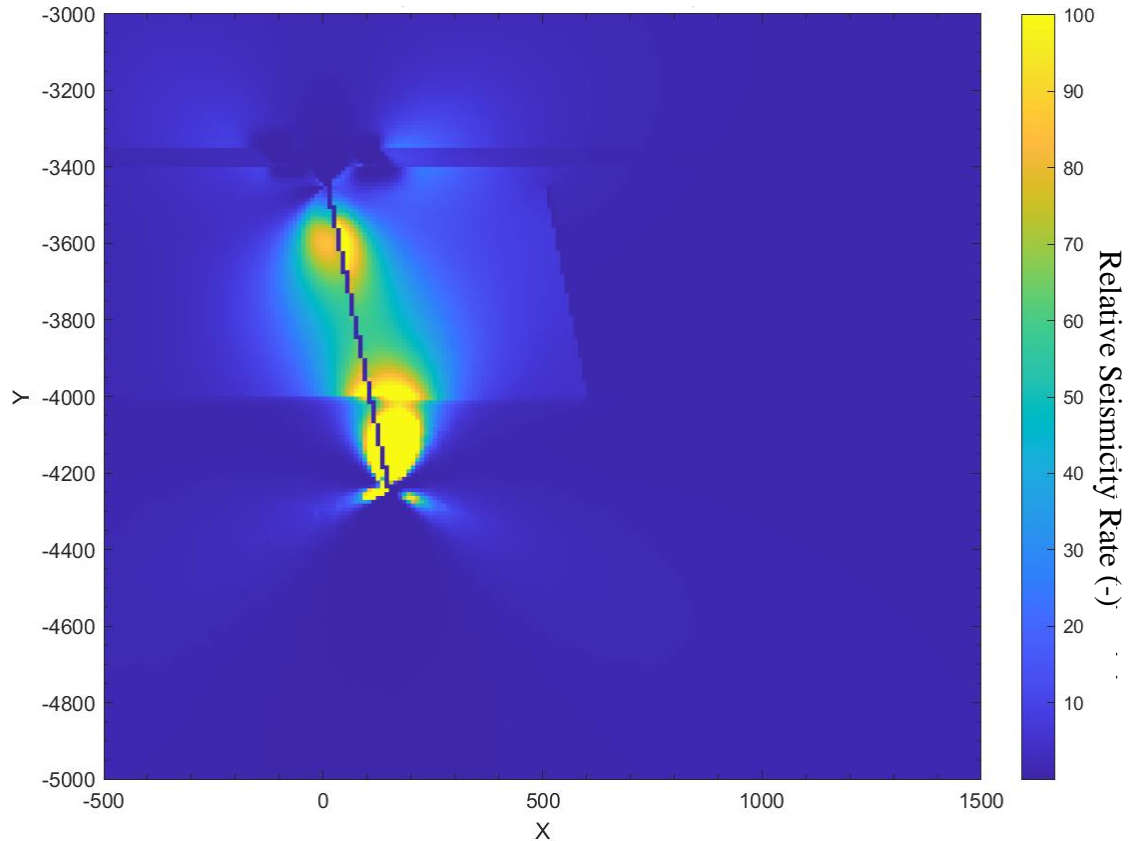
Figure 3.21: Calculated activity rate at $t = 50\ days$ for an impermeable fault.

3.7   Cases Studies 6, 7, and 8: Varying the Angle of the Fault

Simulations were performed for three different orientations of the fault with respect to the horizontal direction. In Case Study 6 the fault was oriented 115° from the horizontal line (Figure 3.22A) and corresponding to a dip angle of 65°, while for Case Study 7, the fault angle was decreased to 85° from the horizontal (Figure 3.22B). Finally, in Case Study 8, the fault angle further decreased to 70° from the horizontal in order to examine a less vertical fault oriented in the new quadrant (Figure 3.22C). As part of the change in quadrants, the angles used for the construction of the latter two Case Studies are equal to the respective dips of the constructed systems. In order to maintain the position of Fault 1 between the two injection wells, the relative position of the faults was adjusted. For Case Study 6, the x-position of the faults was increased by $100m$, while it

was decreased by $75m$ and $175m$ respectively for Case Studies 7 and 9. These altered geometries are shown in Figure 3.22.

A)
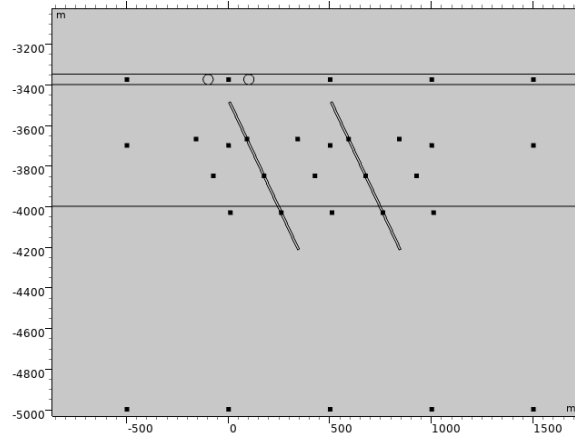
B)
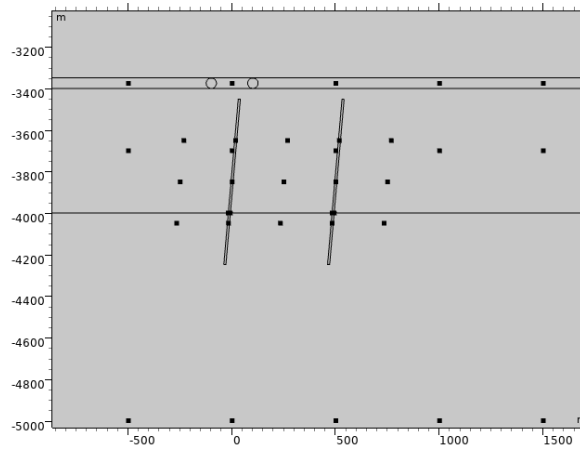
C)
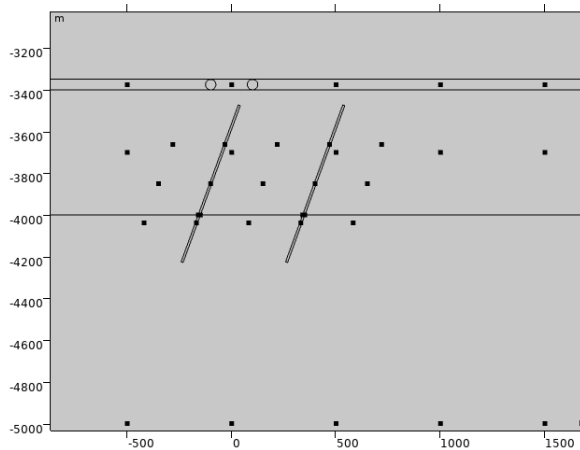
Figure 3.22: Model geometry for Case Studies (A) 6, (B) 7, and (C) 8; displaying the different fault angles and centre positions.

The seismic activity was relatively higher near the edge of the basement on the less-vertical fault compared to the base model (Figure 3.23). This is potentially due to the shallower angle leaving more time and length for fluid to diffuse out of the fault, after which point it has difficulty infiltrating the basement.
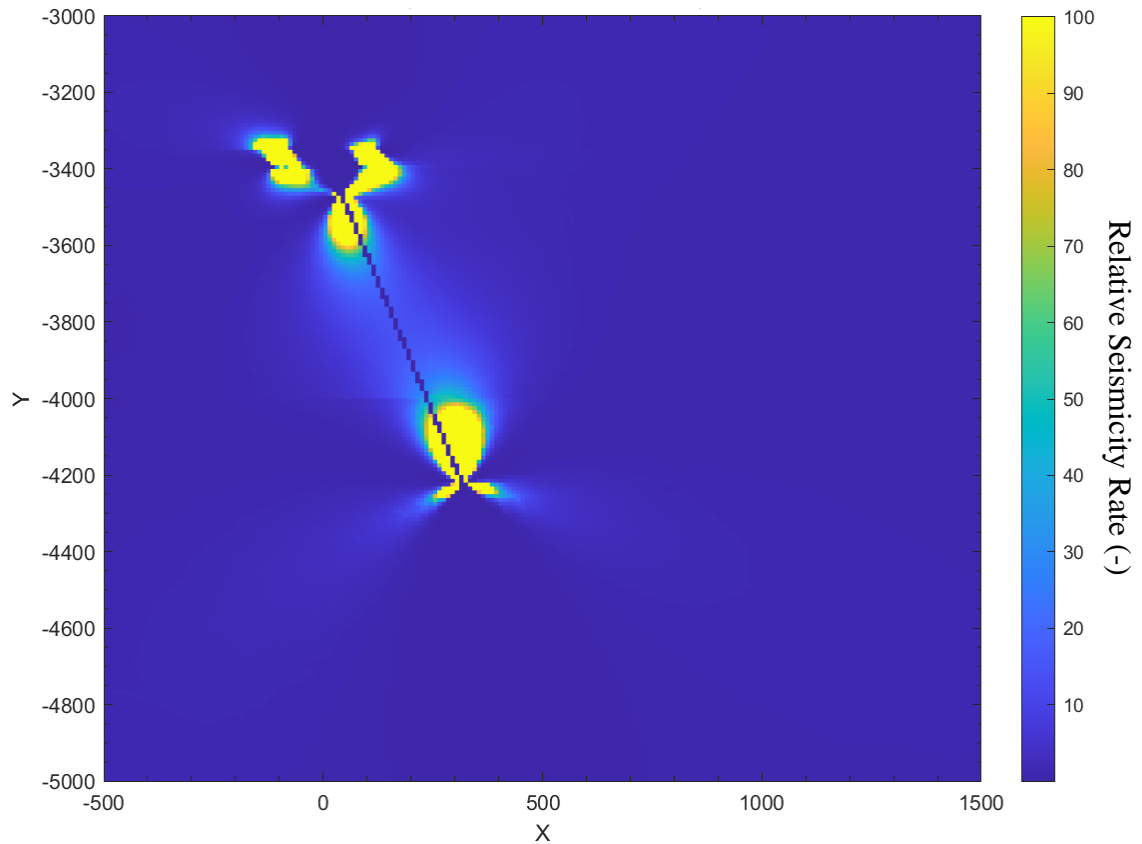
Figure 3.23: Predicted activity rate after slip on a 110° fault (Case Study 8) at $t = 8\ days$.

3.8 Case Study 9 and Case Study 10: Varying the Permeability of the Middle Layers

In order to determine the effects of different permeability in the intermediate rock layers, simulations were performed with the shared permeability of the cap and intermediate regions (Figure 3.2) increased and decreased to $5 * 10^{-15}\ m^2$ and $0.5 * 10^{-15}\ m^2$, respectively. These values were chosen as they are partway to the next order of magnitude. Higher permeability allows for faster diffusion of pore pressure out from

the injection wells and Fault 1. By comparing these cases to each other as well as the permeability of $1 * 10^{-15} \ m^2$ used for the other simulations, it can be noted that areas of increased activity are smaller and closer to Fault 1 when permeability is lower, but the increase in activity is larger. Figure 3.24 shows a comparison between the later activity in Case Studies 1, 9, and 10.

A)
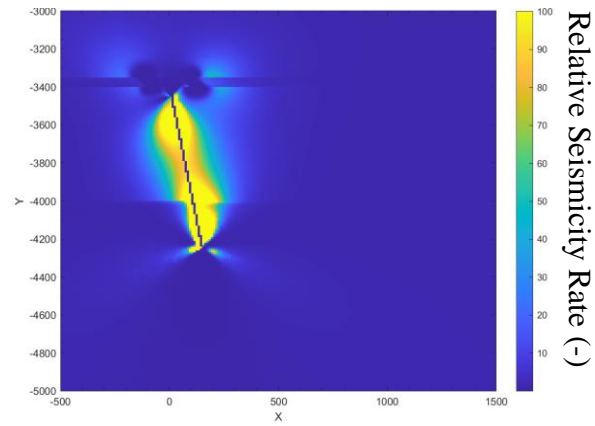
B)
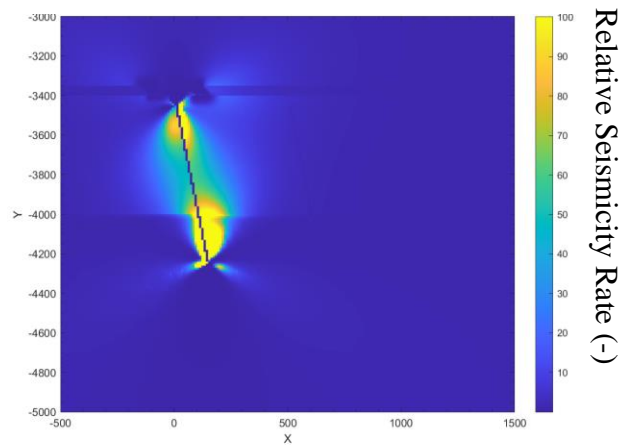
C
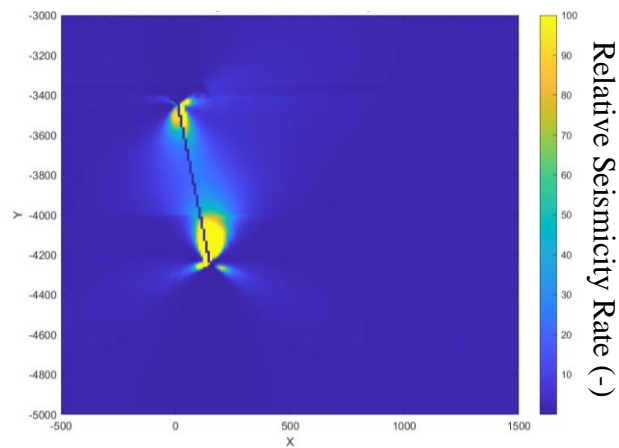
Figure 3.24: Activity comparison after 50 days for Case Studies (A) 9, (B) 1, and (C) 10, arranged in order of increasing permeability for the intermediate layer.

3.9 Case Study 11, 12, and 13: Permeability of the Basement

In addition to the intermediate layers examined in Case Studies 9 and 10, it was also believed that the permeability of the basement would also impact the overall behaviour. Three simulations were performed to test this. In Case Study 11, the permeability of the basement is set to $10^{-15} \ m^2$, matching the middle layer. Case studies instead increase and decrease the basement permeability by a factor of 10, respectively, with values of $10^{-17} \ m^2$ for Case study 12 and $10^{-19} m^2$ for Case Study 13. These changes only slightly affect the pore pressure diffusion from the injection wells but do noticeably impact the decay of the pressure changes resulting from the slip at the bottom endpoint of the fault (Figure 3.25).

A
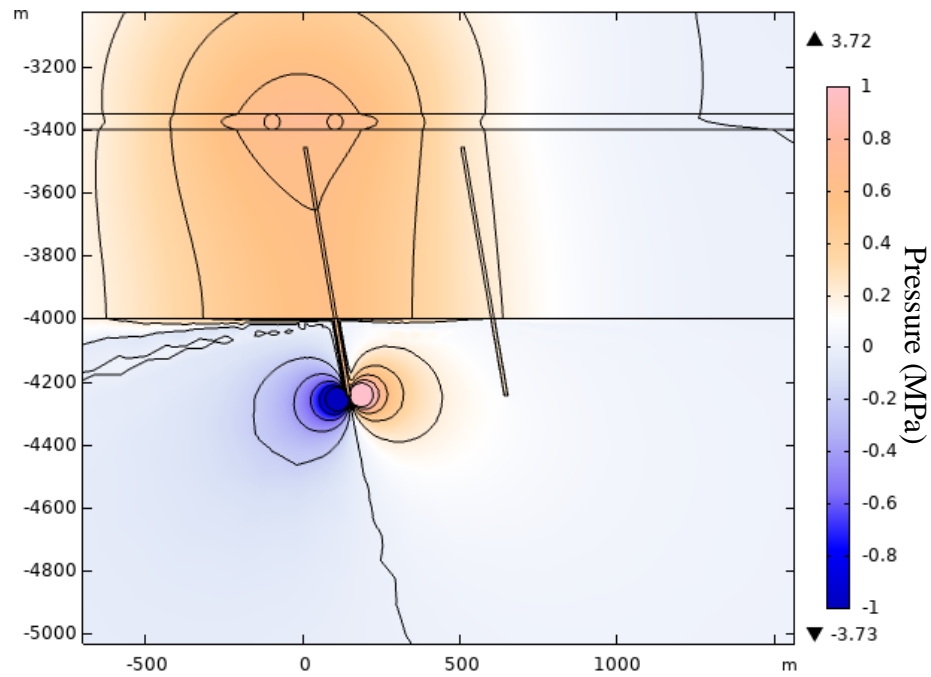
B
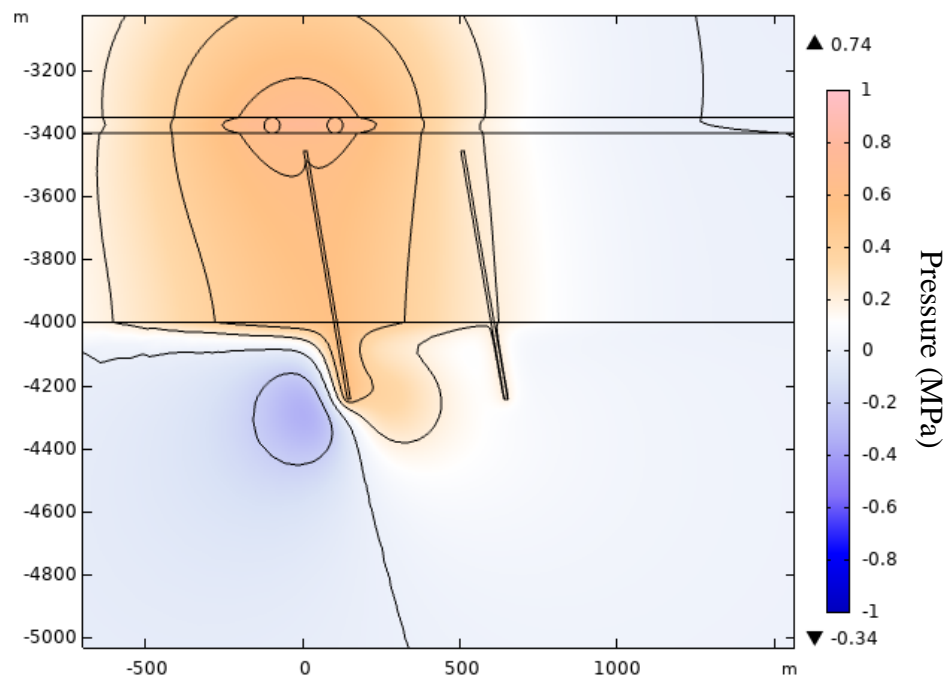
Figure 3.25: Comparison of pore pressure at $t = 50\ days$ for basement permeabilities of $10^{-19}m^2$ (A) and $10^{-17}m^2$ (B). The pressure differential at the lower endpoint is still clearly visible in A, but has nearly vanished in B.

This ended up producing similar effects to the permeability changes in Case Studies 9 and 10, where lower permeability led to more intense and localized areas of high simulated activity, and lower permeability lead to wider areas of less intense activities. (Figure 3.26) However, unlike those Case Studies, the changes in basement permeability only primarily affected the stresses produced inside the basement by the slip.

A
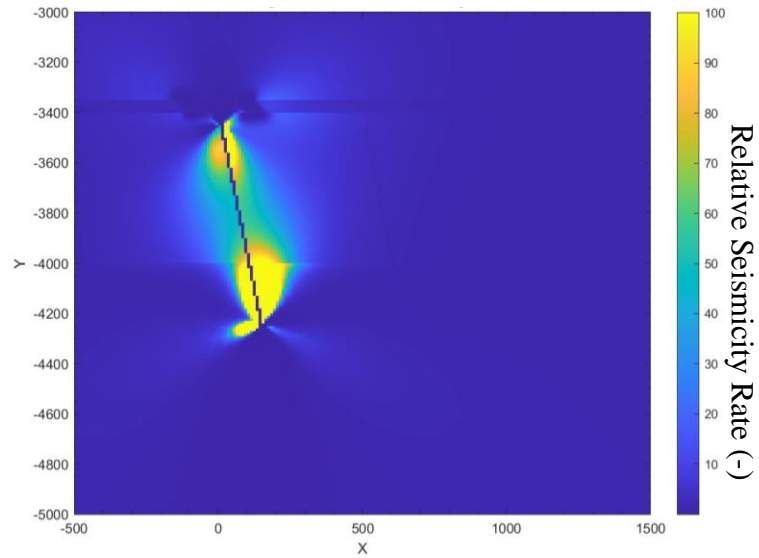
B
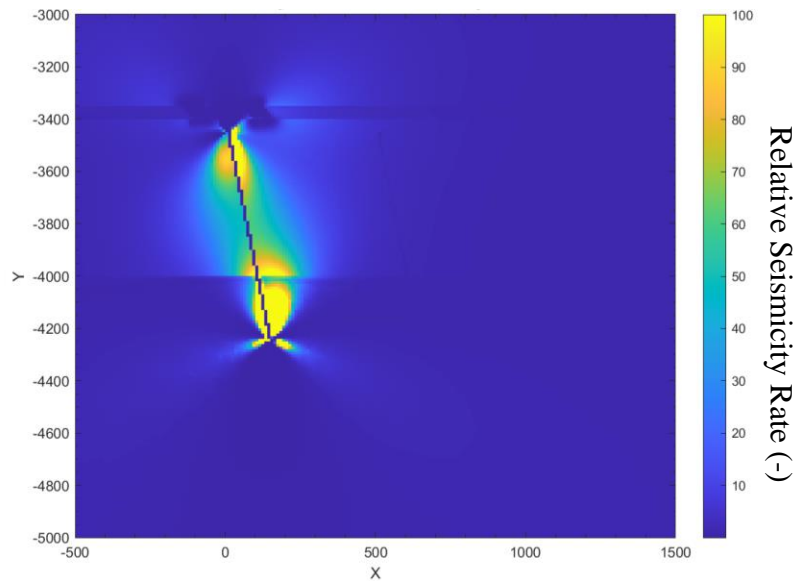
Figure 3.26: Comparison of activity rate at $t = 50\ days$ for Case Stuides 12 (A) and 13 (B).

3.10   Summary

Slip on Fault 1 was triggered as a result of pore pressure increases from the nearby injection. The slip increased the rate along the length of Fault 1 in all cases, with

the magnitude of slip determining how far the significantly affected area extends. Differences in slip timing did not significantly impact the behaviour of the system, nor did the case of a reverse faulting regime. The permeability of the different features was the most important in determining the seismicity rate at later times, with lower permeability restricting access to features farther from the wells and increasing the activity in closer regions. Changes as a result of different fault angles were minor and appear to be more related to differences in fluid diffusion than changes in the slip-produced stresses.

Chapter 4

4   Modelling Strike-Slip Faults

4.1   Introduction

This chapter contains results from simulations of a geomechanical model formulated to describe the behaviour of a strike-slip fault during fluid injection operations. The simulations start with a base case approximating the field data and applying variations to several parameters to examine their effects on the model behaviour. Case Studies 1 and 2 are the base cases to which other variations are applied. Case Study 3 examines the effect of a different injection sequence, while Case Study 4 explores the possibility of fault movement occurring in the opposite direction. Case Studies 5 and 6 look at different angles of the test fault. Case Studies 7,8, 9, and 10 alter the size of the fractured area connecting the fault to the injection sites. Finally, Case Studies 11 and 12 change the permeability of the same fracture zones. Similar to the models in Chapter 3, the study area is within the Duvernay formation in Alberta (Figure 4.1), though the exact wells are different from those used previously in this work. Common features of several simulations are described first, followed by the base case and the variant simulations. Variations were selected based on which properties of the fault system were believed to have substantial impact on the predicted activity. All models are top-down cross-sections and describe the behaviour of a strike-slip fault.
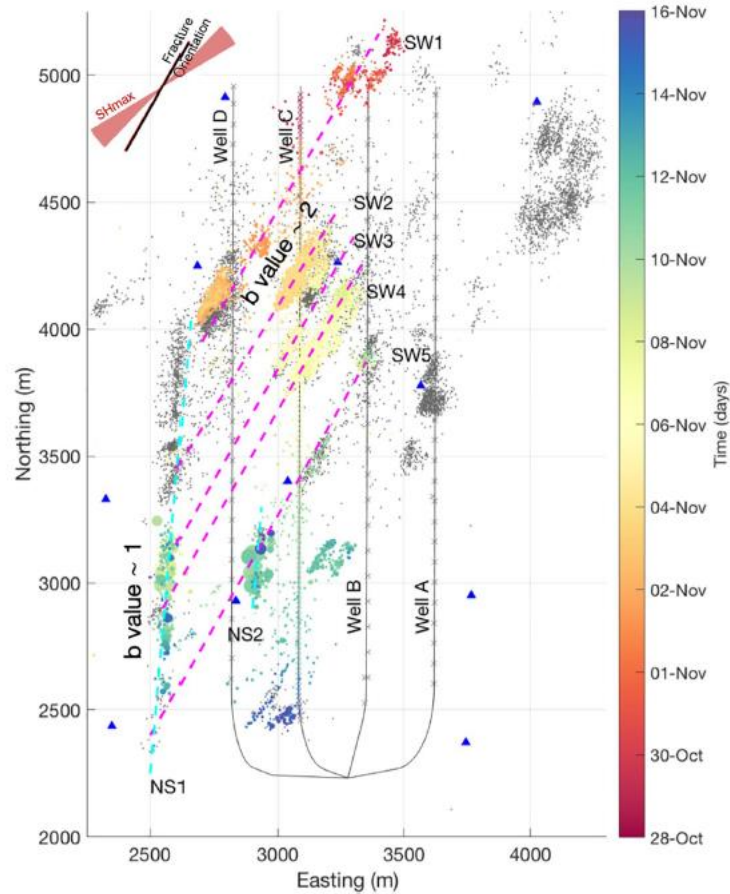
Figure 4.1: Features of the injection system from Igonin et al., (2021). Data was taken during October and November of 2016. Points show recorded events, with coloured points having occurred at the corresponding time. Fracture corridors are noted as magenta lines, while inferred fault locations are shown in cyan. The wells are noted by the grey lines, with each injection point marked by a cross.

4.2 Model Properties

The geomechanical model investigated in this chapter and its variations are based on the field study and modelling done by Igonin et al. (2021). It includes fluid injection emulating those used for the seismic experiments studied in that work. In order to examine the processes involved in injection-induced seismicity, the model simulates both the fluid propagation (using Darcy's Law), and the stresses on the rock formations (using linear poroelasticity). From the simulation data, the rate of seismic activity can be estimated.

4.2.1   Model Geometry

The studied model is a top-down cross-section of four injection wells A-D that connect to a large fault via a permeable fracture zone (Figure 4.2). The simulated geometry only includes the larger NS1 fault from the field data, and not the smaller NS2 or SW1 features that were also inferred to exist. SW1 appears to be another fracture corridor that does not connect to a fault, and NS2 would have significant overlap with the larger fracture zones used in the simulations. The NS1 fault, denoted as Fault 1 within the simulated model, is composed of a rectangular region $10m$ across. This method of simulating the faults is to allow fluid to flow through the fault (see Chapter 1.4.1) The fracture corridors SW2-SW5 are modelled as larger regions with a higher permeability than the surrounding material. The northmost SW2 is not modelled since it does not connect to the fault. Calculations were performed using the finite-element modelling software COMSOL 5.4. Several measurement points have been inserted into the domain, including within and near Fault 1 and a grouping of fixed points arranged in four columns. The finite-element mesh for the strike-slip fault simulations is shown in Figure 4.3, while the parameters used to construct the geometry of the model are described in Table 4.1. Note that the angle present in Table 4.1 is the one used within the software to construct the model and does not correspond to the strike angle. The mesh was constructed using the 'extremely fine' preset settings throughout to ensure the diffusion out of the wells was modelled accurately. The total mesh is composed of 17816 vertices and 35230 triangular elements. The material properties used by the model are described in Table 4.2.

Each of the four boundaries of the model is set to have no flow across it and to be a roller boundary (i.e., the surface can move parallel to the boundary but cannot move inwards or outwards). As well, each boundary is set that no fluid can flow across it.
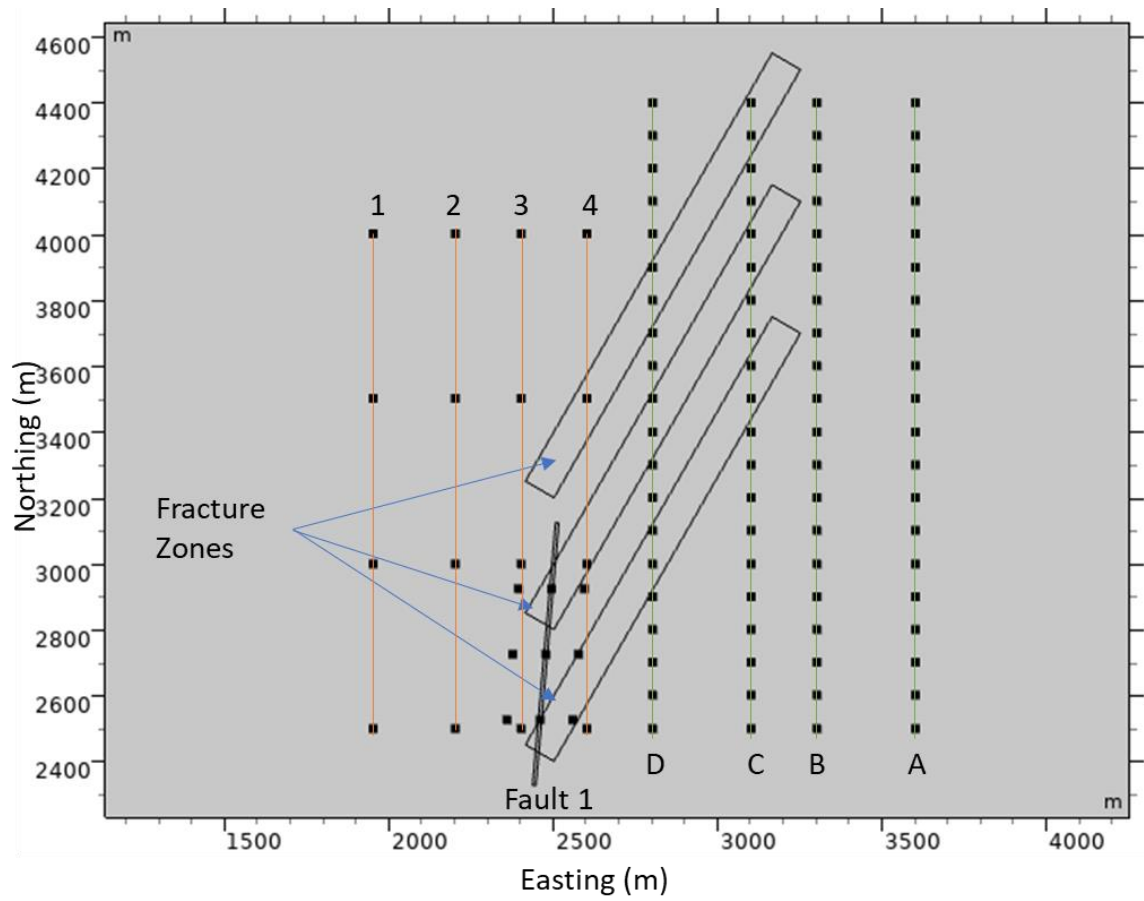
Figure 4.2:Simulated geometry based on the region depicted in Figure 4.1. Wells are labelled with green lines and A-D, with measurement points being labelled with orange lines and 1-4.

Table 4.1: Parameters used to assemble the base case for Model 2. Data chosen to approximate the geometry of Igonin et al., (2021)

Parameter	Value	Parameter	Value	Parameter	Value
Model width in x-direction (m)	4000	Lowest y-coordinate of injection wells (m)	2500	x-coordinate of first fracture zone centre (m)	2500
Model width in y-direction (m)	4000	Spacing between well points (m)	100	y-coordinate of first fracture zone centre (m)	2400
Model offset in x-direction (m)	1000	Well A x-coordinate (m)	3600	Fracture zone spacing (m)	400
Model offset in y-direction (m)	1000	Well B x-coordinate (m)	3300	Total height of model (m)	300
Fault centre x-coordinate (m)	2475	Well C x-coordinate (m)	3100	Spacing from fault to measurement points (m)	100
Fault centre y-coordinate (m)	2725	Well D x-coordinate (m)	2800	x-coordinate for measurement point column 1(m)	1950
Fault length (m)	800	Fracture zone length (m)	1500	x-coordinate for measurement point column 2(m)	2200
Fault thickness (m)	10	Fracture zone width (m)	100	x-coordinate for measurement point column 3(m)	2400
fault angle $(°)$	85	Fracture zone angle $(°)$	60	x-coordinate for measurement point column 4(m)	2600
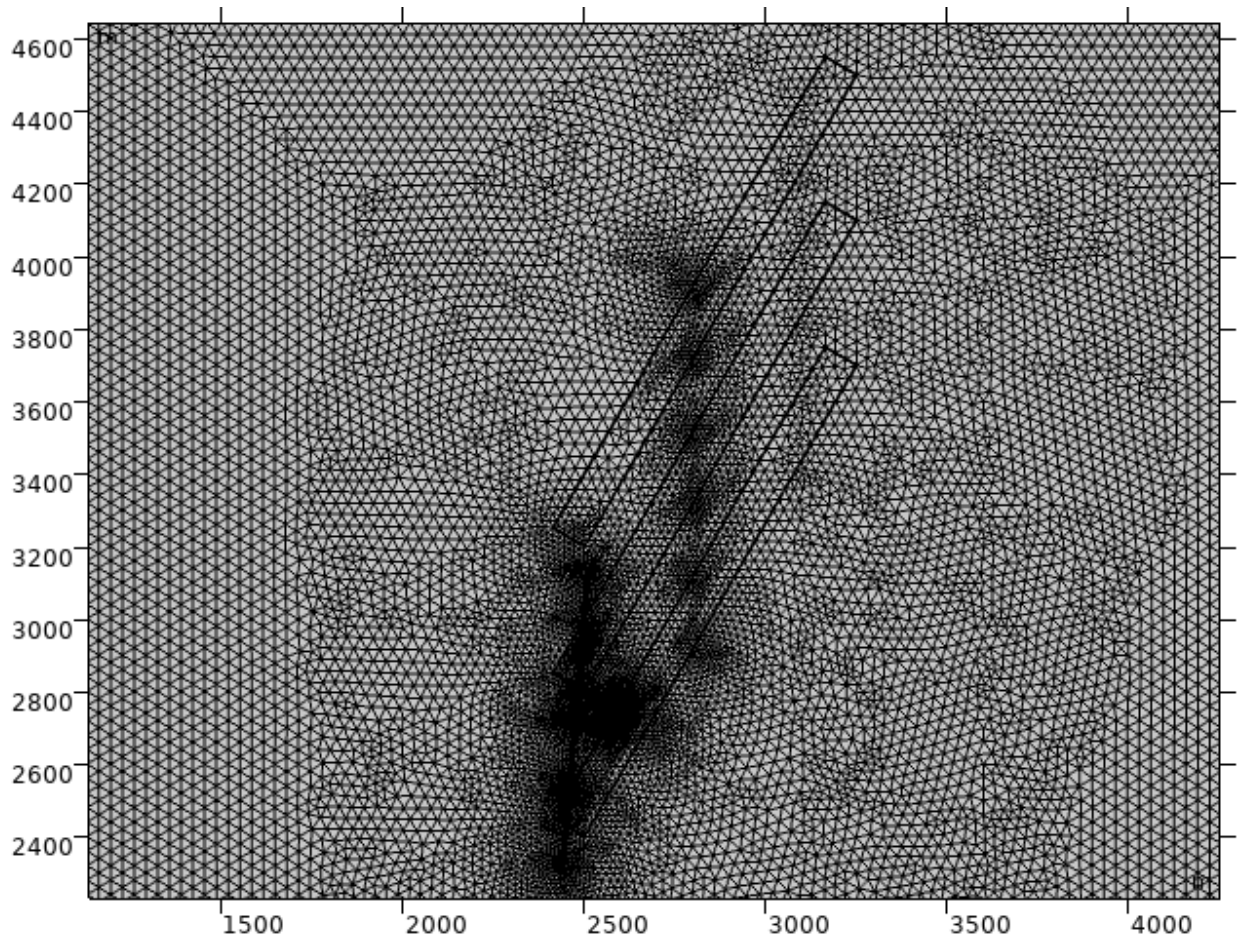
Figure 4.3: Simulation mesh for the model strike-slip fault system. High resolution is used throughout the model.

Table 4.2: Material properties for model 2. [A] Fault data is from (Chang and Segall, 2016), using the data for a conductive fault. [B] Skempton Coefficient is noted as a typical value in (Deng et al., 2016). Other data is determined by the research team based on what are believed to be typical values for the rock type in question.

Parameter	Surrounding shale	Fracture Zones	Fault[A]
Density $\rho \left(\frac{kg}{m^3}\right)$	2 500	2 500	2 500
Young's Modulus E (MPa)	40 000	40 000	14 400
Poisson ratio ν $(-)$	0.25	0.2	0.2
Biot-Willis coefficient α $(-)$	0.4	0.23	0.8
Porosity ϕ $(-)$	0.065	0.15	0.02
Permeability $\kappa (m^2)$	$0.5 * 10^{-14}$	10^{-13}	10^{-13}
Skempton Coefficient[B] B $(-)$	0.75	0.75	0.75

4.2.2 Calculation Parameters

This simulation made use of the fully coupled model described by equations (2.29) and (2.35). The model was run from $t = 0 \ days$ to $t = 150 \ days$, gathering data every $0.1 \ days$. Injection occurred starting at $t = 1 \ day$. First, Well C was injected into, with each noted point on that well receiving an injection rate of $2.2 \frac{m^3}{min}$ for one day. After all the points along Well C have been injected into, Wells A, B, and D were injected concurrently at a rate of $3.2 \frac{m^3}{min}$ split evenly between the three active points, with each row of points again being active for one day each. These figures approximately match the average volume injection rate given in Eaton et al. (2018). The injected fluid is based on the properties from Chang and Segall (2016), with a density of $\rho_f = 1000 \frac{kg}{m^3}$, a viscosity of $\eta = 0.001 \ Pa * s$, and a compressibility of $4 * 10^{-10} \ Pa^{-1}$.

The CFS, calculated using Equation (2.42), was examined to determine when slip should occur on the fault. $0.05\ MPa$ was chosen as the required stress threshold for slip to occur since stresses of that size are capable of triggering earthquakes (King et al., 1994). The slip is modelled as a displacement imposed on each side of the fault. For an $800m$ fault, a 4.0 Magnitude earthquake corresponds to a fault slip of $0.0376m$, with half that value ($0.0188m$) being applied to each side of the fault (Leonard, 2010).

The CFS calculated by the finite-element simulation described above was then used to calculate the activity rate over time. The CFS is recorded in a grid of 63001 data points evenly spaced within a rectangular area from $(1500, 2000)$ to $(4000, 4500)$, every $0.1\ days$. This data was then used to calculate the activity rate using Equation (2.49) and the ode45 function in MATLAB. The other parameters used for solving (2.49) are $t_a = 10^4\ days$ and $A_\sigma = 0.3\ MPa$, based on the results from Chapter 3.3. The solver used an absolute tolerance of 10^{-9}, a relative tolerance of 10^{-8}, and assumes the solution is nonnegative.

4.3   Case Study 1: North-to-South Injection

Following Igonin et al. (2021), injection starts at the northernmost well points and proceeds southwards for all case studies except Case Study 3. The CFS increases significantly a few days after injection begins, corresponding to when injection occurs within an area connected to the fault (see Figure 4.4). A threshold was established for when the fault would slip at a CFS increase of $0.05\ MPa$, which has been noted to be sufficient to trigger earthquakes (King et al., 1994). Despite the steep increase, the stresses applied during the injection of Well C did not meet this threshold. This threshold is surpassed at approximately $t = 34.7\ days$, during the injection into Wells A, B, and D. (Figure 4.4). The western edge of the fault is moved northwards, and the eastern edge of the fault is moved southwards (defining a right-lateral strike-slip fault), in such a way that areas parallel to the fault experience a positive change in CFS (see Figure 4.5). Each side of the fault is subject to a displacement of $0.0188m$, producing a total fault slip of $0.0376m$. This corresponds to a 4.0M earthquake (Leonard, 2010).
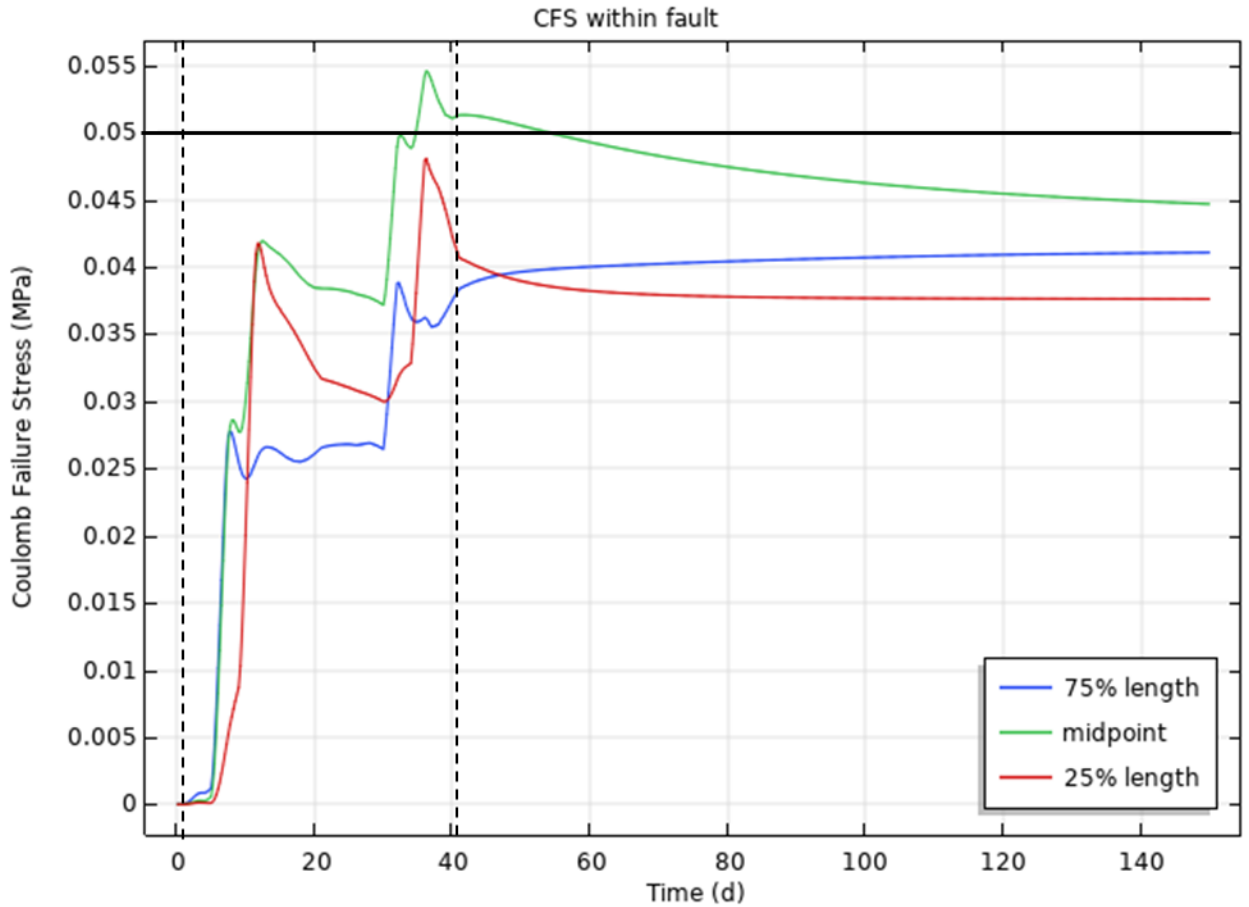
Figure 4.4: Coulomb Failure Stress over time inside the fault. Data was taken at $(2492, 2924)$, $(2475, 2725)$, and $(2458, 2526)$, representing the points 0.75, 0.5, and 0.25 along the length of the fault, respectively, starting from the bottom. The stress threshold of $0.05\ MPa$ (solid black line) is crossed at approximately $t = 34.7\ days$. The injection period is denoted by the dashed lines.

A
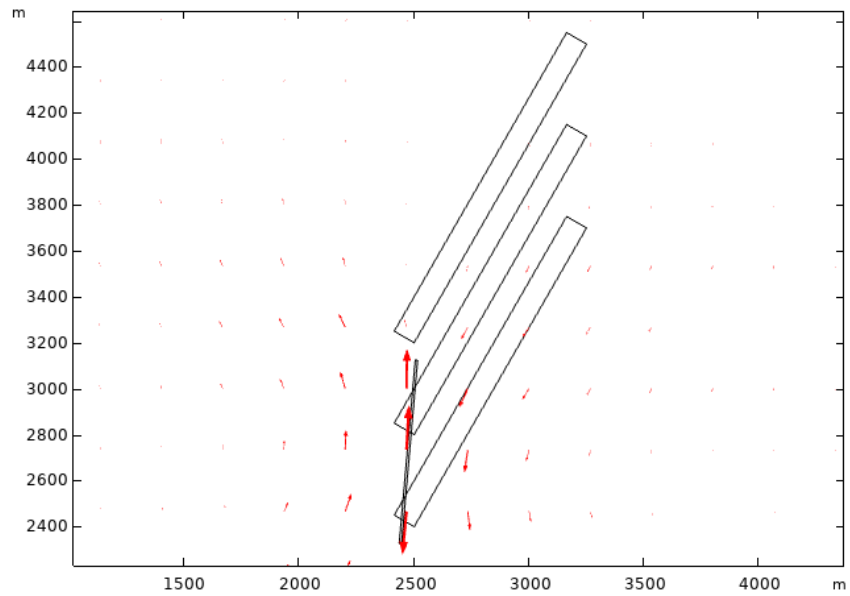
B
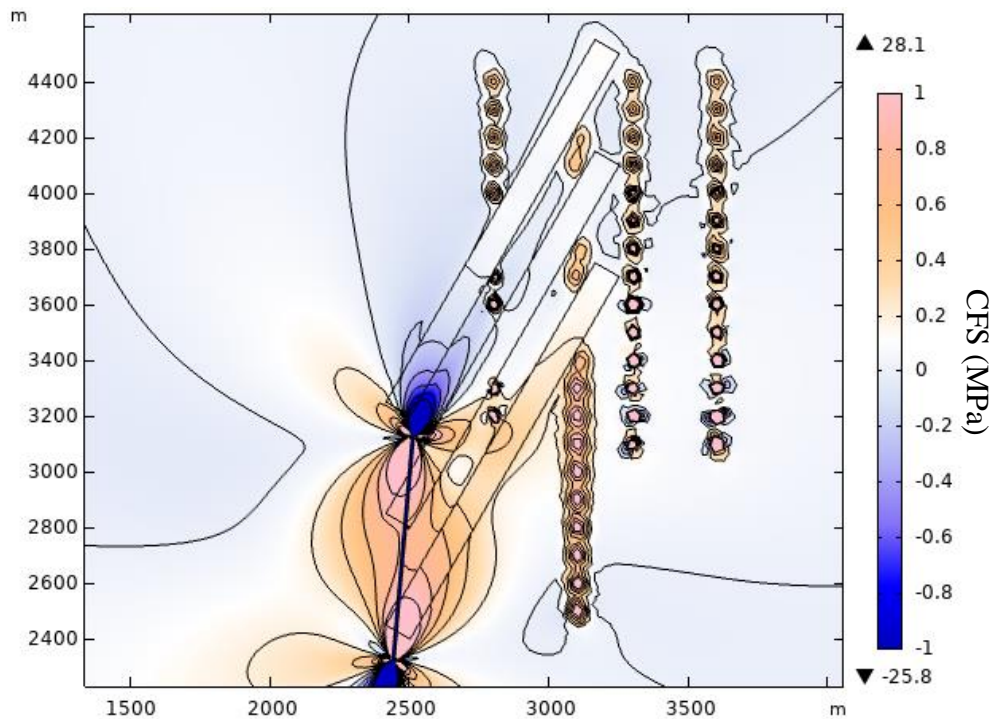
Figure 4.5: (A) Displacement and (B) resulting Coulomb failure stress of a $0.0376m$ slip on the fault. Snapshot was taken at $t = 35\ days$. Areas directly East and West of the fault have increased CFS and would be more likely to produce activities. The calculated CFS includes the contribution from the fluid movement.

Outside of the permeable fracture zones and fault, the pore pressure takes a very long time to diffuse away from the injection wells, with the location of the wells still being visible from the locations of high pressure after injection finishes (Figure 4.6).
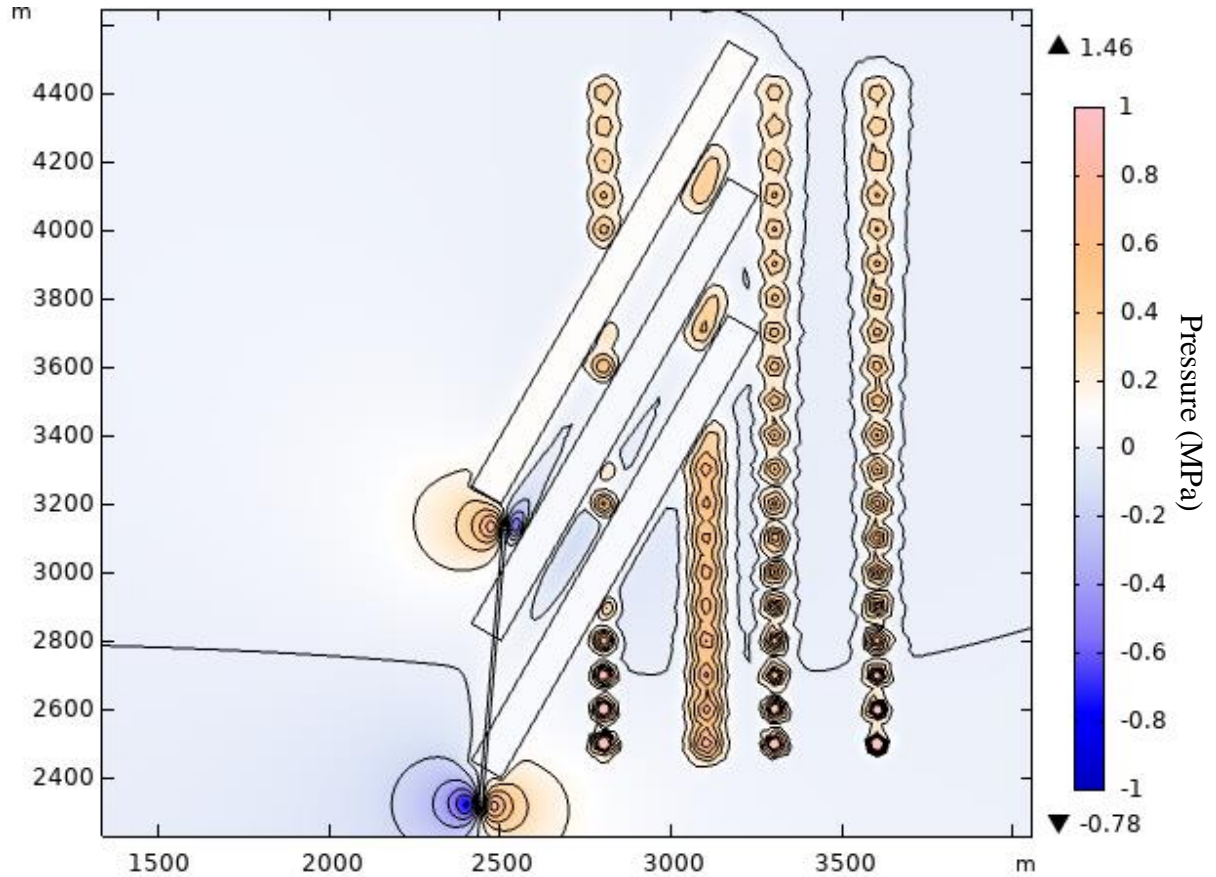
Figure 4.6: Pore pressure at $t = 50\ days$, after injection concludes. Isolated wells are still discernable as vertical areas of high pressure, particularly in the case of Well C s as a result of higher individual injection at that location.

4.4   Case Study 2: Second Fault

In order to examine the ability of slip on one fault to induce slip on other faults, a second fault needs to be inserted into the model. For this case, a copy of the main fault is placed $100m$ to the west of the original (Figure 4.7), with the same angle and y-position of the centre. The distance was chosen to be close enough that stresses from the main fault slipping would be noticed at the location but far enough that it was unlikely to interfere with the fluid propagation to the main fault. Similarly, a large fault placed to the

east of the main fault would affect the fluid movement through the fracture zones. Injection and slip proceed as in Case Study 1. This second fault is included in later case studies, and the addition increases the mesh size to 19239 vertices and 38076 triangular elements.
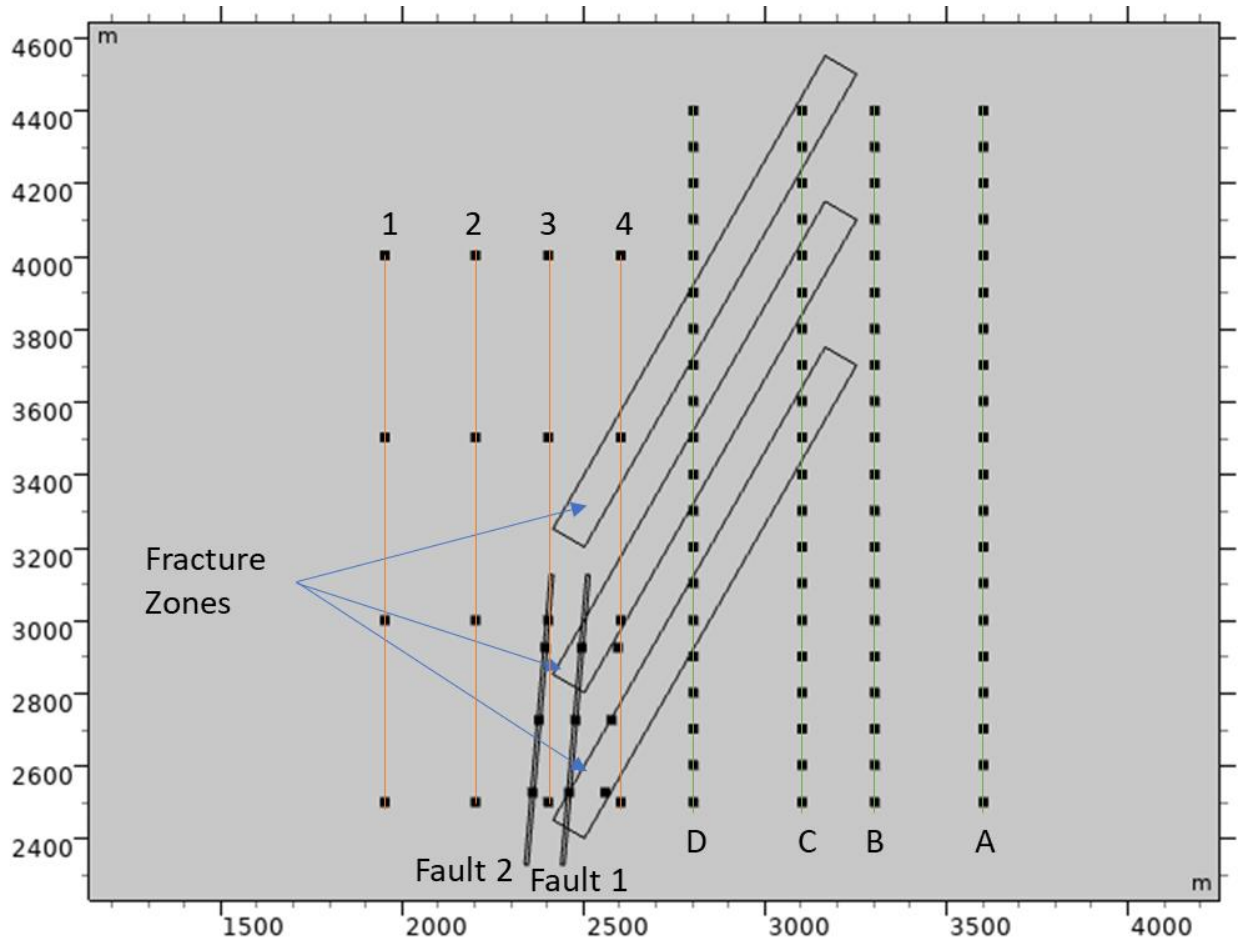
Figure 4.7: Model geometry including a secondary fault parallel to the first. The secondary fault does not have any permeable connections to the injection wells, fracture zones, or the main fault.

This secondary fault is not hydraulically connected to the main fault or the fracture zones. As a result, it has minimal change in pore pressure. The only increase in seismic activity noted occurs when the main fault moves (Figure 4.8). The poroelastic stresses on the second fault produce a small reduction in the CFS compared to this

increase from the slip. The test fault is not significantly stimulated and does not have a substantial activity rate (Figure 4.9).
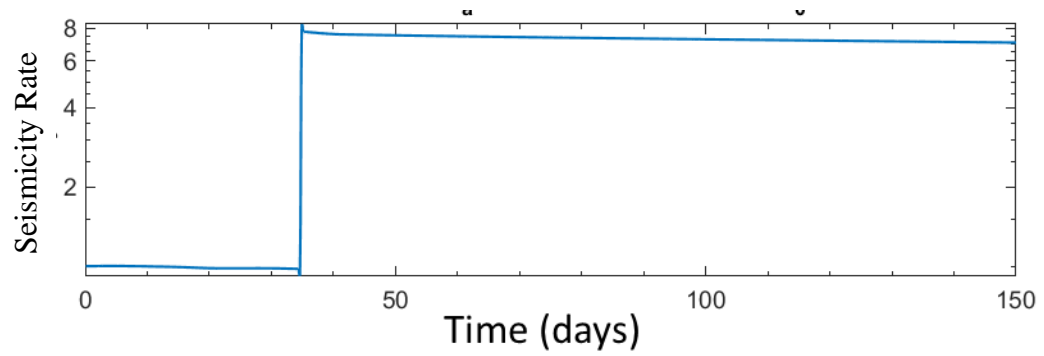
Figure 4.8: Activity within the midpoint of Fault 2. The activity is increased at $t = 34.7\ days$ when the fault slip occurs but is otherwise decreasing throughout as a result of the poroelastic stressing from the injection.
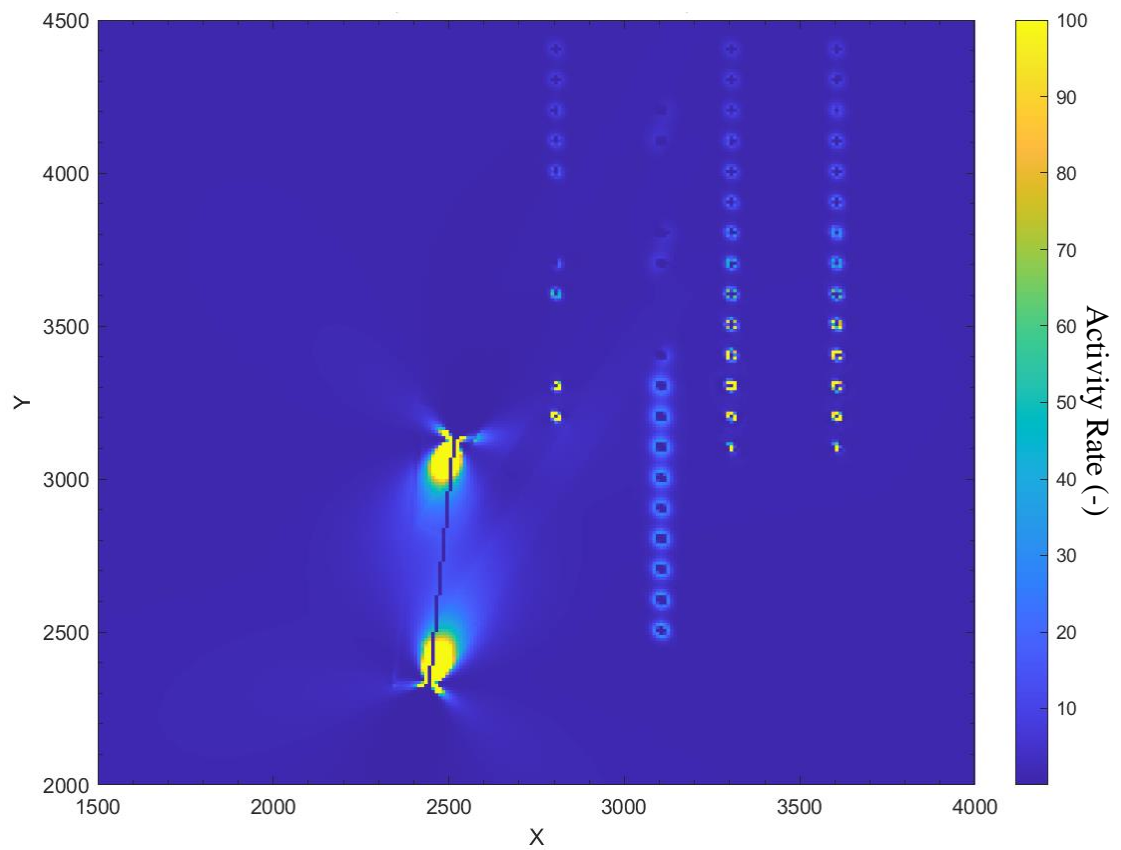
Figure 4.9: Calculated activity rate for Case Study 2 at $t = 35\ days$. Sites of high activity are shown with yellower pixels, with the scale given on the right. Since the secondary fault is not stimulated compared to the surrounding rock, it does not appear distinct. Meanwhile, the main fault and any isolated wells are clearly visible by virtue of having different activity from their surroundings.

4.5   Case Study 3: South-to-North Injection

To better examine the poroelastic stresses before the fluid reaches the fracture zones and proceeds to the fault, the injection was switched to proceed starting from the south instead of the north. This allows the lower points to complete their injection before the fault is in permeable contact with a fluid source. The unconnected wells produce compressive stresses in the direction of the fault (Figure 4.10). This leads to the fault experiencing a negative CFS change in the time before the injection reaches the fracture zones at approximately $t = 10\ days$ (Figure 4.11). As a result, the main fault reaches the slip threshold at approximately $t = 31.5$ days, when the movement is applied to the system. Within Fault 2, increases in activity rate are still caused by the slip, but the drop in CFS as a result of poroelastic stressing from the wells is more prominent in times before the slip occurs (Figure 4.12).
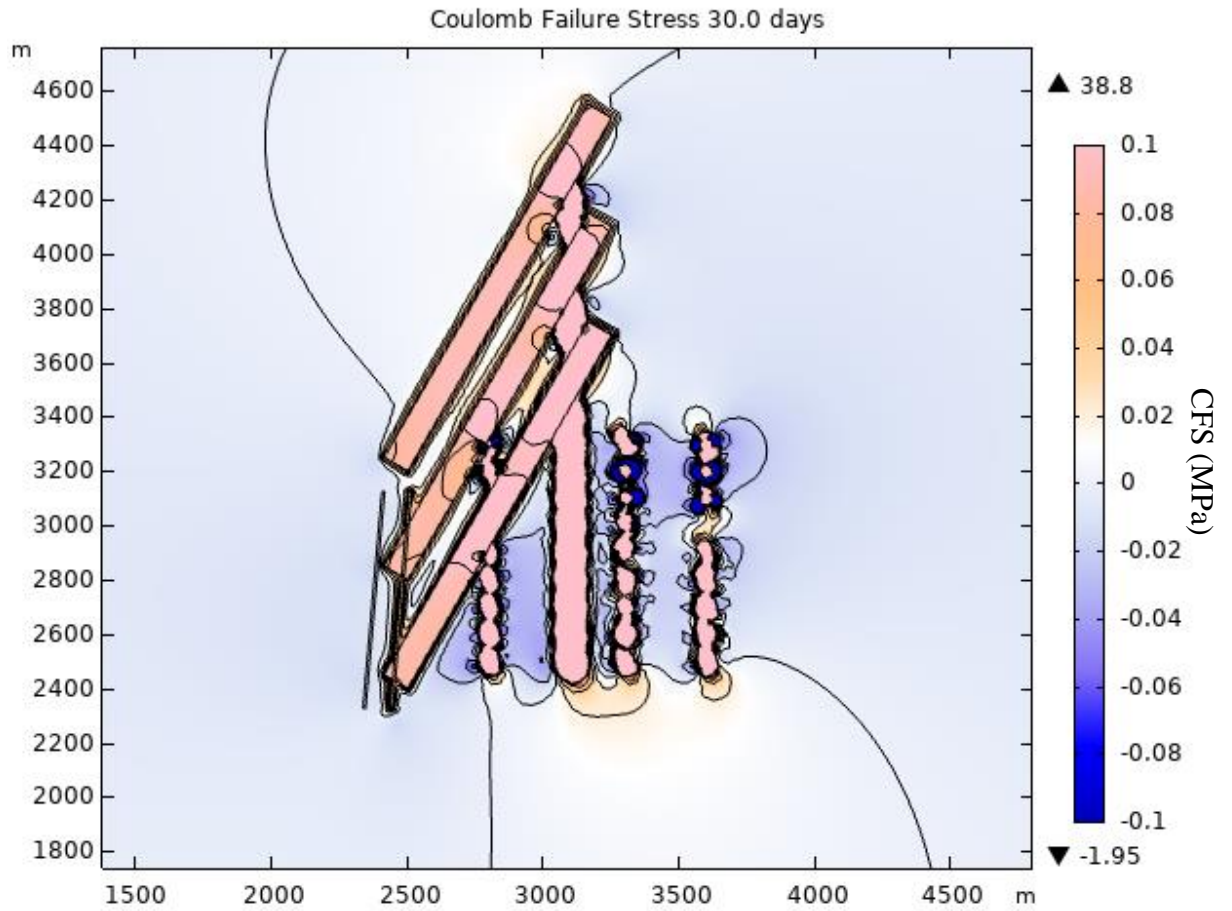
Figure 4.10: system CFS at $t = 30\ days$. The faults are in a region of negative stress, inhibiting slip. The data range has been reduced so that the decreases in stress from the injection wells is visible.
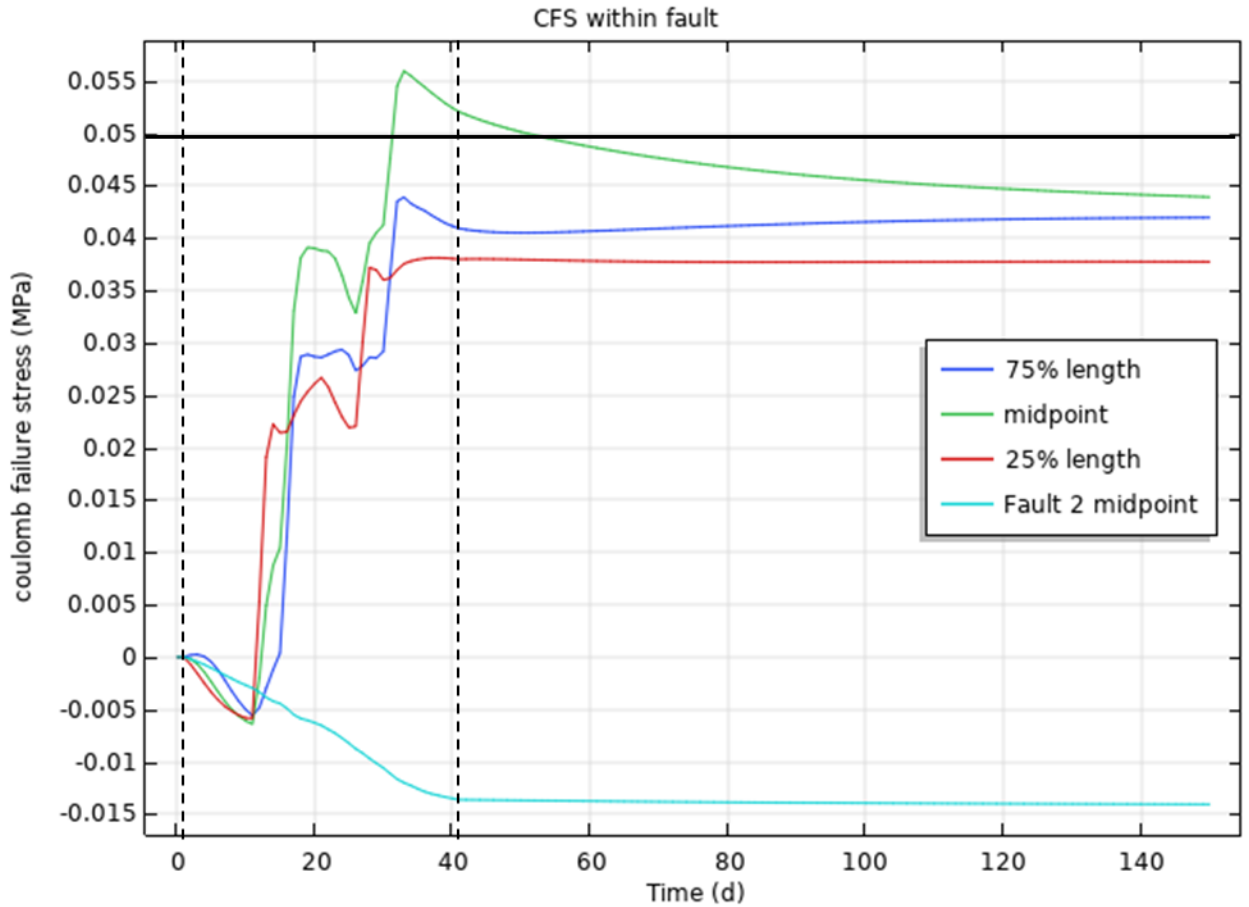
Figure 4.11: CFS within the main fault for injection proceeding from the south upwards to the north. No slip is applied to the fault in this simulation. The injection period is denoted by the dashed lines The slip threshold of $0.05\ MPa$, shown by the solid black line, was passed at approximately $t = 31.3\ days$.
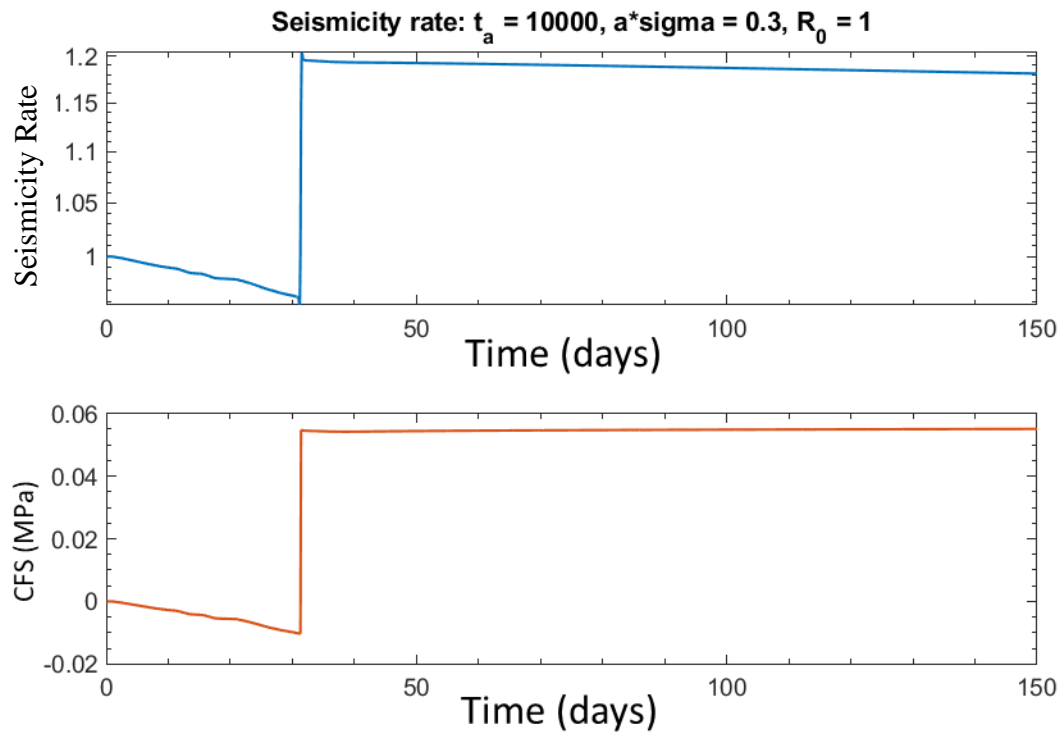
Figure 4.12: Activity and CFS over time for Case Study 3, taken at the midpoint of Fault 2. Except for an upwards shift at the time of the fault slip, CFS and activity continue trending downwards.

The calculated activity for the simulation after the slip occurs near the main fault is shown in Figure 4.13B, along with the accompanying CFS at that time (Figure 4.13A). Gaps in the areas of high activity match the locations of isolated wells, particularly along Well C which was injected into earliest. Within the fracture zones, this is masked by the relatively low initial rate from the fluid diffusing outwards. This effect is the most pronounced for Case Study 3, as the isolated wells are injected into earlier.

A
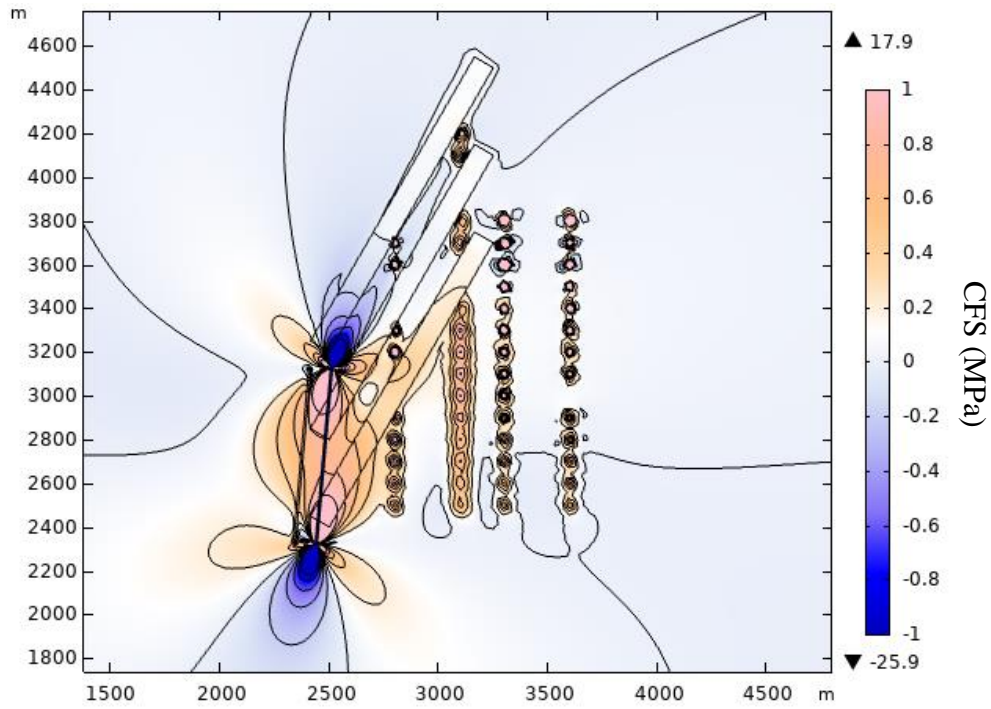
B
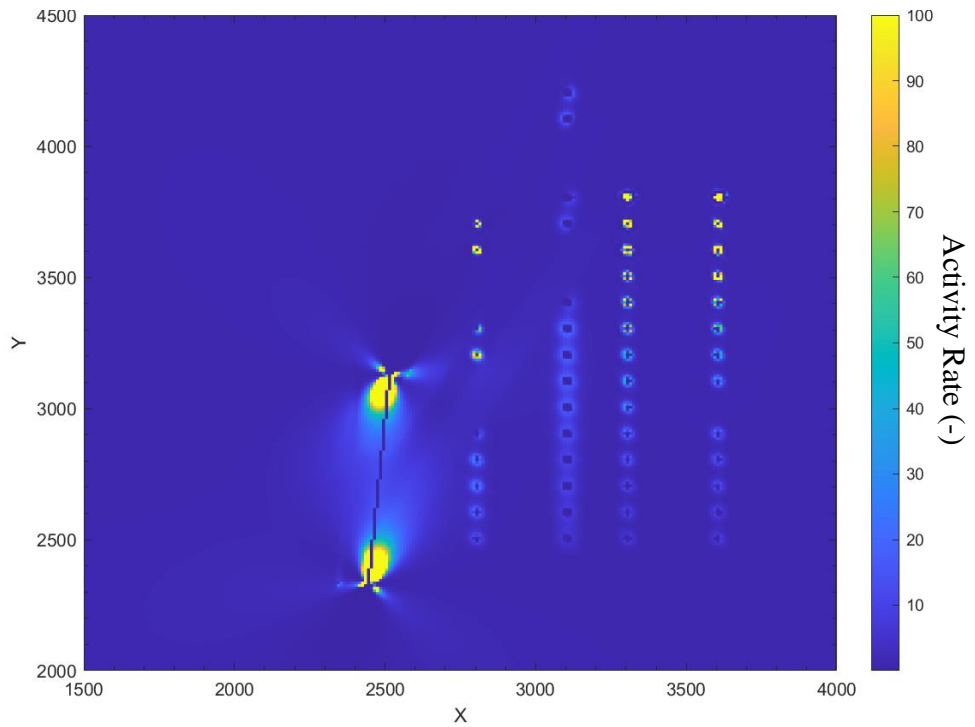
Figure 4.13: (A) Coulomb Failure Stress and (B) calculated activity rate for Case Study 3 at $t = 35\ days$.

4.6   Case Study 4: Inverted Slip Movement

For this simulation, the movement on Fault 1 is inverted, with the west side moving southward and the east side moving northward (Figure 4.14). This forms a left-lateral fault slip. The slip magnitude and timing are unchanged from Case Study 1, as is the injection sequence.
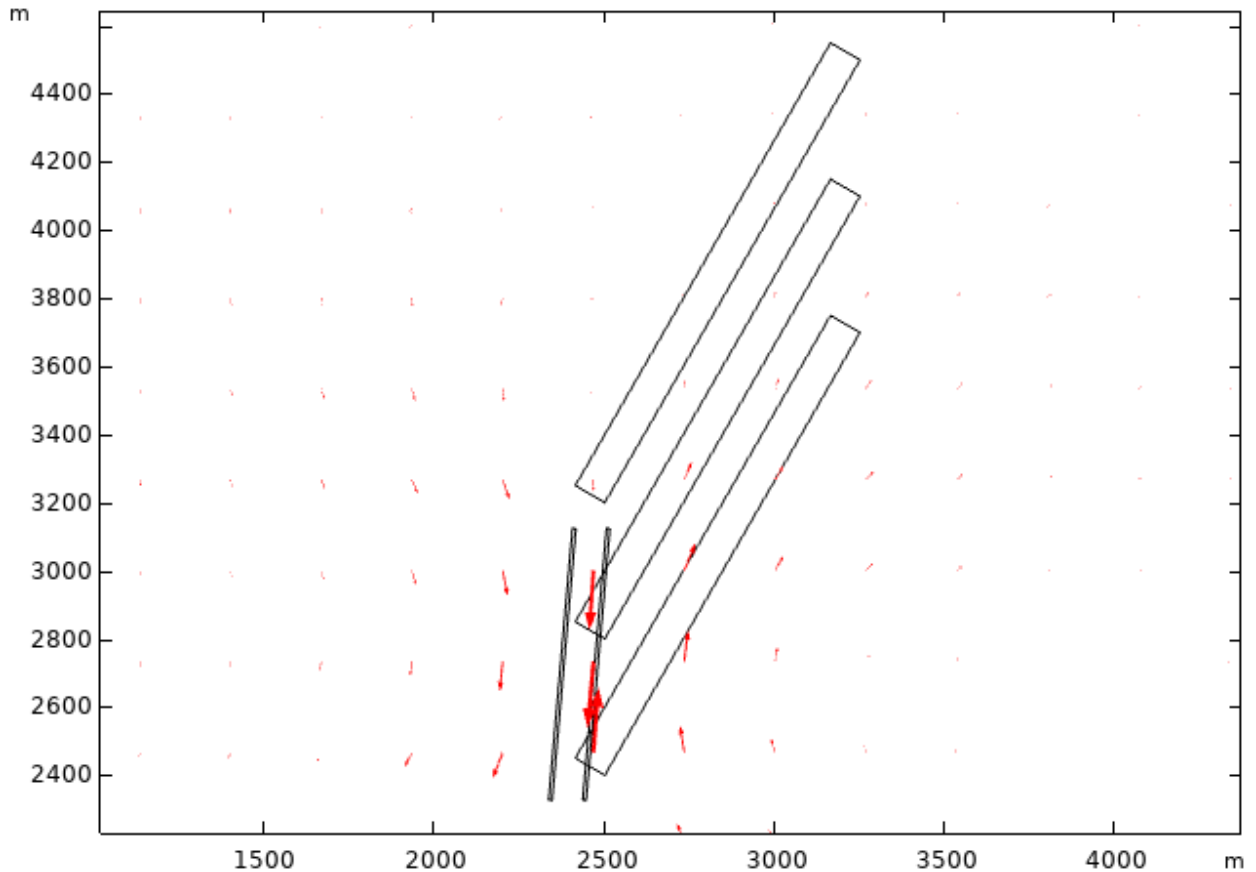
Figure 4.14: Displacement after a $0.0376m$ fault slip for Case Study 4.

When examining the possibility of failure in the same direction as Fault 1, the CFS is very similar to that of Case Study 2 (Figure 4.15). However, when examining the potential for right-lateral slip also looked at for the other case studies, this movement instead reduces the CFS in the region of Fault 2 (Figure 4.16).
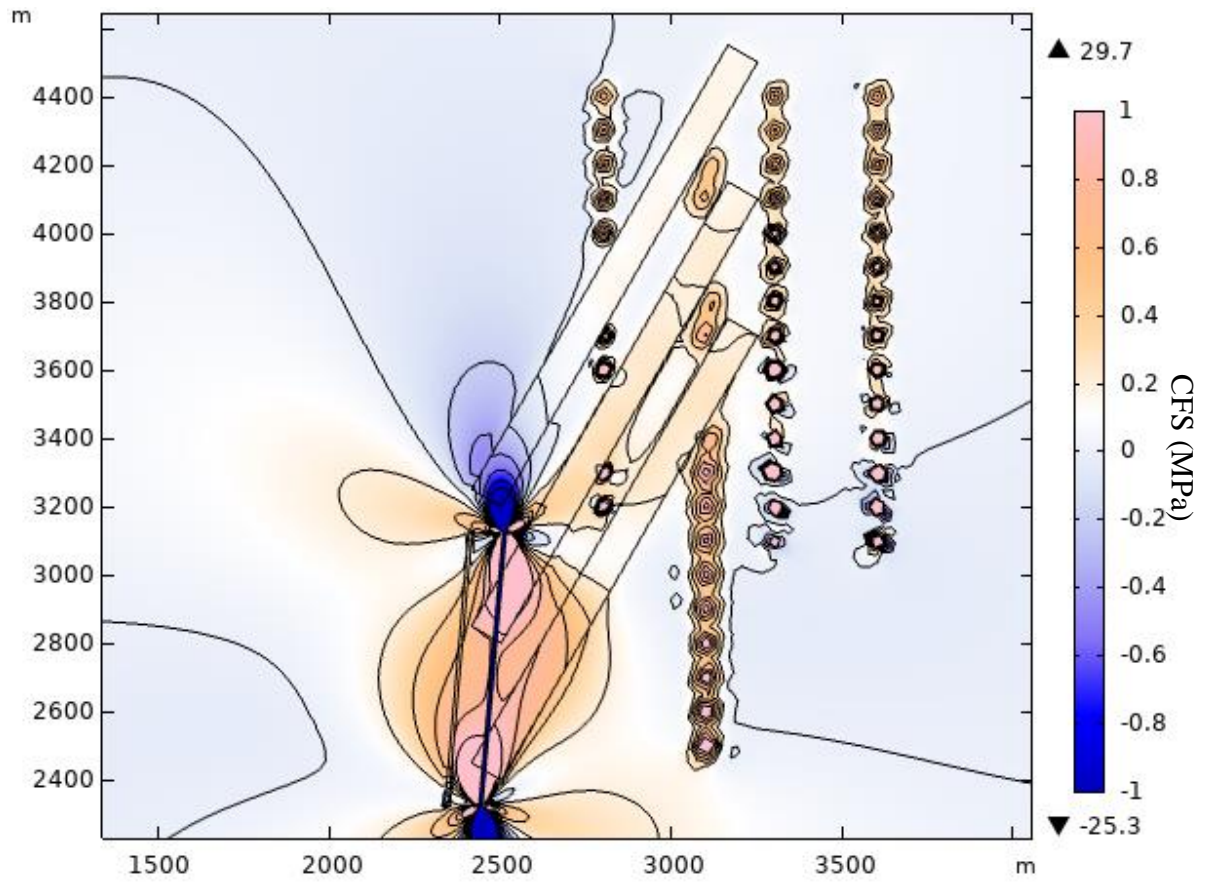
Figure 4.15: CFS assuming right-lateral failure for Case Study 4 at $t = 35\ days$.
The stress pattern is similar to that seen in Case Study 2.
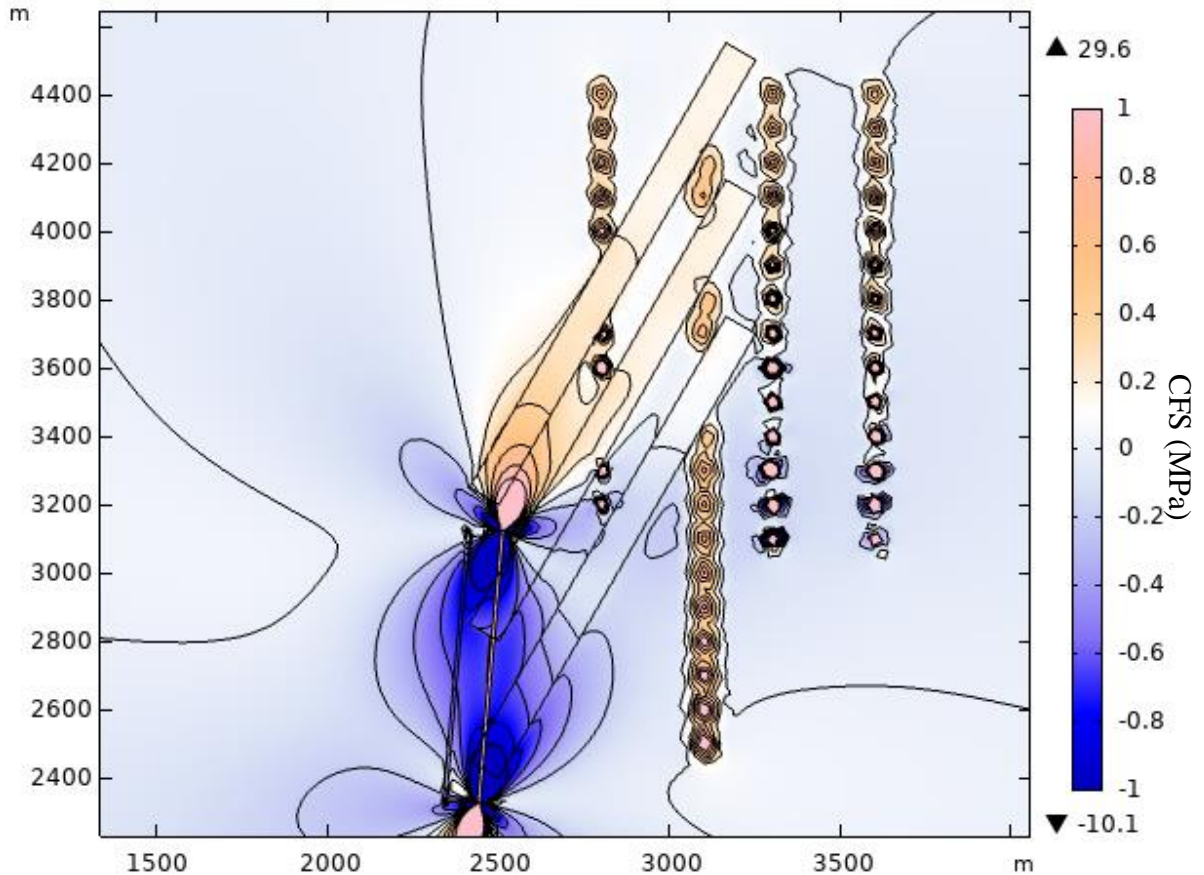
Figure 4.16: Coulomb Failure Stress Assuming left-lateral failure for Case Study 4. Snapshot was taken at $t = 35\ days$, shortly after the fault slip occurred. Solid stresses from the slip result in a decrease along the length of the fault, while areas stimulated by high pore pressure still have positive CFS.

4.7   Case Studies 5 and 6: Angle of Fault 2

For these cases, the angle of Fault 2 was changed so that it is no longer parallel to the main fault. For these cases, the CFS is calculated based on the direction of Fault 2 rather than Fault 1, though slip on the main fault proceeds as normal. For Case Study 5, the test fault is set to 70°, while for Case Study 6 it is set to 100°. In order to prevent the two faults from overlapping with one another, Fault 2 was also moved $25m$ more westward. The model geometry for these case studies is shown in Figure 4.17. Injection and the timing of the slip on Fault 1 proceed as in Case Study 1.

A
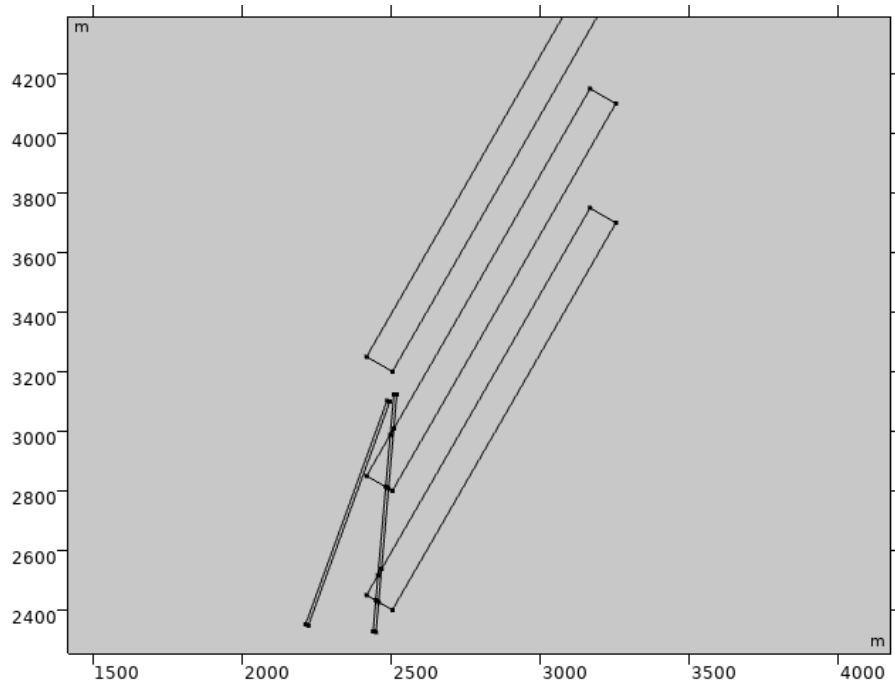
B
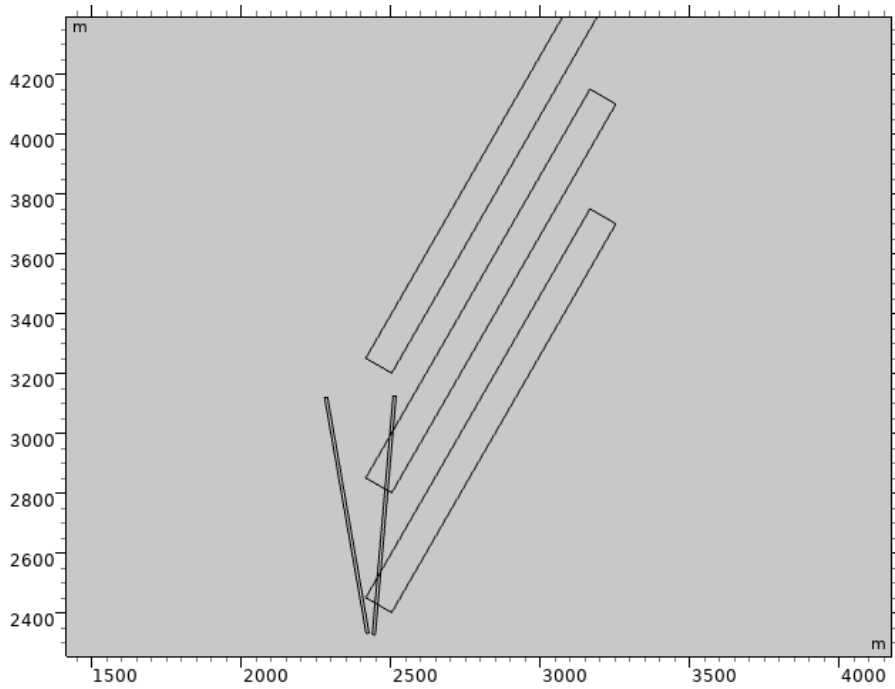
Figure 4.17: Simulation geometry for (A) Case Study 5 and (B) Case Study 6.

The calculated CFS can be compared to Case Study 2 (Figure 4.18). The contributions from pore pressure are the same regardless of the orientation and account for most of the increases near the wells and fracture zones. However, the solid stresses do vary based on orientation. Despite being close to the main fault at the endpoints, the pore pressure within Fault 1 takes a long time to diffuse into Fault 2 (Figure 4.19).

A
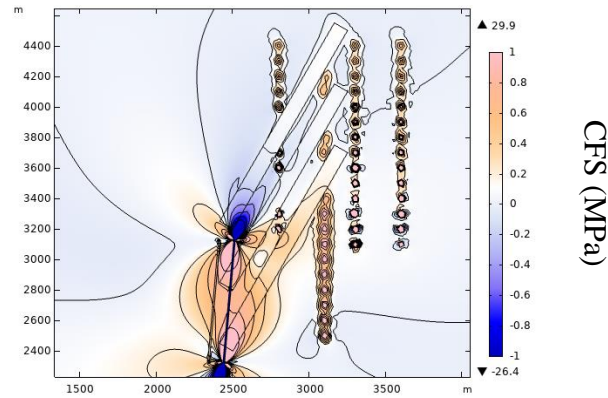
B
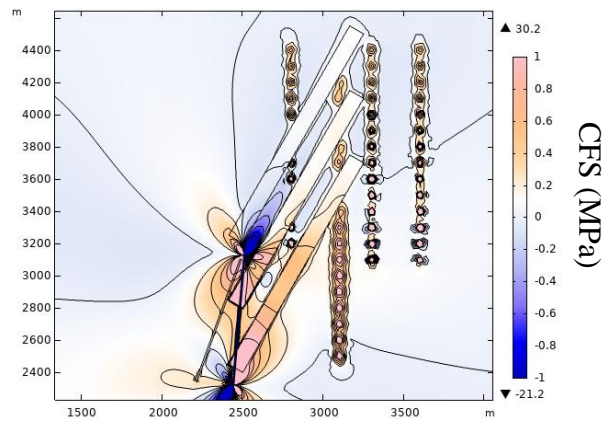
C
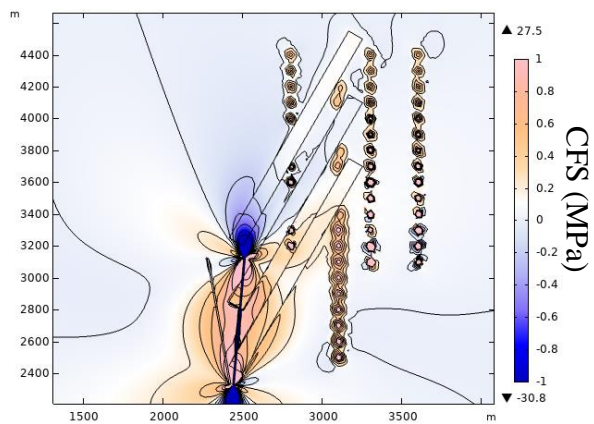
Figure 4.18: Coulomb Failure stress after fault slip for (A) Case Study 2, (B) Case Study 5 and (C) Case Study 6. Stress changes from the fault slip are more favourable for Case Study 6, while poroelastic stresses from injection are more positive in Case Study 5.

A
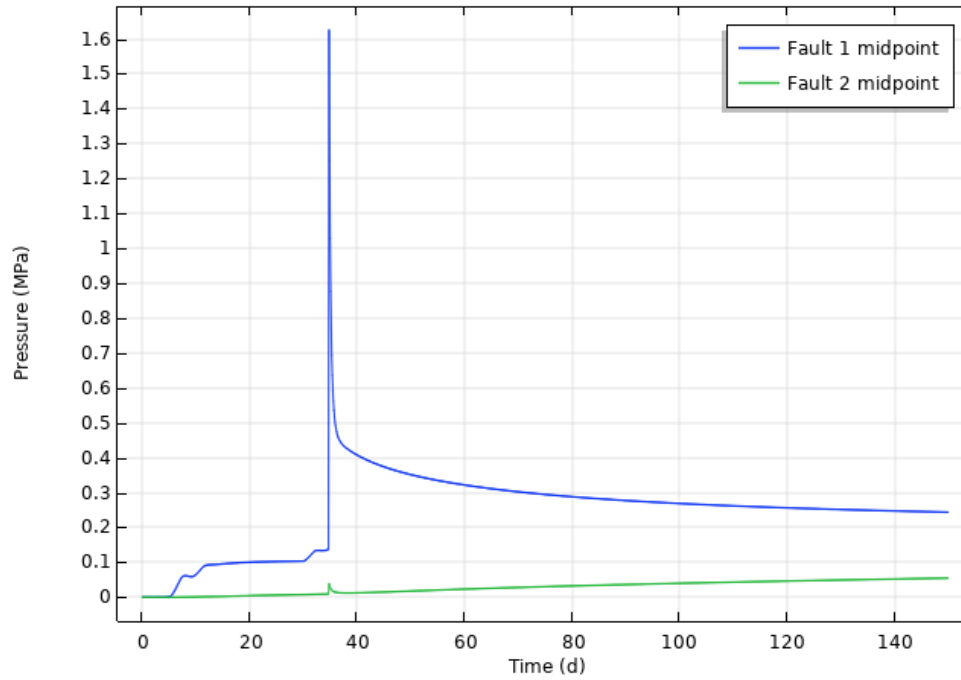
B
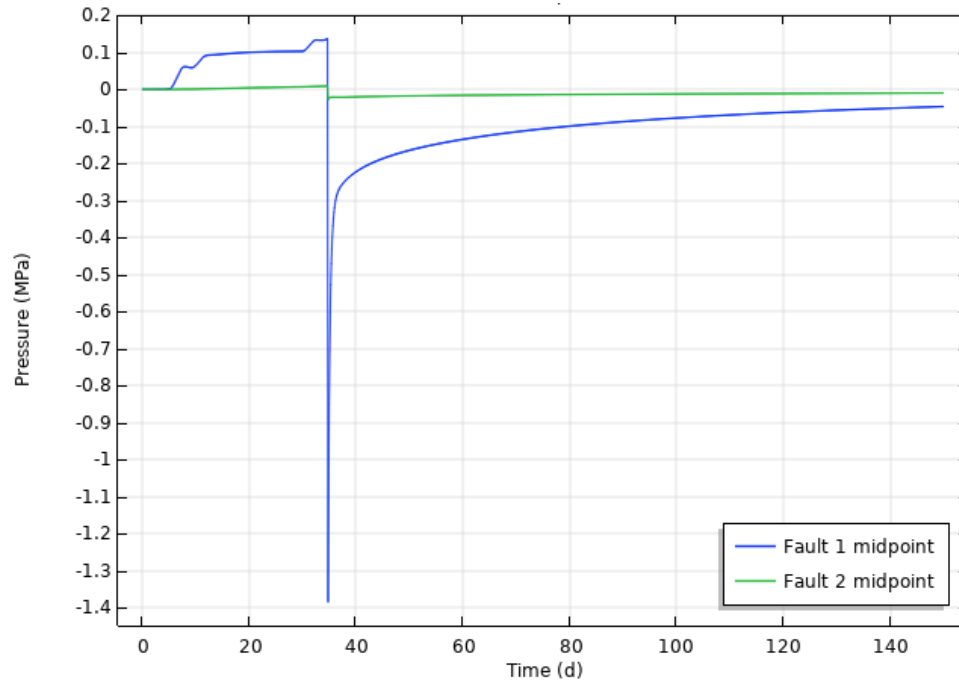
Figure 4.19: Pore pressure over time for the midpoints of each fault in (A) Case Study 5 and (B) Case Study 6. Despite the proximity of the two faults, pressure does not equalize between them before fault slip occurs.

4.8   Case Studies 7, 8, 9 and 10: Fracture Zone Size

Since the slip appears to be triggered by pore pressure diffusion through permeable fracture zones, simulations were performed with smaller fracture zones in order to examine when and if the fault would still slip. For Case Study 7, the fracture zones are halved in width to $50m$. It failed to meet the $0.05\ MPa$ threshold for slip during the simulation period (Figure 4.20). Case Study 8 was then run with an intermediate value of $75m$ for fracture zone width. It reached a peak CFS within the fault of $0.046\ MPa$, still falling short of the threshold (Figure 4.21). Both case studies were rejected from further examination.
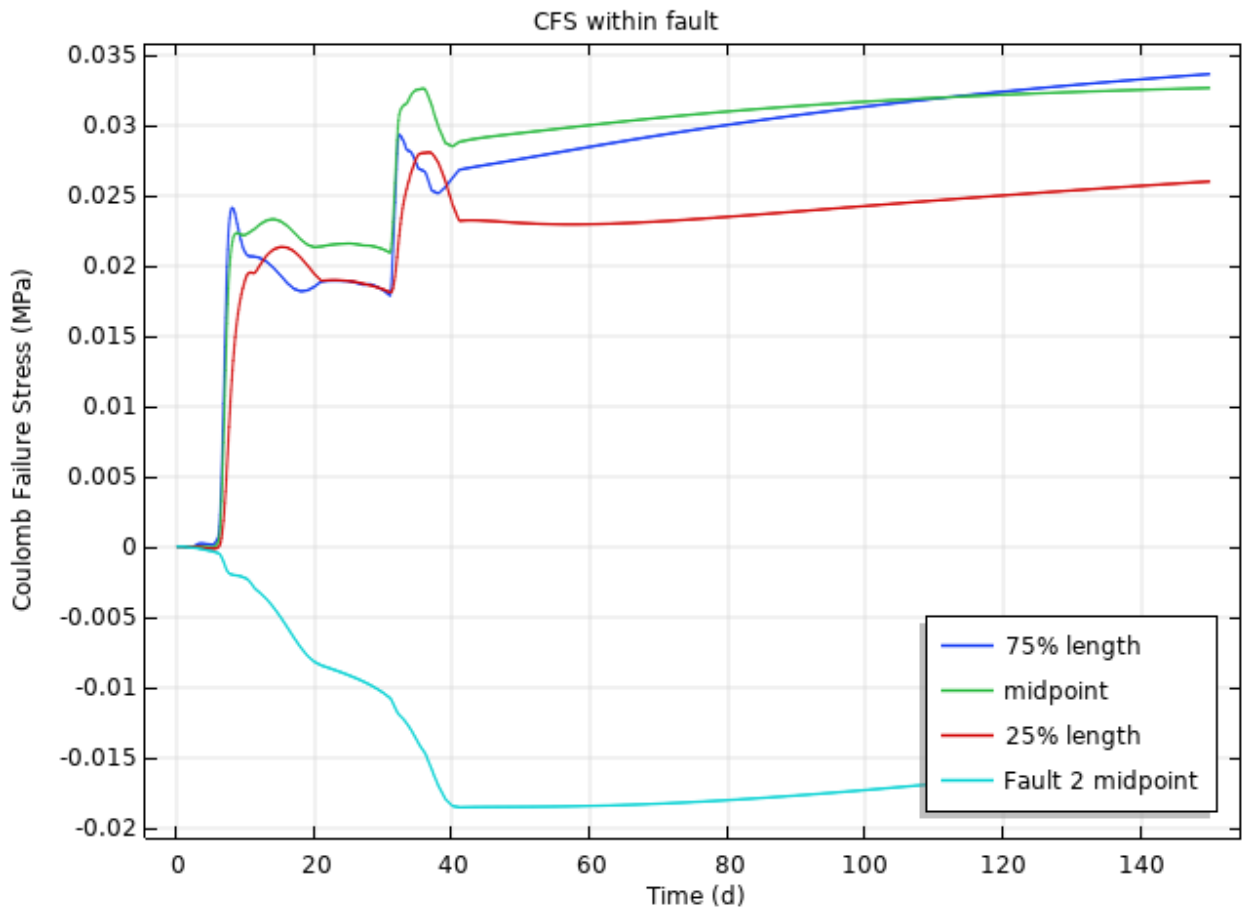
Figure 4.20: Coulomb Failure stress over time within the faults for Case Study 7. The $0.05\ MPa$ threshold is not met.
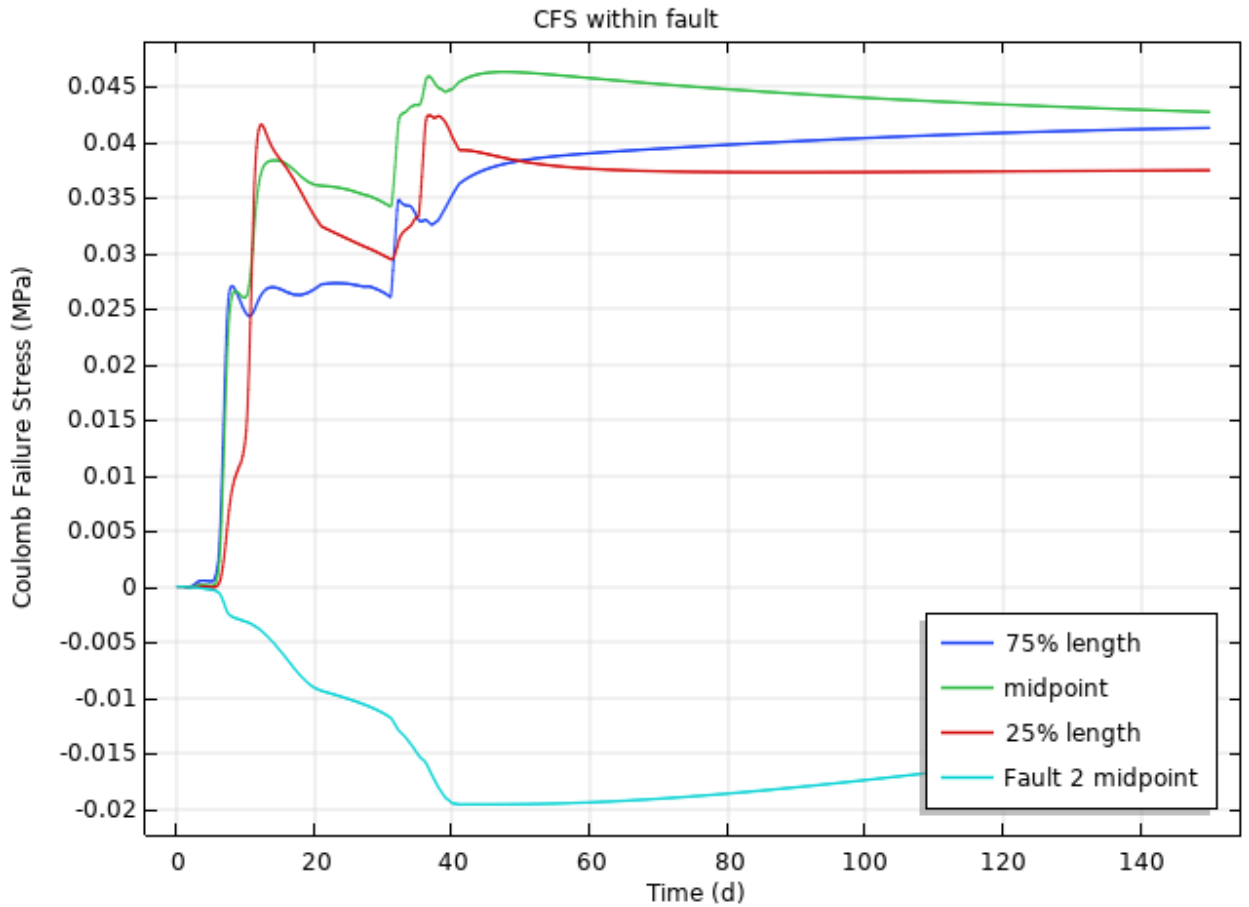
Figure 4.21: Coulomb failure stress within the fault for Case Study 8. The slip threshold is closer to being met than in Case Study 7, but is still not reached

For Case Study 9, the width of the fracture zones was increased to $150m$. The fracture zones were also cut off by Fault 1 to prevent fluid transfer into Fault 2 (Figure 4.22). The increased width led to the stress threshold being met earlier, at $t = 31.8\ days$ (Figure 4.23). Compared to Case Study 2, the activity rate after both models have slipped is similar (Figure 4.9 and Figure 4.24)
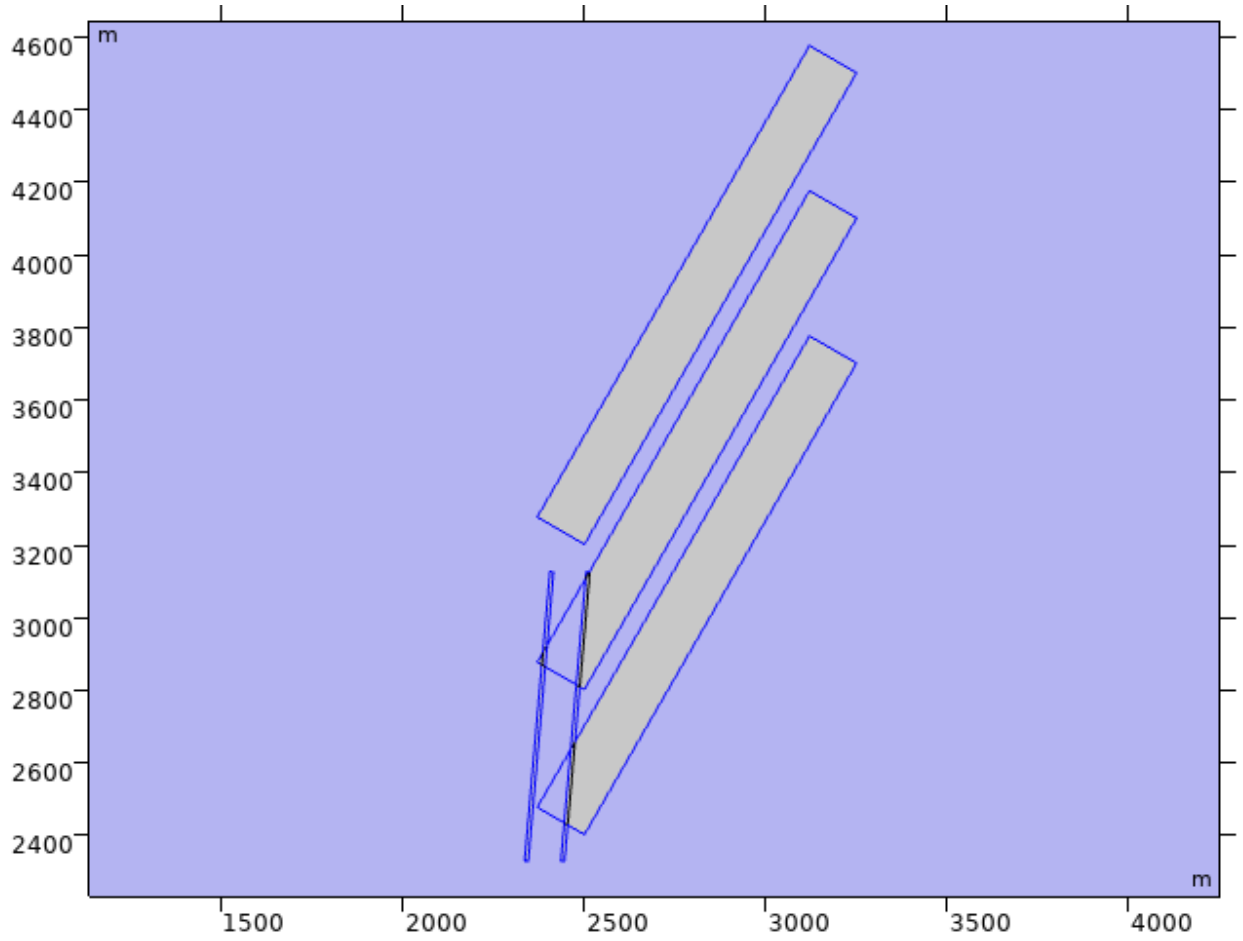
Figure 4.22: Model geometry for Case Study 9. Regions highlighted in blue use the properties for the main rock.
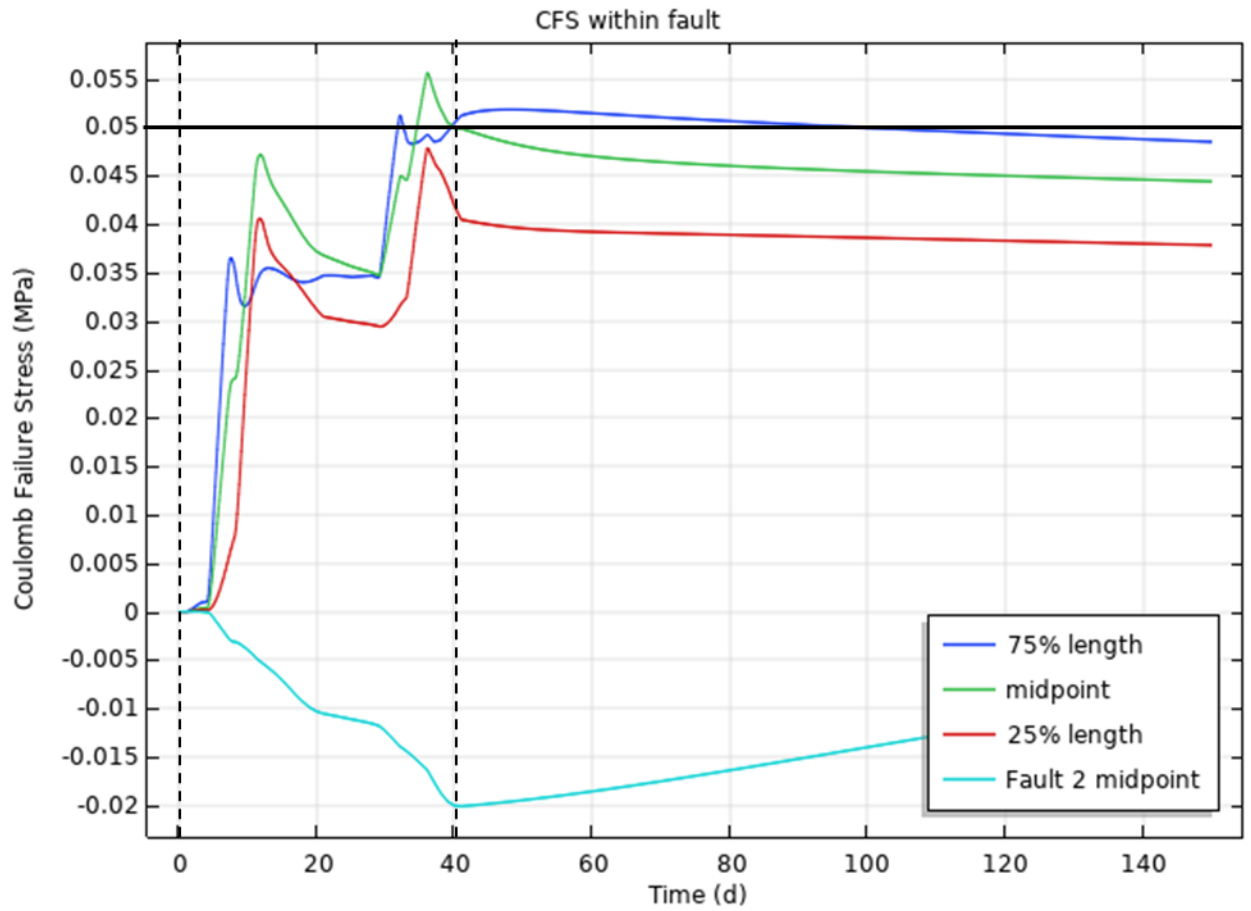
Figure 4.23: CFS over time within fault for Case Study 9. The slip threshold (solid black line) is met at $t = 31.8\ days$.
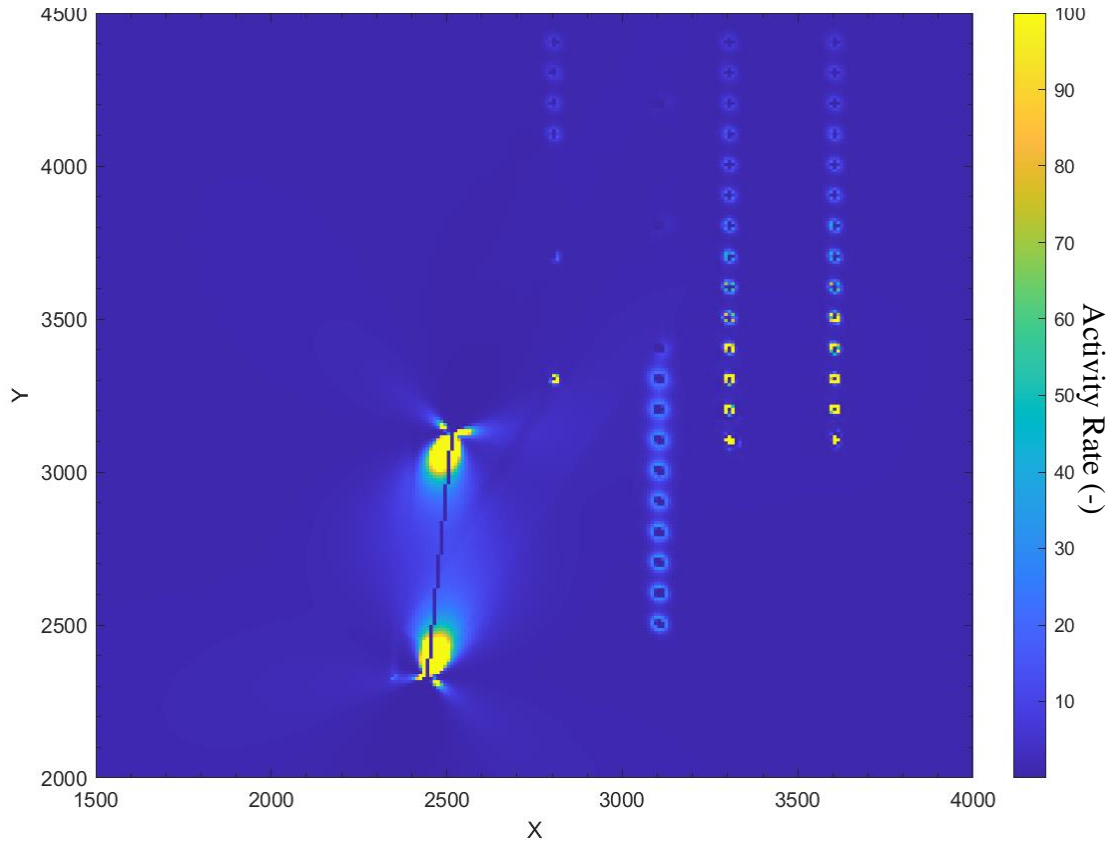
Figure 4.24: Activity rate at $t = 35\ days$ for Case study 9. Rate as a result of fault slip has not noticeably changed.

Finally, in Case Study 10, a simulation is performed without the presence of the fracture zones. Since the poroelastic stresses from injection inhibit slip in the region of the fault, the fault does not meet the stress threshold at any time during the simulation and no slip occurs (Figure 4.25).
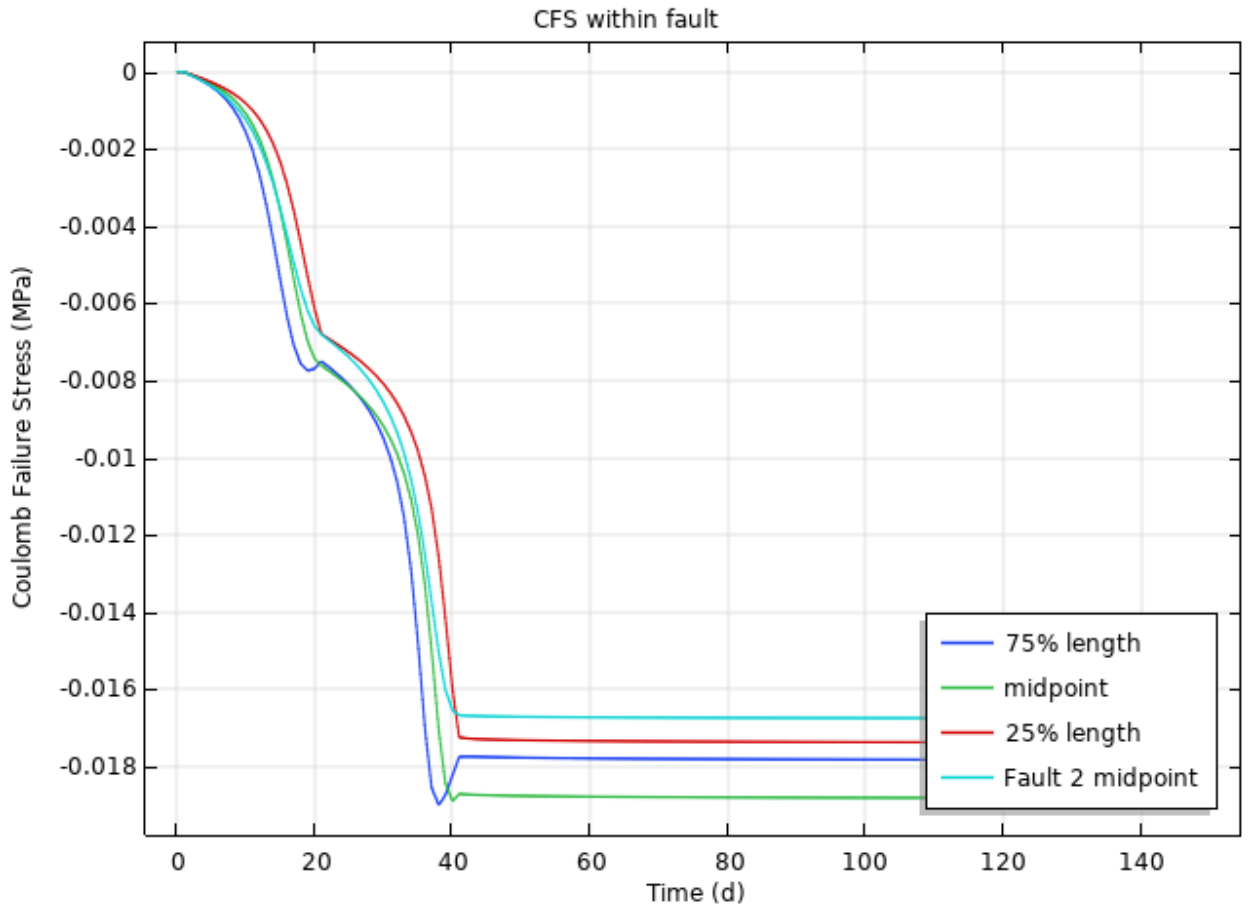
Figure 4.25: CFS within the faults for Case Study 9. The CFS is not positive at any point in the simulation, so no fault slip occurs.

4.9   Case Studies 11 and 12: Fracture Zone Permeability

For these simulations, the permeability of the fracture zone was altered to examine its impact. For Case Study 11, it was increased by an order of magnitude to $10^{-12} \, m^2$, while it was decreased by an order of magnitude to 10^{-14} for Case Study 12. Increased permeability did not significantly change the timing of when the CFS reaches the threshold for slip (Figure 4.26), and the threshold is not met during Case Study 12 (Figure 4.27). Both cases were deemed unsuitable for further examination.
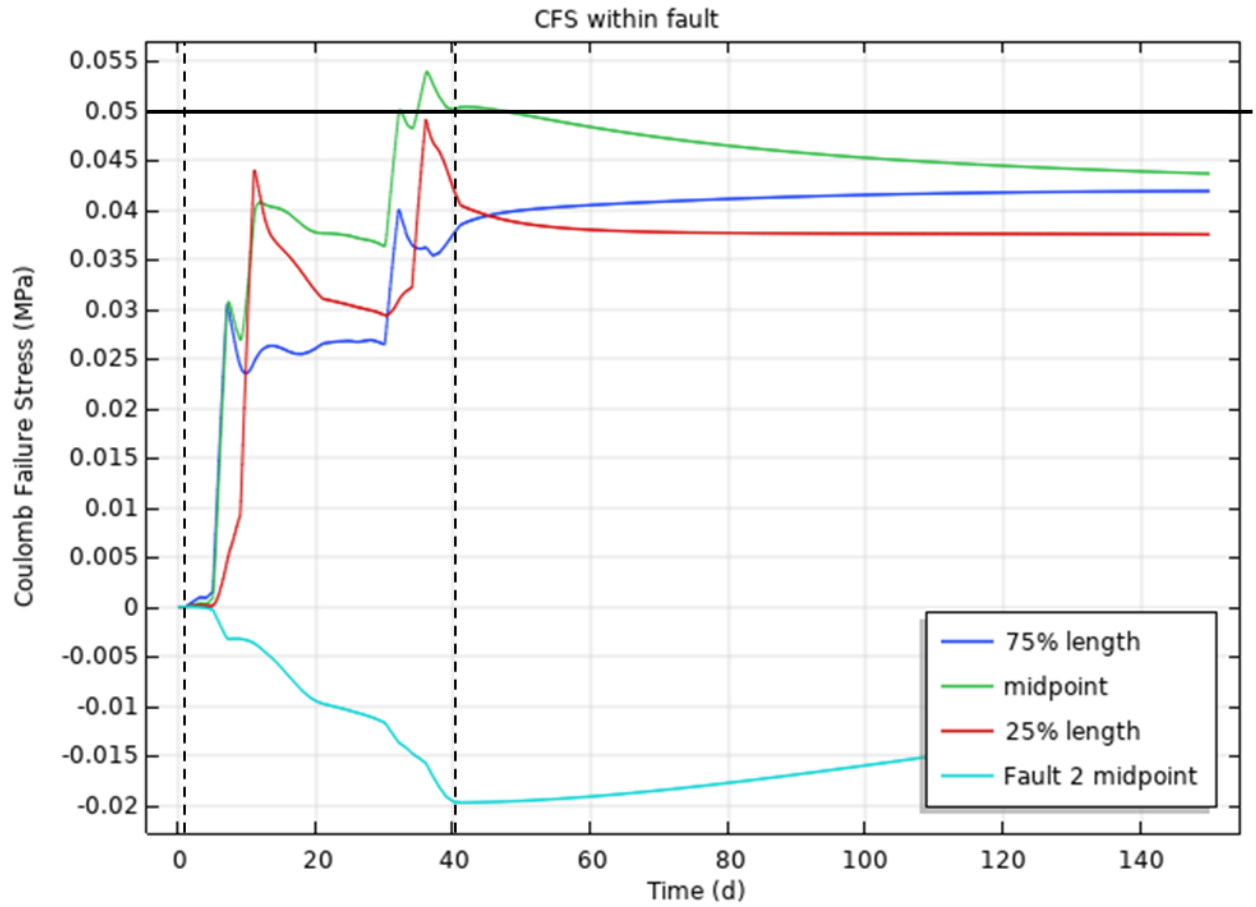
Figure 4.26: CFS within faults for Case Study 11. The stress threshold is met slightly earlier, but still within the injection into Wells A, B, and D.
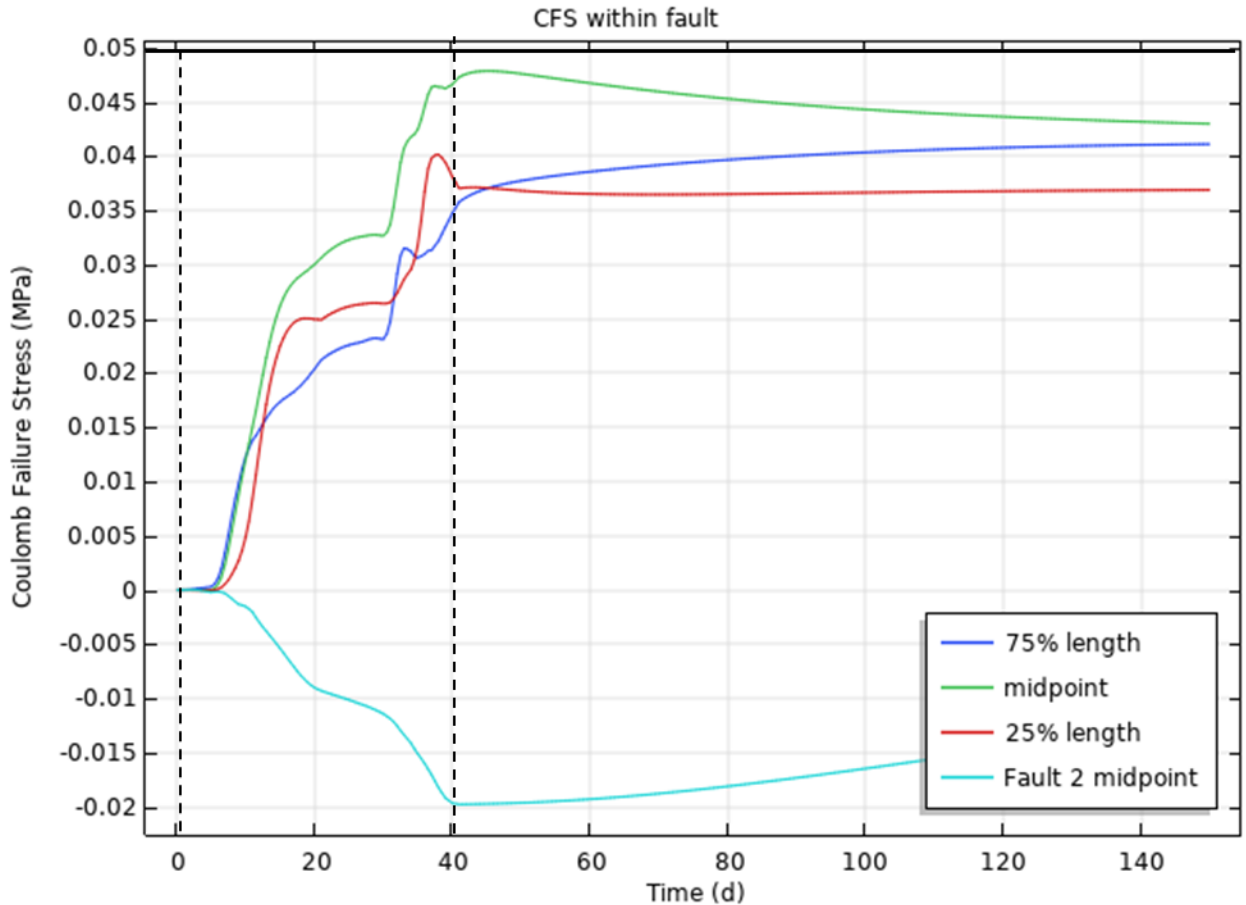
Figure 4.27: CFS within fault for Case Study 12. The increases in CFS are much smoother than in cases with higher permeability, but fail to meet the threshold of $0.05\ MPa$ in order to produce slip

4.10   Summary

Increases to pore pressure were the primary source of high CFS encouraging fault slip. In areas separated from the injection wells, solid stresses instead are more prevalent due to the inability for pore pressure to be transferred. Hydraulically isolated injection produced noticeable poroelastic stress, and it is dependant on the relative position and orientation of a fault whether those stresses encourage slip on said fault. In the arrangement common to many of these simulations, these stresses do not encourage slip and slip on the main fault is determined entirely by the amount of fluid capable of diffusing into the fault. Larger and more permeable fracture corridors allow slip to occur,

while more restrictive parameters result in the stress threshold for slip not being met. Slip on Fault 1 did produce an increase in CFS and activity in the vicinity of Fault 2, but this was not as far-reaching as those from the fracture corridors being pressurized. Altering the relative orientation of the two faults and the direction of slip on Fault 1 produced slight changes within this smaller area.

The results from these simulations, as well as the vertical cross-section simulations of Chapter 3, will be examined more in the upcoming Chapter 5: Discussion.

Chapter 5

5   Discussion

In Chapters 3 and 4, several simulations for the effects of hydraulic fracturing injection on a fault system have been described. These models can be examined for which mechanisms of stress transfer are responsible for producing expected seismicity. Additionally, since both models are based on field research performed near the Duvernay shale, the simulated results can be compared with the field data to examine if the simulations produce accurate results. Finally, which parameters of the model play an important role in determining the behaviour of the system are looked into.

5.1   Earthquake Triggering Mechanisms

Three potential methods for stress transfer to a fault were identified in the literature (see Chapter 1.3): increases in pore pressure within the faults, poroelastic stressing, and solid stresses resulting from slip on another fault. How these processes are represented in the simulated models is detailed below and summarized in Figure 5.1.

Pore Pressure Increases

- Correlated with CFS increases in all simulations
- Permeable channel required for slip in top-down model

Poroelastic Stresses

- More apparent on the Strike-Slip model
- Depends on orientation compared to the wells
- Decreases CFS with the simulated positions

Slip on a Nearby Fault

- Sharp change in CFS
- Stress increases beside the fault
- Most noticeable in unpressurized areas

Figure 5.1: Summary of stress transfer mechanisms within the simulated models

5.1.1   Pore Pressure Increases

Both simulated models had slip triggered by pore pressure increases. This is a commonly attributed cause of injection-induced seismicity (Kernanen and Weingarten, 2018, Castro et al., 2020). This is more clearly shown with the strike-slip model covered in Chapter 4, where the fault does not slip without the aid of a permeable connection to the fault as demonstrated in Case Studies 7, 8, 10, and 12. The model used in Chapter 3 placed the fault sufficiently close to the injection wells that fluid could diffuse into Fault 1 without the requirement of an additional connection.

5.1.2   Poroelastic Stressing

The forward and reverse faulting model examined in Chapter 3 model does not clearly show poroelastic effects on the faults, due to the faults being close enough to experience pressure increases. However, Case Study 3 on the strikes-slip fault model has a period of time where all active injection wells are not connected to the fault (see Figure

4.10). As such, during the early parts of the injection on most of the simulations, the Coulomb failure stress at the fault is instead determined mainly by the transfer of poroelastic stresses during this time period. Due to these stresses including a large amount of compressive normal stresses, the CFS change is negative at that time and fault slip is inhibited before the fault becomes pressurized (Figure 5.2). The inclusion of poroelastic stress into a model has been known to sometime decrease the activity in an area as well as increase it (Yeyha et al., 2018).
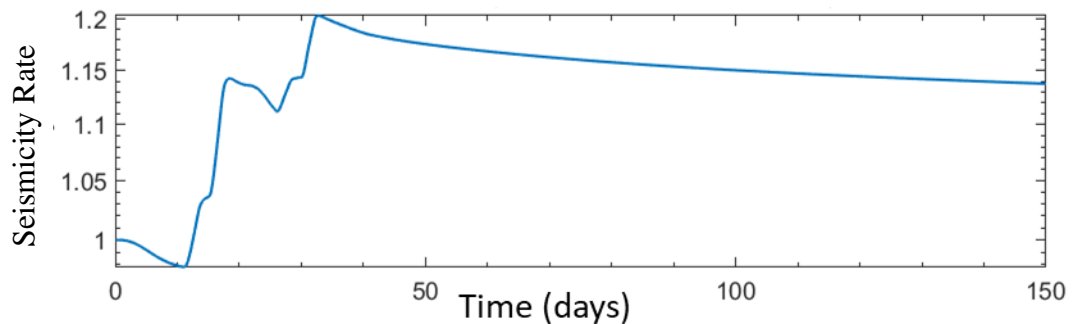
Figure 5.2: Activity rate over time for Case Study 3 of the strike-slip model, taken at the midpoint of Fault 1. No slip has been applied in order to better show the pressure-related and poroelastic changes.

It is however important to note that there are still areas where the poroelastic stresses encourage slip, specifically areas to the north or south of the active wells. As a result, faults positioned there would likely still encounter an increase in CFS. Since many faults activated via fluid injection are not previously known (Atkinson et al., 2020), it would be difficult to predict for a new injection site in the field whether any faults would be in an area of increased or decreased CFS as a result of poroelastic stressing.

5.1.3   Effects of Slip on Neighbouring Faults

The introduction of slip on one fault leads to a sharp change in the CFS in all cases for both models. Whether this change increases or decreases the expected activity depends on the position relative to the fault undergoing slip. Regions aligned with the fault have reduced CFS, and regions beside the fault experience an increase. For the simulated models, the second fault was always positioned beside the first one, placing it

in an area of increased stress. This change is larger close to the fault and is a larger component of the stress state at places and times that have not experienced increases in pressure, such as in the strike-slip model discussed in Chapter 4.

5.2   Comparing the Normal/Reverse Faulting Model

The observed activity from the field data examined by Bao and Eaton (2016) can be compared to the simulations for the similar systems examined in Chapter 3: Modelling Normal and Reverse Faults. It is worth noting that the system examined in the field is in a strike-slip faulting regime, while the limitations of a cross-sectional model require the simulated fault to experience normal and reverse faulting. The analysis performed by Bao and Eaton (2016) suggests both poroelastic stressing and pressure diffusion as causes for increased activity in the region. The simulated results show clear increases in activity related to changes in pore pressure, but they do not show significant increases related to poroelastic effects at the locations of the faults. As a result, the simulated results suggest pore pressure diffusion as the primary triggering mechanism for injection-related earthquakes. This discrepancy may be due to the limitations of a cross-sectional model. The injection points varied in the field data across the length of the horizontal wells, potentially leading to injection occurring farther from the faults at certain times, in turn potentially allowing for noticeable poroelastic effects that are not masked by high pore pressure at the fault.

5.2.1   Activity at Fault 1

The simulated Fault 1 undergoes slip very quickly after injection begins. This is in contrast to the field data, which shows significant activity within the system only occurring during the later stages of injection (Figure 5.3). One possible explanation is that a higher increase in stress was required to trigger an event on this fault. The largest recorded earthquake of the sequence occurred shortly after injection concludes. This is similar to the timing used in Case Study 2, which uses the peak stress within the fault which occurs $1\ day$ after injection finishes. Despite this, the Case Study 2 results indicate that the timing of slip on the main fault does not significantly affect the long-

term behaviour of the system, so the other simulations are still likely to have provided usable data.
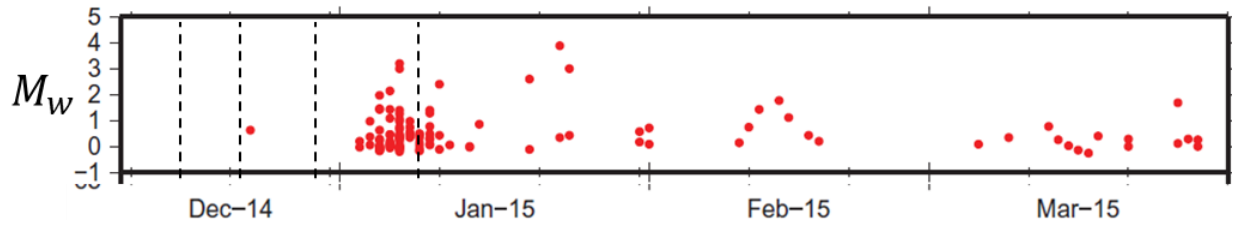
Figure 5.3: Recorded activity from Bao and Eaton (2016). Red dots represent seismic events. Injection periods are bounded by dashed lines.

5.2.2   Activity at Fault 2

Within the field data, the eastern fault strand experienced activity mostly during the injection period. Within the simulated data, the activity rate is increasing during this time, matching the field data (Figure 5.4). The simulated activity does peak later, near $t = 70\ days$, as a result of fluid diffusion reaching the fault, but this is not significantly higher than the value obtained during the injection period. Only small changes to the system would likely be required to have activity on Fault 2 cluster near the end of the injection period, matching the field results.
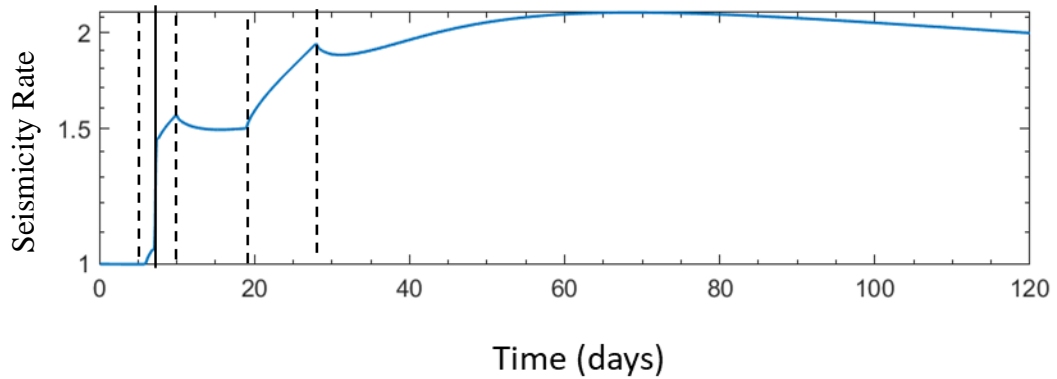
Figure 5.4: Activity within Fault 2 for Case Study 1. Injection periods are bounded by dashed lines and slip on Fault 1 is denoted by a solid line.

5.3   Comparing the Strike-Slip Model

The field data gathered by Igonin et al. (2021) was the basis for the model described in Chapter 4: Modelling Strike-Slip Faults. This data includes early injection wells that did not connect to the main fault under study in the simulation. Regardless, the behaviour of those wells that did connect to the main fault can still be compared to the simulation results. The field data shows a delay of approximately $1\ day$ between injection at a connected well and activity on the fault. Slip on the simulated fault is dependant primarily on the size and permeability of the regions connecting the injection wells and the fault, supporting the conclusions drawn by Igonin et al. (2021) suggesting that the fault was activated by pressure diffusion through a fracture network.

5.3.1   Slip Timing

Within the field data, the southern parts of the NS1 fault section are noted to have experienced seismic activity during the injection into well C. This was not the case for the simulated fault, where the threshold for slip was met during the later injection into wells A, B, and D for all simulations that produced slip. Since the CFS is pressure-driven, the earlier slip in the field data is likely due to another source of pressure increase not covered in the simulation model. The northern part of the NS1 structure appears to be the most likely candidate for this. This part of the system was not modelled as part of the fault during simulation in order to match the simulated fault length to the slip length for a $4.0M$ earthquake (Leonard, 2010). Another possibility is that the stress threshold for slip needed to be lowered in order for slip to occur during the earlier injection, but this is inconsistent with the results from the normal/reverse faulting model that seems to imply that a threshold of $0.05\ MPa$ may be too low.

While this section of NS1 did not experience seismic activity during the well C injection, it connects to both the northernmost fracture corridors and the part of NS1 that did experience earlier earthquakes. If it is a conductive fault structure, this would allow for an indirect connection between the southern part of NS1 and more northern injection wells. The additional fluid from these wells could then have led to a larger increase in pore pressure and CFS during the earlier injection.

5.4   Examining the Parameters

It is important to determine which aspects of a system are most influential on the overall stress state if forward-modelling approaches are to be used for risk assessment. A new project would involve uncertainty in many aspects that a single simulation cannot encompass. As such, by examining which parameters have a larger impact on the seismic activity, it informs what measurements are most important to perform to reduce the overall uncertainty in the stress state.

Of the examined parameters, the permeability of various features is the most important for determining the overall behaviour of the simulations. Since the Coulomb failure stress is dominated by the pore pressure in particularly active areas, the ability of that pressure to diffuse outwards significantly affects the stress state. Higher permeability leads to less intense activity over a wider area, while lower permeability results in smaller areas of more intense predicted seismicity, most clearly shown in Chapter 3 Case Study 5. The presence or absence of a permeable channel between injection sites and faults can determine whether or not the faults are likely to slip. This aspect is consistent with other numerical models in the literature, where permeable fracture corridors are considered to be a primary method of transferring stress to a fault (Castro et al., 2020, Igonin et al., 2020, Igonin et al., 2021, Wang et al., 2021).

Within the tested parameters, the angle of the fault being examined did not significantly alter the results of the simulations, seen in Chapter 3 Case Studies 6-8 and Chapter 4 Case Studies 5 and 6. Orientation does not affect the contribution of pore pressure to the CFS, and so the areas with the highest activity are only determined by the fault angle by way of having a differently oriented conductive fault connect different regions of the model. Differing angles become more significant when the stress is not being driven by pore pressure, though it would likely require a larger change in angle than was simulated in order to change the overall image.

For these models, the precise timing of the slip on the fault does not appear to produce a significant change to the long-term state. The slip does not significantly affect the pore pressure distribution, meaning that the pressure diffusion proceeds much the

same regardless of when the slip occurs. The end result is that after enough time has passed that the slip has occurred in both simulations, the stress state is not very different.

5.5 Future Investigations

One obvious avenue of future investigation would be to use additional computational resources in order to produce a fully three-dimensional model. This could allow for study of aspects such as a strike-slip fault extending into other rock layers with differing properties. As well, since most of the modelled systems included multiple faults, introducing multiple instances of slip in different locations will potentially yield useful information.

Many of the variant Case Studies were focused on different model geometry, with a smaller amount dedicated to differences in permeability. With the uncovered information that the permeability is the most prominent factor in determining the presence and timing of the simulated slip, it may be useful to examine the other material properties with more scrutiny. These changes could also include introducing anisotropic properties to the materials.

It would also be possible to use statistical analysis methods to determine if the simulated activity rates would be reasonably capable of producing the sequence of recorded events in addition to qualitatively comparing the events to peaks in the simulated rates.

5.6 Summary

The simulated models appear capable of predicting active locations similar to recorded field data. The highest contributions to the activity are provided by increases in pore pressure, and parameters such as material permeability that affect pore pressure diffusion are the most significant when determining the behaviour of the simulations. However, the timing of fault activation shows more differences from the pre-existing data. The fluid-related stressing occurs mostly independently of the slip, so this is not believed to significantly affect the overall behaviour of the system. In the case of the normal and reverse faulting model, these differences seem to indicate that a higher stress

threshold is required to produce larger earthquakes. For the strike-slip model, the differences can potentially be explained with the introduction of a longer fault that was only partly activated.

Chapter 6

6   Conclusions

The injection of fluid into rock masses is becoming increasingly common in industrial processes, and so modelling of the systems involved should be used to increase understanding of the underlying effects and to inform risk assessment of new projects. In particular, hydraulic fracturing operations use relatively low injection volumes and high injection pressures compared to other activities, and as a result require specific models. Fluid injection can lead to observed seismic activity as a result of increased pore pressure and changes to the solid stresses within the rock matrix as a result of poroelastic stressing or slip on another fault. Finite-element analysis is a useful tool for examining these effects.

This work uses a simulation that is fully coupled between the solid mechanics of the rock matrix and the flow of pressure within the rock pores. The normal stresses, shear stresses, and pore pressure through a model can be determined through their respective constitutive equations, then combined into the Coulomb Failure Stress in order to estimate the likelihood of slip occurring in an area. The Coulomb Failure Stress can then be used to determine the predicted rate of seismic activity.

Simulations were performed based on field data gathered from the Duvernay region using the commercially available software COMSOL Multiphysics. Both vertical and horizontal cross-sectional models have been examined. Parameters were then altered in order to determine their impact on the simulated system, including those associated with the model geometry, material properties, and application of slip on a fault.

Altering the permeability of model components led to significant changes in the simulation results, while parameters such as the slip timing had little change to the long-term behaviour of the system. The high dependence on permeability also extends to the activity on a second fault farther away from the injection. For the vertical models detailed in Chapter 3, the intermediate rock layers were somewhat permeable, allowing fluid to reach the secondary fault after some time. This was not the case for the top-down models

of the shale in Chapter 4, where the secondary fault received little increase in pore pressure. Those models also showed that the presence of permeable fractured areas between an injection site and pre-existing faults were required for the faults to undergo slip.

Much of the predicted activity was produced by increases in pore pressure, which is consistent with the literature. Poroelastic effects are noticeable in unpressurized areas but lead to lesser increases in CFS when compared to the contributions of pressure in areas hydraulically connected to the injection sites. Fault movement applies a noticeable change in the stress state near the fault and whether this change increases or decreases the CFS is dependant on the relative position from the fault.

Examining sites for fracture networks and determining the permeability of surrounding features would be important parts of determining the risk of seismic activity at a hydraulic fracturing operation. The model systems can be expanded into a more comprehensive three-dimensional model.

Appendix: List of Variables

Variables are listed in order of appearance

Variable	Description	Units	Variable	Description	Units
$\overleftrightarrow{\sigma}$	Stress tensor	MPa	E_u	Undrained Young's Modulus	MPa
σ_{ij}	Stress tensor components	MPa	ν_u	Undrained Poisson's Ration	—
$\overleftrightarrow{R}$	Rotation matrix	—	F_i	Applied force components	N
σ_i	Principal stresses	MPa	$\vec{q}$	Fluid flow rate	$m^3 s^{-1}$
θ_f	Fault angle	°	ρ_f	Fluid density	$kg m^{-3}$
σ	Normal stress	MPa	κ	Permeability	m^2
τ	Shear stress	MPa	η	Viscosity	$m^2 s^{-1}$
τ^L	Left-lateral shear stress	MPa	S_σ	Unconstrained specific storage	MPa^{-1}
τ^R	Right-lateral shear stress	MPa	m	Mass	kg
ϵ_{ij}	Strain tensor components	—	Q_{ext}	Fluid volume change	m^3
u_i	Displacements	m	S_c	Constrained specific storage	MPa^{-1}
x_i	Positions	m	S_u	Uniaxial specific storage	MPa^{-1}
ϵ_i	Principal strains	—	μ	Coefficient of friction	—
E	Young's Modulus	MPa	S	Coulomb failure stress	MPa
ν	Poisson's Ratio	—	R	Relative seismic activity rate	—
σ_{00}	Volumetric stress	MPa	r	Seismic activity rate	events/time
ϵ_{00}	Volumetric strain	—	r_0	Background activity rate	events/time
K	Bulk Modulus	MPa	τ_0	Background shear stress	MPa

β	Bulk Compressibility	MPa^{-1}	γ	Activity rate state variable	$MPa^{-1}s$
G	Shear Modulus	MPa	$\bar{\sigma}$	Effective normal stress	MPa
λ	Lamé Constant	MPa	t	Time	days
ϕ	Porosity	—	A	Direct-effect parameter	—
V	Volume	m^3	a	Constitutive parameter	—
V_P	Pore Volume	m^3	t_a	Characteristic time	days
α_B	Biot Coefficient	—	S	Background Coulomb stress	MPa
B	Skempton Coefficient	—	y	Simplified activity rate	$days^{-1}$
p	Pore pressure	MPa	A_σ	Simplified stress parameter	MPa
K_u	Undrained Bulk Modulus	MPa	t_R	Simplified time step	—

Bibliography

Altmann, J. B., Müller, B. I., Heidbach, O., Tingay, M. R., & Weißhardt, A. (2014). Pore pressure stress coupling in 3D and consequences for reservoir stress states and fault reactivation,. *Geothermics, 52*, 195-205. doi:10.1016/j.geothermics.2014.01.004

Andrés, S., Santillán, D., Mosquera, J. C., & Cueto-Felgueroso, L. (2019). Thermo-Poroelastic Analysis of Induced Seismicity at the Basel Enhanced Geothermal System. *Sustainability, 11*(24), 6904. doi:doi:10.3390/su11246904

Atkinson, G. M., Eaton, D. W., & Igonin, N. (2020). Developments in understanding seismicity triggered by hydraulic fracturing. *Nat Rev Earth Environ, 1*, 264-277. doi:10.1038/s43017-020-0049-7

Atkinson, G. M., Eaton, D. W., Gofrani, H., Walker, D., Cheadle, B., Schultz, R., . . . Kao, H. (2016). Hydraulic Fracturing and Seismicity in the Western Canada Sedimentary Basin. *Seismological Research Letters, 87*(3), 631-647. doi:10.1785/0220150263

Bao, X., & Eaton, D. W. (2016). Fault activiation by hydraulic fracturing in western Canada. *Science, 354*(6318), 1406-1409. doi:10.1126/science.aag2583]

Basich, S., Vörös, R., Rothert, E., Stang, H., Jung, R., & SchellSchmidt, R. (2010). A numerical model for fluid injection induced seismicity at Soultz-sous-Forets. *International Journal of Rock Mechanics and Mining Sciences, 47*, 405-413.

Bhattacharya, P., & Viesca, R. C. (2019). Fluid-induced aseismic fault slipoutpaces pore-fluid migration. *Science, 364*, 464-468.

Bickle, M. J. (2009). Geological carbon storage. *Nature Geoscience, 2*, 815-818.

Biot, M. A. (1941). General theory of three-dimensional consolidation. *J. Appl. Phys., 12*, 155-164.

Borst, R. d. (2018). *Computational Methods for Fracture in Porous Media.* Oxford: Elsiever.

Cappa, F., Scuderi, M. M., Collettini, C., Guglielmi, Y., & Avouac, J.-P. (2019). Stabilization of fault slip by fluid injection in the labratory and in situ. *Science Advances, 5*, eaau4065.

Chang, K. W., & Segall, P. (2016). Injection-induced seismicity on basement faults including poroelastic stressing. *J. Geophys. Res. Solid Earth, 121*(4), 2708-2726. doi:10.1002/2015JB012561

Chang, K. W., Yoon, H., & Martinez, M. J. (2018). Seismicity Rate Surge on Faults after Shut-in: PoroelasticResponse to Fluid Injection. *Bulletin of the Seismological Society of America, 108*(4), 1889-1904. doi:10.1785/0120180054

Cheng, A. H.-D. (2016). *Theory of Transport in Porous Media.* Oxford: Springer International Publishing.

Cocco, M., & Rice, J. R. (2002). Pore pressure and poroelasticity effects in Coulomb stress analysis of earthquake interactions. *Journal of Geophysical Research, 107*(B2), 2030. doi:10.1029/2000JB000138

Cornet, F. H. (2016). Seismic and aseismic motions generated by fluid injections. *Geomechanics for Energy and the Environment, 5*, 42–54.

Cundall, P. A. (2020). The Art of Numerical Modelling in Geomechanics. *Geo Congress 2020* (pp. 1-13). Minniapolis: ASCE.

Damjanac, B., & Cundall, P. (2016). Application of distinct element methods to simulation of hydraulic fracturing in naturally fractured reservoirs. *Computers and Geotechnics, 71*, 283-294.

Deng, K., Liu, Y., & Harrington, R. M. (2016). Poroelastic stress triggering of the December 2013 Crooked Lake, Alberta, induced seismicity sequence. *Geophysical Research Letters, 43*(16), 8482-8491. doi:10.1002/2016GL070421

Diechmann, N., Kraft, T., & Evans, K. (2014). Identification of faults activated during the stimulation of the Basel geothermal project from cluster analysis and focal mechanisms of the larger magnitude events. *Geothermics, 52*. doi:10.1016/j.geothermics.2014.04.001

Dieterich, J. (1994). A consitutive law for rate of earthquake production and its application to earthquake clustering. *Journal of geophysical research, 99*(B2), 2601-2618.

Dieterich, J., Cayol, V., & Okubo, P. (2000). The use of earthquake rate changes as a stress meter at Kilauea volcano. *Nature*, 457-460.

Eaton, D. W. (2018). *Passive Seismic Monitoring of Induced Seismicity.* Cambridge: Cambridge University Press.

Eaton, D. W., Igonin, N., Poulin, A., Weir, R., Zhang, H., Pellegrino, S., & Rodriguez, G. (2018). Induced Seismicity Characterization during Hydraulic-Fracture Monitoring with a Shallow-Wellbore Geophone Array and Broadband Sensors. *Seismological research letters, 89*(5), 1641-1651. doi:10.1785/0220180055

Ellsworth, W. L. (2013). Injection-Induced Earthquakes. *Science, 341*(6142), 142-142. doi:10.1126/science.1225942

Eyre, T. S., Eaton, D. W., Garagash, D. I., Zecevic, M., Venieri, M., Weir, R., & Lawton, D. C. (2019). The role of aseismic slip in hydraulic. *Science Advances*(5), eaav7172.

Gan, W., & Frohlich, C. (2013). Gas injection may have triggered earthquakes in the Cogdell oil field, Texas. *Proceedings of the National Academy of Sciences, 110*(47), 18786-18791. doi:10.1073/pnas.1311316110

Ge, J., Sukhvarsh, J., & Ahmad, G. (2020). Semianalytical modelling on 3D stress redistribution during hydraulic fracturing stimulation and its effects on natural fracture reactivation. *Int J Numer Anal Methods Geomech, 44*(8), 1184-1199. doi:https://doi.org/10.1002/nag.3056

Grigoli, F., Cesca, S., Priolo, E., Rinaldi, A. P., Clinton, J. F., Stabile, T. A., . . . Dahm, T. (2017). Current challenges in monitoring, discrimination, and management of induced seismicity related to underground industrial activities: A European perspective. *Reveiws of Geophysics, 55*(2), 310-340. doi:10.1002/2016RG000542

Hsu, Y.-J., Kao, H., Bürgmann, R., Lee, Y.-T., Huang, H.-H., Hsu, Y.-F., . . . Zhuang, J. (2021). Synchronized and asynchronous modulation of seismicity by hydrological loading: A case study in Taiwan. *Science Advances, 7*, eabf7282.

Igonin, N., Verdon, J. P., Kendall, J.-M., & Eaton, D. W. (2021). Large-Scale Fracture Systems Are Permeable Pathways for Fault Activation During Hydraulic Fracturing. *J Geophys Res Solid Earth, 126*(3), e2020JB020311. doi:doi.org/10.1029/2020JB020311

Im, K., Saffer, D., Marone, C., & Avouac, J.-P. (2020). Slip-rate-dependent friction as a universal mechanism for slow slip events. *Nature Geoscience, 13*, 705–710. doi:10.1038/s41561-020-0627-9

Jiang, G. (2021). Theoretical analysis of ground displacements induced by deep fluid injection based on fully-coupled poroelastic simulation. *Geodesy and Geodynamics, 12*(3), 197-210. doi:10.1016/j.geog.2021.02.005

Jiang, G., Liu, L., Barbour, A. J., Lu, R., & Yang, H. (2021). Physics-Based Evaluation of the Maximum Magnitude of Potential Earthquakes Induced by the Hutubi (China) Underground Gas Storage. *J Geophys Res Solid Earth, 126*(4), e2020JB021379. doi:10.1029/2020JB021379

Kernanen, K. M., & Weingarten, M. (2018). Induced Seismicity. *Annual Review of Earth and Planetary Sciences, 46*(1), 149-174. doi:10.1146/annurev-earth-082517-010054

King, G., & Devès, M. (2015). Fault Interaction, Earthquake Stress Changes, and the Evolution of Seismicity. In E. G. Schubert, *Treatise on Geophysics* (pp. 243-271). Oxford: Elsevier.

Leonard, M. (2010). Earthquake Fault Scaling: Self-Consistent Relating of Rupture
    Length, Width, Average Displacement, and Moment Release. *Bulletin of the
    Seismological Society of America, 100*(5A), 1971. doi:10.1785/0120090189

Lui, S. K., Huang, Y., & Young, R. P. (2021). The Role of Fluid Pressure-Induced
    Aseismic Slip in Earthquake Cycle Modulation. *Journal of Geophysical
    Research: Solid Earth, 126*, e2020JB021196. doi:10.1029/2020JB021196

Mazzoldi, A., Rinaldi, A. P., Borgia, A., & Rutqvist, J. (2012). Induced seismicity within
    geological carbon sequestration projects: Maximum earthquake magnitude and
    leakage potential from undetected faults. *International Journal of Greenhouse
    Gas Control , 10*, 434-442. doi:10.1016/j.ijggc.2012.07.012

McGarr, A. (2014). Maximum magnitude earthquakes induced by fluid injection. *J.
    Geophys. Res. Solid Earth, 119*(2), 1008-1019. doi:10.1002/2013JB010597

Meller, C., & Ledésert, B. (2017). Is There a Link Between Mineralogy, Petrophysics,
    and the Hydraulic and Seismic Behaviors of the Soultz-sous-Forêts Granite
    During Stimulation? A Review and Reinterpretation of Petro-Hydromechanical
    Data Toward a Better Understanding of Induced Seismicity. *J. Geophys. Res.
    Solid Earth, 122*(12), 9755-9774. doi:doi.org/10.1002/2017JB014648

Nicot, J.-P., Hosseini, S. A., & Solano, S. V. (2011). Are single-phase flow numerical
    models sufficient to estimate pressure distribution in CO2 sequestration projects?
    Energy Procedia, 4, Pages 3919-3926. doi:10.1016/j.egypro.2011.02.330

Norbeck, J. H., & Rubinstein, J. L. (2018). Hydromechanical Earthquake Nucleation
    Model Forecasts Onset, Peak, and Falling Rates of Induced Seismicity in
    Oklahoma and Kansas. *Geophysical Research Letters, 45*, 2963– 2975.
    doi:10.1002/2017GL076562

Peña Castro, A. F., Roth, M. P., Verdecchia, A., Onwuemeka, J., Liu, Y., Harrington, R.
    M., . . . Kao, H. (2020). Stress Chatter via Fluid Flow and Fault Slip in a
    Hydraulic Fracturing-Induced Earthquake Sequence in the Montney Formation,

British Columbia. *Geophysical Research Letters, 47*(14), e2020GL087254. doi:10.1029/2020GL087254

R. Heimisson, P. S. (2018). Constitutive Law for Earthquake Production Based on Rate-and-State Friction: Dieterich 1994 Revisited. *Journal of Geophysical Research: Solid Earth, 123*, 4141-4156. doi:10.1029/2018JB015656

Reches, Z. (2020). Dynamic Frictional Slip Along Rock Faults. *Journal of Tribology, 142*, 124501.

Rutqvist, J., Rinaldi, A. P., Cappa, F., & Moridis, G. J. (2013). Modelling of fault reactivation and induced seismicity during hydraulic fracturing of shale-gas reservoirs. *Journal of Petroleum Science and Engineering, 107*, 31-34. doi:10.1016/j.petrol.2013.04.023

Schultz, R., Skoumal, R. J., Brudzinski, M. R., Eaton, D., Baptie, B., & William, E. (2020). Hydraulic Fracturing-Indiced Seismicity. *Review of Geophysics, 58*(3), e2019RG000695. doi:10.1029/2019RG000695

Segall, P., & Lu, S. (2015). Injection-induced seismicity: Poroelastic and earthquake nucleation effects. *J. Geophys. Res. Solid Earth, 120*(7), 5082-5103. doi:10.1002/2015JB012060

Sgambato, C., Faure Walker, J. P., Mildon, Z. K., & Roberts, G. P. (2020). Stress loading history of earthquake faults influenced by fault/shear zone geometry and Coulomb pre-stress. *Scientific Reports, 10*, 12724. doi:10.1038/s41598-020-69681-w

Shapiro, S. A. (2015). *Fluid-Induced Seismicity.* Cambridge: Cambridge University Press.

Sherwood, J. D. (1993). Biot poroelasticity of a chemically active shale. *Proc. R. Soc. Lond., 440*, 365-377.

Shirzaei, M., Manga, M., & Zhai, G. (2019). Hydraulic properties of injection formations constrained by surface deformation. *Earth and Planetary Science Letters, 515*, 125-134.

Shiu, W., Guglielmi, Y., Graupner, B., & Rutqvist, J. (2021). Modelling the water injection induced fault slip and its application to in-situ stress estimation. *International Journal of Rock Mechanics and Mining Sciences, 137*, 104537. doi:10.1016/j.ijrmms.2020.104537

Skempton, A. W. (1954). The pore water coefficient A and B. *Geotechniqe, 4*, 143-147.

Treffeisen, T., & Henk, A. (2020). Representation of faults in reservoir-scale geomechanical finite element models – A comparison of different modelling approaches. *Journal of Structural Geology, 131*, 103931. doi:10.1016/j.jsg.2019.103931

van den Ende, M. P., Chen, J., Niemeijer, A. R., & Ampuero, J.-P. (2020). Rheological Transitions Facilitate Fault-Spanning Ruptures on Seismically Active and Creeping Faults. *J. Geophys. Res. Solid Earth, 125*(8), e2019JB019328. doi:doi.org/10.1029/2019JB019328

Verberne, B. A., Ende, M. P., Chen, J., Niemeijer, A. R., & Spiers, C. J. (2020). The physics of fault friction: insights from experiments on simulated gouges at low shearing velocities. *Soild Earth, 11*(6), 2075–2095. doi:10.5194/se-11-2075-2020

Verdecchia, A., Cochran, E. S., & Harrington, R. M. (2021). Fluid-Earthquake and Earthquake-Earthquake Interactions in Southern Kansas, USA. *J Geophys Res Solid Earth, 126*(3), e2020JB020384. doi:10.1029/2020JB020384

Viesca, R. C., & Dublanchet, P. (2019). The slow slip of viscous faults. *Journal of Geophysical Research: Solid Earth, 124*, 4959-4983. doi:10.1029/2018JB016294

Wang, B., Verdecchia, A., Kao, H., Harrington, R. M., Liu, Y., & Yu, H. (2021). A Study on the Largest Hydraulic Fracturing Induced Earthquake in Canada: Numerical

Modelling and Triggering Mechanism. *Bulletin of the Seismological Society of America, 111*(3), 1392-1404.

Wang, H. F. (2000). *Theory of Linear Poroelasticity.* Princeton: Princeton University Press.

Woods, A. W. (2015). *Flow in Porous Rocks.* Cambridge: Cambridge University Press.

Yenier, E., & Atkinson, G. M. (2015). Regionally Adjustable Generic Ground-Motion Prediction Equation Based on Equivalent Point-Source Simulations: Application to Central and Eastern North America. *Bulletin of the Seismological Society of America, 105*(4), 1989–2009. doi:10.1785/0120140332

Yeyha, A., Zhuo, Y., & Rice, J. R. (2018). Effect of Fault Architecture and Permeability Evolution on Response to Fluid Injection. *J. Geophys. Res. Solid Earth, 123*(11), 9982-9996. doi:doi.org/10.1029/2018JB016550

Zhai, G., Shirzaei, M., Manga, M., & Chen, X. (2019). Pore-pressure diffusion, enhacned by poroelastic stresses, controls induced seismicity in Oklahoma. *Proceedings of the National Acadamey of Sciences, 116*(33), 16228-16233. doi:10.1073/pnas.1819225116

Zhao, X., & Young, R. P. (2011). Numerical modelling of seismicity induced by fluid. *Geophysics, 76*(6), WC167-WC180. doi:10.1190/GEO2011-0025.1

Zoback, M. D. (2007). *Reservoir Geomechanics.* Cambridge: Cambridge University Press.

Zoback, M. D. (2019). *Unconventional Reservoir Geomechanics.* Cambridge: Cambridge University Press.

Curriculum Vitae

Name: **Charles Hulls**

Post-secondary   University of Guelph

Education and   Guelph, Ontario, Canada

Degrees: 2015-2019 B.Sc.

The University of Western Ontario

London, Ontario, Canada

2019-2022 M.Sc.

Honours and   Province of Ontario Graduate Scholarship

Awards: 1993-1994, 1994-1995

Related Work   Teaching Assistant

Experience   The University of Western Ontario

2019-2021